

**MECHANISTIC ASPECTS OF STABILIZATION OF
FERROELECTRIC, RELAXOR AND ANTIFERROELECTRIC
PHASES IN LEAD-BASED PEROVSKITE SYSTEMS**

*Thesis Submitted to
University of Calicut
in partial fulfillment of the requirements
for the award of the degree of
Doctor of Philosophy in Chemistry
under the Faculty of Science*

by

ANIL A.

**Under the supervision of
Dr. V. Kumar, Senior Scientist**



Centre for Materials for Electronics Technology (C-MET)
Scientific Society
Ministry of Electronics and Information Technology
Govt. of India, Shornur Road, M. G. Kavu, Athani P.O.
Thrissur 680 581, Kerala, India
Email: cmett@cmet.gov.in URL: wwwcmet.gov.in

September 2018

Mechanistic Aspects of Stabilization of Ferroelectric, Relaxor and Antiferroelectric Phases in Lead-based Perovskite Systems

Ph D Thesis under the Faculty of Science

Submitted by

Anil A.

Kayyil Veedu

Pallipuzha

Pakkam P.O-671316

Kasargod, Kerala, India

e-mail: anilpakkam@gmail.com

Research Supervisor

Dr. V. Kumar

Senior Scientist

Centre for Materials for Electronics Technology (C-MET)

Thrissur-680581

Kerala, India

e-mail: vkumar@cmet.gov.in

September 2018

**UNIVERSITY OF CALICUT
CERTIFICATE ON PLAGIARISM CHECK**

1.	Name of the research scholar	ANIL. A		
2.	Title of thesis/dissertation	MECHANISTIC ASPECTS OF STABILIZATION OF FERROELECTRIC, RELAXOR AND ANTIFERROELECTRIC PHASES IN LEAD-BASED PEROVSKITE SYSTEMS		
3.	Name of the supervisor	Dr. V. KUMAR		
4.	Department/Institution	C-MET THRISSUR		
5.	Similar content (%) identified	Introduction/ Review of literature	Materials and Methods	Result/Discussion/ Summary/Conclusion
		1%	0%	0%
	Acceptable maximum limit (%)	25	25	10
6.	Software used	Vedkund		
7.	Date of verification	8/8/2018		

*Report on plagiarism check, specifying included/excluded items with % of similarity to be attached.

Checked by (with name, designation & Signature)

Dr. Vinod.V.M.
Assistant Librarian
University of Calicut

Name & Signature of the Researcher

ANIL A

Name & Signature of the Supervisor

Dr. V. Kumar
Scientist
Centre for Materials for Electronics
Technology (C-MET), DIT, Govt. of India
Mulangunnathukavu, Athani,
Thrissur- 680 581

The Doctoral Committee* has verified the report on plagiarism check with the contents of the thesis, as summarized above and appropriate measures have been taken to ensure originality of the Research accomplished herein.

Name & Signature of the HoD/HoI (Chairperson of the Doctoral Committee)

डॉ. एन. रघु
Dr. N. RAGHU
निदेशक/Director
सी-मेट (एम इ आइ टी वी, भारत सरकार)
C-MET (MeitY, Govt. of India)
अथानि पोस्ट/Athani P.O., एम.जी. कावु /M.G. Kavu
त्रिस्सूर - 680 581 / Thrissur - 680 581
केरल/Kerala





सेन्टर फॉर मेटिरियल्स फॉर इलेक्ट्रॉनिक्स टेक्नोलॉजी (सी-मेट)

(वैज्ञानिक संस्था, इलेक्ट्रॉनिक्स और सूचना प्रौद्योगिकी मंत्रालय, भारत सरकार)

षोरनूर रोड, मुलंगुन्नतुकावु पोस्ट, अत्तानि, त्रिश्शूर - 680 581, केरला, भारत

CENTRE FOR MATERIALS FOR ELECTRONICS TECHNOLOGY

(Scientific Society, Ministry of Electronics and Information Technology, Government of India)

Shoranur Road, P.O. Mulangunnathukavu, Athani, Thrissur - 680 581, Kerala, India

Tel : EPABX : 91-487-2201156-59 (4 LINES). Fax : 91-487-2201347

E-mail : cmett@cmet.gov.in URL : www.cmet.gov.in

Dr. V. Kumar

Scientist F

Certificate

This is to certify that the thesis entitled “*Mechanistic Aspects of Stabilization of Ferroelectric, Relaxor and Antiferroelectric Phases in Lead-based Perovskite Systems*” submitted to Calicut University in partial fulfillment of the requirements for the award of the degree of *Doctor of Philosophy in Chemistry* under the Faculty of Science, Calicut University, Malappuram is a record of the authentic work carried out by Mr. Anil A., at Centre for Materials for Electronics Technology (C-MET), Thrissur under my guidance. The work presented in the thesis has not been submitted for any other degree or diploma of this or any other University and has been found to have no plagiarism using the software approved by the UGC/University.

Thrissur
September 2018

Dr. V. Kumar
(Supervising Guide)

Declaration

I hereby declare that the thesis entitled “*Mechanistic Aspects of Stabilization of Ferroelectric, Relaxor and Antiferroelectric Phases in Lead-based Perovskite Systems*” submitted to Calicut University, is based on the original research work carried out by me under the guidance and supervision of Dr. V. Kumar, Senior Scientist, Centre for Materials for Electronics Technology (C-MET), Thrissur. No part of this work has been presented for the award of any other degree from any other institution.

Thrissur
September 2018

Anil A

Acknowledgments

At the very beginning, I would like to express my sincere gratitude to my supervising guide Dr. V. Kumar, for the continuous support, excellent guidance, patience and encouragement throughout the course of the research period. His deep insights helped me at various stages of this research programme.

I am thankful to Kerala State Council for Science, Technology and Environment (KSCSTE), Government of Kerala, for a research fellowship. I am also thankful to Dr. C. Arunan and Dr. B. Sarika, Basic Science Division, KSCSTE for their help and support in this regard.

I convey my extreme gratitude to the Doctoral Committee members, Prof. P. Raveendran (Head, Department of Chemistry) and Prof. Abraham Joseph (Dean, Faculty of Science) Calicut University for their valuable time and constant motivation.

The helping hands from various institutions are greatly acknowledged. I acknowledge the help rendered to me by Prof. K. B. R. Varma, IISc Bangalore and his students Mr. Jaschin and Dr. P. Bharathi for P-E analysis. I would also like to acknowledge Prof. Ajit Kulkarni, IIT Bombay, for P-E analysis. I am extremely thankful to UGC-DAE Consortium for Scientific Research (UGC-DAE CSR) Indore Center for providing their esteemed facilities. I acknowledge the help rendered to me by Dr. V. Raghavendra Reddy, UGC-DAE CSR Indore and his students Mr. Akash and Ms. Anjali for carrying out the P-E analysis of samples. I am thankful to Prof. G. Unnikrishnan NIT Calicut, for the XRD analysis carried out in his laboratory. I am also thankful to STIC, Kochi and SAIF, IIT Madras for the support given to me during the research work.

I am extremely thankful to Dr A. Seema and Dr. M. N. Muraleedharan for the low temperature measurements. I would like to acknowledge the co-operation and comments from Dr. S. N. Potty and Dr. K. V. Baiju.

I would like to thank my fellow lab mates Dr. K. Vani and Dr. A. S. Divya, for stimulating discussions and sharing their knowledge through sincere association. Thanks to Dr. T. Anto Johny for the co-operation and constant motivation. Sincere thanks to Ms. S. Laxmi Priya and Ms. K. V. Vijila for the co-operation in the laboratory. I take this opportunity to express my heartfelt gratitude to Mr. N. Manoj for his brother-like concern and creating a pleasant working atmosphere in laboratory. I would like to thank Mr. M.K. Satheesan for being-considerate and true motivation.

Thanks are also due to Mr. C. Rohith, Mr. V. Vinoj, Mr. P. Gopakumar, Ms. N. B. Rahna and Mr. M. Sathyanarayana for their sincere association. I also take this opportunity to mark my record of appreciation to Ms. V. Priyadarsini for strong support and sincere help. I would also like to thank Mr. K. Sivanandan and Mr. Abhisek Choudhary for their encouragement.

I would like to thank my C-MET friends, Dr. M. Libu, Dr. A. Surjith, Mr. S. Susanth, Mr. E. K. Suresh, Mr. P. Prabeesh, and Mr. P. P. Deepak for extending sincere support throughout the period.

I take this opportunity to express my heartfelt gratitude to Prof. K. R. Haridas, Dr S. Sudheesh and classmates of School of Chemical Sciences, Kannur University.

I owe my deepest gratitude to my life partner Bindu, for her understanding of my goals and aspirations. Her love and support have always been my strength. I am thankful to my son Aaron for giving me happiness during the past two years of my research period.

A special thanks to my brother Aneesh, sisters Anitha and Akhila, brothers-in-law, sister-in-law, father-in-law, mother-in-law and Vivek (brother-in-law) for their love and support.

Words are not enough to express the care and support extended by my big family to complete this thesis. I feel a deep sense of gratitude to my father Krishnan, mother Padmavathi, and elder sister of my father Lakshmi for their constant encouragement and inspiration.

Anil A.

Preface

In view of great technological importance, ABO₃-type perovskite ferroelectric ceramics and devices has been of considerable interest over the last few decades. This has been attributed to their exciting application possibilities in the field of transducers, actuators and sensors ranging from non-volatile memory applications to microelectromechanical systems (MEMS). In ABO₃-type ferroelectric ceramics, Lead-based perovskite systems are still the material of choice for piezoelectric based sensors and actuators due to their superior electromechanical properties which may be modified by appropriate doping. Depending on the differences observed in electromechanical characteristics, these material systems are categorized as ferroelectrics (FEs), relaxor ferroelectrics (RFEs) and antiferroelectrics (AFE). Mechanistic aspects of stabilization of different phases in Lead-based perovskite systems present a considerable challenge.

The thesis is organized in to five chapters. Chapter 1 deals with the general introduction to three different categories namely ferroelectrics, relaxor ferroelectrics and antiferroelectrics. This chapter is further divided into three parts to discuss the above mentioned three systems in detail. The first part includes the basic concepts like ferroelectric polarisation and domains in ferroelctrics. This part also includes the charge compensation mechanisms that occur during aliovalent doping and discuss different theories explaining the aging mechanism in *hard* ferroelectrics. The second part discusses in detail the local structural rearrangements and lattice dynamics in Lead-based relaxors. Finally the mechanistic aspects of AFE-FE phase transformations in antiferroelectrics are discussed in detail in the third part.

The experimental methods adopted for synthesis of lead-based compositions are given in chapter 2. Different characterization techniques employed are highlighted. This chapter discusses the theory of some of the important characterization techniques like X-ray powder diffraction (XRD), Raman spectroscopy and Electron Paramagnetic Resonance (EPR) spectroscopy. Interactions affecting the local symmetry of transition metal ion sites are discussed in detail. Also this chapter briefly explains the principles behind the dielectric, ferroelectric and piezoelectric characterization using Impedance/Gain phase analyzer and Piezoevaluation system.

For better performance and reliability of ferroelectric devices, degradation of ferroelectric properties with time, referred to as aging have to be minimized. For imparting excellent electromechanical characteristics, hybrid-doping (i.e., donor and acceptor co-doping) is a very useful strategy. However, aging in such systems have not yet been well understood. Chapter 3 is dedicated to the discussions regarding the aging in hybrid-doped lead zirconate titanate (PZT). We have shown in Chapter 3, that ferroelectric aging in hybrid-doped PZT is related to the acceptor:donor ratio. At higher donor-level compositions significant resistance to aging is observed. This is in contrast to the aging observed in non-lead containing compositions like barium titanate, irrespective of the donor:acceptor ratio. Through EPR study, the defect chemistry responsible for aging-resistance at high levels of donor dopant concentrations have been comprehensively established. Results demonstrate that at appropriate donor:acceptor ratio, piezoceramics with enhanced dielectric and piezoelectric characteristics can be realised thus their device application potential.

Relaxor ferroelectrics of lead-based complex perovskites of the type $\text{Pb}(\text{B}_{1-x}'\text{B}_x'')\text{O}_3$ have attracted interest for transducer applications in view of

their excellent piezoelectric properties, especially their co-fireability with cheaper metal electrodes. However, origin of the relaxor behavior in Lead-based complex perovskites is still under debate and is actively studied by many groups. Local structural rearrangements in lead-based complex perovskites of the type $(\text{Ba}_{1-x}\text{Pb}_x)(\text{In}_{0.50}\text{Nb}_{0.50})\text{O}_3$, responsible for transition from ferroelectric (FE) to relaxor (R) phase have been systematically examined by us using detailed Raman spectroscopic studies which are reported in Chapter 4. Raman spectral investigation clearly reveal that relaxor behavior in the lead based complex perovskites to be a consequence of stereochemical influence of the ns^2 lone-pair electrons in Pb^{2+} which results in an off-center displacement of lead atoms along $\langle 111 \rangle$. In complex perovskite of the type $\text{Pb}(\text{B}_{1-x}'\text{B}_x'')\text{O}_3$ the relative size of two different B-site cations have a prominent effect on the Pb^{2+} -displacement along $\langle 111 \rangle$. Subtle changes in the Pb-O and B-O bonding brought about by this off-centre displacement results in decoupling of dynamic Pb-O-B bond, leading to relaxor state. The study presented in Chapter 4 provides clear insights into the mechanistic aspects of the FE \rightarrow R transitions.

The ternary PbZrO_3 - PbTiO_3 - PbSnO_3 system holds strong scientific interest due to the presence of both ferroelectric and antiferroelectric phases. They are attractive in actuator applications as they exhibit large mechanical strains during field induced antiferroelectric(AFE)-ferroelectric(FE) transformation. However, many material systems in the PbZrO_3 - PbTiO_3 - PbSnO_3 ternary systems have also evinced considerable theoretical interest, especially with respect to the nature and sequence of the phase transformations below Curie point. Influence of defect structures on the FE \rightarrow AFE phase transformation and existence of incommensuration in tin-modified lead zirconate titanate have been studied and reported in Chapter 5. Results

obtained from temperature dependent dielectric, polarisation-electric field, strain-electric field and EPR spectral investigations have revealed that in tin-modified lead zirconate titanate $\text{Pb}(\text{Zr}_{0.60}\text{Sn}_{0.30}\text{Ti}_{0.10})\text{O}_3$, B-site acceptor dopant, Mn^{3+} favour the stabilization of FE phase and suppress the formation of incommensuration. This study validates mechanistic aspects of incommensurate structure in antiferroelectric phase and provides clear insights on the defect-mediated stabilization of FE phase in the same.

The last section contains the highlights of the present work. The major findings of the present work have led to three publications in international journals and two patents.

CONTENTS

Motivations for the Present Study

Chapter 1 Introduction	1
1.1 Introduction to Ferroelectrics.....	3
1.1.1 Perovskite structure	3
1.1.2 Chemical bonding in perovskites	5
1.1.3 Ferroelectric polarisation	7
1.1.4 Ferroelectric domains.....	10
1.1.5 Poling of ferroelectrics	11
1.1.6 Ferroelectric properties.....	12
1.1.6.1 Polarisation-Electric field hysteresis curve.....	12
1.1.6.2 Strain-Electric field curve	13
1.1.7 Lead Zirconate Titanate (PZT) solid solution	15
1.1.7.1 ‘Soft’ and ‘Hard’ PZT- Effects of defects--	16
1.1.8 Domain stabilization in ‘Hard’ ferroelectrics and its consequences	18
1.1.8.1 Domain stabilization theories	21
1.1.8.1.1 Grain boundary effect	21
1.1.8.1.2 Domain wall effect	22
1.1.8.1.3 Volume effect	22
1.1.9 Symmetry Conforming - Short Range Ordering of point defects	23
1.1.9.1 SC-SRO mechanism in rhombohedral and orthorhombic ferroelectrics.....	26
1.1.10 Factors influencing SC-SRO mechanism ---	29
1.1.10.1 Locking of defect dipoles in the lattice---	29
1.1.10.2 Kinetics of migration of oxygen vacancy in perovskite structure	30

1.1.11	Recoverable nonlinear electrostrain by reversible domain switching -----	32
1.2	Introduction to Relaxor ferroelectrics -----	34
1.2.1	Lattice dynamics of relaxor ferroelectrics ---	36
1.2.2	Origin of PNR and evolution of relaxor state -----	38
1.2.3	Relaxors with perovskite structure -----	41
1.2.3.1	A-site substituted complex perovskite (Pb, A'')BO ₃ -----	41
1.2.3.2	B-site substituted complex perovskite, Pb(B',B'')O ₃ -----	41
1.2.3.3	B-site ordering in Pb(B',B'')O ₃ type complex perovskites -----	43
1.2.4	Local structural preferences and special bonding considerations in Lead-based complex perovskites -----	44
1.3	Introduction to Antiferroelectrics -----	46
1.3.1	Lead Zirconate-----	47
1.3.2	Importance of AFE materials-----	48
1.3.2.1	Crystal structure change during AFE-FE phase transformation -----	48
1.3.2.2	Polarisation and Strain behaviour during AFE-FE phase transformation -	49
1.3.2.3	Phase switching induced currents -----	51
1.3.3	AFE-FE phase switching sequence-----	51
1.3.4	Stability of phases in AFEs -----	53
1.3.5	Stability of ferroelectric phase in antiferroelectric Lead zirconate -----	54
1.3.6	Ferroelectric and antiferroelectric Sn-modified Lead Zirconate Titanate-----	58
1.3.7	Incommensuration in Sn-modified Lead Zirconate Titanate-----	62

1.3.7.1	Compositional effects (Sn/Ti ratio) on incommensuration-----	64
1.3.7.2	Effect of DC bias on incommensuration-----	65
1.3.8	Incommensuration in La-modified antiferroelectric Lead Zirconate Titanate ----	67
References	-----	69

Chapter 2 Experimental Methods and Characterization Techniques ----- 85

2.1	Ceramic processing -----	87
2.1.1	Solid state route -----	87
2.1.2	Sol-Gel method -----	89
2.2	Characterization techniques -----	91
2.2.1	X-ray powder diffraction-----	91
2.2.2	Raman spectroscopy -----	92
2.2.3	Electron Paramagnetic Resonance spectroscopy -----	95
2.2.3.1	Origin of EPR signal-----	95
2.2.3.2	Factors affecting the magnitude of the 'g' factor -----	97
2.2.3.3	Orientation dependence of 'g' factor---	98
2.2.3.4	Hyperfine Interaction-----	98
2.2.3.5	Interactions affecting the energies of unpaired electrons in transition metal ion complexes -----	100
2.2.3.6	Theoretical description- spin-Hamiltonian concept-----	102
2.2.3.7	Simulation techniques -----	103
2.2.4	Dielectric and ferroelectric characterization techniques -----	104
2.2.4.1	Dielectric characterization -----	104
2.2.4.2	Piezoelectric characterization -----	106
2.2.4.3	P-E and S-E loop measurements -----	107

References -----	109
Chapter 3 Ferroelectric Aging in Hybrid-Doped PZT---	113
3.1 Introduction -----	115
3.2 Experimental Procedure-----	117
3.3 Results and Discussion -----	118
3.3.1 Ferroelectric Aging -----	119
3.3.2 Ferroelectric properties-----	126
3.4 Conclusion -----	127
References -----	128
Chapter 4 Local Structural Rearrangements and Evolution of Relaxor states in Complex Perovskite Systems -----	131
4.1 Introduction -----	133
4.2 Experimental Procedure-----	138
4.3 Results and Discussion -----	139
4.3.1 Origin of Raman bands-----	142
4.4 Conclusion -----	154
References -----	155
Chapter 5 Defect-mediated Stabilization of Ferroelectric Phase in Antiferroelectric PZST-----	161
5.1 Introduction -----	163
5.2 Experimental Procedure-----	166
5.3 Results and Discussion -----	167
5.4 Conclusion -----	176
References -----	177
Highlights of the Present work -----	181
List of Publications -----	183

LIST OF TABLES

Table 1.1	EXAFS results of bond distance in several $\text{Pb}(\text{B}', \text{Nb})\text{O}_3$ ---	45
Table 3.1	Spin-Hamiltonian parameters -----	121
Table 4.1	EXAFS results of bond distance in several $\text{Pb}(\text{B}', \text{Nb})\text{O}_3$ ----	136
Table 4.2	Wyckoff positions and corresponding phonon modes in $\text{Fm}\bar{3}\text{m}$ -----	141
Table 4.3	Wyckoff positions and corresponding phonon modes in $\text{Pm}\bar{3}\text{m}$ -----	141
Table 4.4	Mode assignment for the symmetry allowed Raman active modes in $\text{Fm}\bar{3}\text{m}$ -----	143
Table 5.1	Spin-Hamiltonian parameters -----	175

LIST OF FIGURES

Figure 1.1	Ideal ABO ₃ Perovskite Structure-----	3
Figure 1.2	Spontaneous polarisation directions (indicated by arrows) in a typical ABO ₃ unit cell BaTiO ₃ (a) cubic (reference) (b) tetragonal (c) orthorhombic and (d) rhombohedral -----	5
Figure 1.3	Representative σ and π bonding in a Perovskite Structure -----	6
Figure 1.4	Molecular orbital diagram of BO ₆ octahedron in ABO ₃ perovskite -----	7
Figure 1.5	Illustration of the changes in a ferroelectric material which transforms from cubic paraelectric phase into tetragonal ferroelectric phase with temperature-----	8
Figure 1.6	Curie- Weiss plot for typical ferroelectric BaTiO ₃ -----	9
Figure 1.7	Schematic representations of 180 ⁰ and 90 ⁰ domains and domain walls -----	10
Figure 1.8	Formation of 90 ⁰ and 180 ⁰ ferroelectric domain walls -----	11
Figure 1.9	Polycrystalline ferroelectric with random orientation of grains before and after poling -----	12
Figure 1.10	Ferroelectric Polarisation-Electric field hysteresis loop-----	13
Figure 1.11	Ferroelectric Strain-Electric field hysteresis loop -----	14
Figure 1.12	Electric field dependence of polarisation and strain in electrostrictive material -----	14
Figure 1.13	Phase diagram of PZT solid solution -----	15
Figure 1.14	P-E hysteresis characteristics of unaged Fe ³⁺ -doped PZT at room temperature for (a) unpoled (b) poled. Internal bias (E _i) at various Fe ³⁺ concentrations given in (c) -----	19
Figure 1.15	P-E hysteresis loops before and after aging (a) unpoled (b) poled -----	20
Figure 1.16	Schematic representation of grain boundary effect-----	21
Figure 1.17	Schematic representation of domain wall effect -----	22
Figure 1.18	Schematic representation of volume effect -----	23
Figure 1.19	Tetragonal crystal symmetry and the related defect symmetry in unaged and aged state. Circle with maximum unshaded are represents the most probable site of oxygen vacancy -----	25

Figure 1.20	Rhombohedral crystal symmetry and the related defect symmetry in unaged and aged state. Circle with maximum unshaded area represents the most probable site of oxygen vacancy -----	27
Figure 1.21	Orthorhombic crystal symmetry and the related defect symmetry in structure unaged and aged state. Circle with maximum unshaded area represents the most probable site of oxygen vacancy -----	28
Figure 1.22	Dependence of internal bias, E_i on doping concentration of PZT ceramics in the unpoled aged state -----	29
Figure 1.23	P-E and S-E curves of aged samples of (a) Fe^{3+} and (b) Mn^{3+} doped $[(Ba_{0.80}Sr_{0.20})TiO_3]$ -----	30
Figure 1.24	P-E hysteresis loops at room temperature for Ga^{3+} , Al^{3+} , Mg^{2+} -doped Barium titanate samples in the unaged and aged states -----	31
Figure 1.25	(a) Electrostrain in aged sample of Mn^{3+} -doped BT; (b) Point defect mediated reversible domain switching mechanism in tetragonal ferroelectric unit cell generates large electrostrain -----	32
Figure 1.26	(a) Field Dependence of electrostrain of Mn^{3+} -doped BST; (b) Cycle dependence of electrostrain of Mn^{3+} -doped BST -----	33
Figure 1.27	Temperature dependence of dielectric permittivity and Curie-Weiss ($1/\epsilon_r$ vs T) plot at $T > T_c (T_m)$ -----	34
Figure 1.28	Temperature dependence of saturation and remnant polarizations -----	35
Figure 1.29	P-E hysteresis characteristics normal relaxor ferroelectrics-----	35
Figure 1.30	Dark field image of ordered domains in nanoscale in PMN -----	36
Figure 1.31	Schematic representation of temperature evolution of polar nano regions and macroscopic ferroelectric domains in relaxors -----	37
Figure 1.32	Vögel-Fulcher fitting curve of typical relaxor ($Pb_{0.92}La_{0.08}$) ($Zr_{0.65}Ti_{0.35}Cu_{0.004}O_3$). Circles represent experimental data and solid line represents fitting curve -----	40
Figure 1.33	Temperature dependence of dielectric constant of (a) disordered (b) partially ordered and (c) ordered PIN -----	42
Figure 1.34	Temperature dependence of dielectric constant of disordered and ordered PST -----	42

Figure 1.35 Schematic representation of (a) ordered; (b) disordered Pb(B',B'')O ₃ perovskite. Black, green and red circles represent Pb, B' and B'' cations respectively. Dashed arrows show the region having disordered arrangement-----	43
Figure 1.36 B-site ordering in (a) A(B' _{1/2} B'' _{1/2})O ₃ and (b) A(B' _{1/3} B'' _{2/3})O ₃ -----	44
Figure 1.37 Atomic arrangements in R $\bar{3}$ m symmetry for Pb(B',B'')O ₃ structure -----	45
Figure 1.38 Ternary phase diagram for PbZrO ₃ -PbTiO ₃ -PbSnO ₃ system -----	46
Figure 1.39 Polarisation-Electric field characteristics for antiferroelectric phase-----	47
Figure 1.40 Antiferroelectric structure of Lead zirconate. Arrows represent the direction of shifts of Pb ²⁺ ions; solid line shows an orthorhombic unit cell; dashed lines show the unit cells of the high temperature cubic phase -----	47
Figure 1.41 Schematic diagram of the primitive cell in AFE and FE states -----	49
Figure 1.42 Polarisation-Electric field characteristics for field forced antiferroelectric to ferroelectric phase transition -----	50
Figure 1.43 Polarisation-Electric field characteristics for field forced antiferroelectric to ferroelectric phase transition -----	50
Figure 1.44 Current- Electric field curves of AFEs during AFE-FE phase transformation-----	51
Figure 1.45 Schematic diagram of AFE-FE phase switching procedure-----	52
Figure 1.46 Sequence of phase transitions as a function of temperature for (a) AFE _O and (b) AFE _T phases -----	53
Figure 1.47 Dielectric constant versus temperature curve for PbZrO ₃ -----	54
Figure 1.48 Phase diagram of (a) (Pb _{1-x} Ba _x)ZrO ₃ (b) (Pb _{1-x} Sr _x)ZrO ₃ -----	56
Figure 1.49 Phase diagram of PbZrO ₃ with admixtures of Nb ⁵⁺ -----	57
Figure 1.50 PbZrO ₃ - PbTiO ₃ phase diagram -----	57
Figure 1.51 Ternary phase diagram for PbZrO ₃ -PbTiO ₃ -PbSnO ₃ system -----	58
Figure 1.52 Temperature-composition phase diagram for Pb _{0.98} Nb _{0.02} [(Zr _{0.90} Sn _{0.10}) _{1-y} Ti _y] _{0.98} O ₃ with y variable, (a) for increasing temperature and (b) for decreasing temperature -----	59
Figure 1.53 Temperature-composition phase diagram for Pb _{0.98} Nb _{0.02} [(Zr _{1-x} Sn _x) _{1-y} Ti _y] _{0.98} O ₃ with 'x' variable, y = (a)0.03 and (b)0.06 -----	60

Figure 1.54	Temperature dependent dielectric response in compositional series of formula $\text{Pb}_{0.995}\text{Nb}_{0.01}[(\text{Zr}_{0.60}\text{Sn}_{0.40})_{1-x}\text{Ti}_x]_{0.99}\text{O}_3$	61
Figure 1.55	Free energies of Cubic Paraelectric (PE_c), Multi Cell Cubic (MCC) and Ferroelectric (FE)/ Antiferroelectric (AFE) phases	62
Figure 1.56	[001] SAED patterns for $\text{Pb}_{0.98}\text{Nb}_{0.02}[(\text{Zr}_{0.58}\text{Sn}_{0.42})_{0.96}\text{Ti}_{0.04}]_{0.98}\text{O}_3$, at temperature a) 25°C, b) 75°C, c) 100°C, d) 140°C, e) 155°C and (f) 165°C	63
Figure 1.57	(a) Modulation wavelength (λ) of incommensurate structure and (b) dielectric response as a function of temperature	64
Figure 1.58	Dielectric response of $\text{Pb}_{0.98}\text{Nb}_{0.02}[(\text{Zr}_{1-x}\text{Sn}_x)_{0.94}\text{Ti}_{0.06}]_{0.98}\text{O}_3$ as a function of temperature where $x =$ a) 0.40, b) 0.45 and c) 0.50	64
Figure 1.59	Dielectric response of $\text{Pb}_{0.98}\text{Nb}_{0.02}[(\text{Zr}_{0.55}\text{Sn}_{0.45})_{1-y}\text{Ti}_y]_{0.98}\text{O}_3$ as a function of temperature where $y =$ a) 0, b) 0.03, c) 0.06 and d) 0.09	65
Figure 1.60	Dielectric response of $\text{Pb}_{0.98}\text{Nb}_{0.02}[(\text{Zr}_{0.57}\text{Sn}_{0.43})_{0.90}\text{Ti}_{0.10}]_{0.98}\text{O}_3$ as a function of temperature at dc bias levels a) 0, b) 2.5, c) 5, d) 10 and e) 15kV/cm	66
Figure 1.61	PLZT phase diagram	67
Figure 2.1	Flow chart for solid state reaction method	88
Figure 2.2	Flow chart for Sol-Gel method	90
Figure 2.3	Schematic of Bragg Diffraction	91
Figure 2.4	X-ray Diffractometer	92
Figure 2.5	Energy level diagrams for Raman and Rayleigh scattering	94
Figure 2.6	DXR Raman microscope (Thermo Scientific USA)	95
Figure 2.7	Induction of the spin state energies as a function of the magnetic field B_0	97
Figure 2.8	Energy states for an electron in a magnetic field effect of a nuclear spin of $\frac{1}{2}$	100
Figure 2.9	EPR spectrum of single electron interacting with a magnetic nucleus with nuclear spin, $I = \frac{1}{2}$	100
Figure 2.10	Spin levels of $S=1$ (a) without ZFS (b) with ZFS showing allowed transitions and (c) with ZFS $\gg \hbar\nu$ showing forbidden transitions	101
Figure 2.11	EPR Spectrometer	103

Figure 2.12	Set-up for dielectric characterisation -----	105
Figure 2.13	Piezo evaluation system -----	108
Figure 3.1	Ferroelectric hysteresis showing constriction on aging-----	116
Figure 3.2	XRD patterns of $\text{PSZTMn}_{0.005}\text{Nb}_x\text{O}_3$; $x =$ (a) 0, (b) 0.002, (c) 0.004, (d) 0.008, (e) 0.010, (f) 0.015-----	119
Figure 3.3	P-E loops of unaged (solid line) and aged (dotted line) samples of $\text{PSZTMn}_{0.005}\text{Nb}_x\text{O}_3$; $x =$ (a) 0, (b) 0.002, (c) 0.004, (d) 0.008, (e) 0.010, (f) 0.015-----	120
Figure 3.4	Observed (i) and Simulated (ii) EPR spectra of $\text{PSZTMn}_{0.005}\text{Nb}_x\text{O}_3$; $x =$ (a) 0, (b) 0.002, (c) 0.004, (d) 0.010 -----	122
Fig. 3.5	Splitting of energy levels in Mn^{4+} in the presence of (a) Higher Zero field splitting and (b) Lower Zero field splitting. [ZFS(a) \gg ZFS (b)] (c) Representative defect structure in B-site Mn-doped PZT -----	125
Figure 3.6	Dielectric and Piezoelectric properties of $\text{PSZTMn}_{0.005}\text{Nb}_x\text{O}_3$ -----	126
Figure 4.1	Temperature dependence of dielectric constant of (a) $\text{Pb}(\text{In}_{0.50}\text{Nb}_{0.50})\text{O}_3$ and (b) $\text{Pb}(\text{Sc}_{0.50}\text{Ta}_{0.50})\text{O}_3$ -----	133
Figure 4.2	One octant of unit cell of the Perovskite -----	135
Figure 4.3	Schematic bonding in $\text{Pb}(\text{B}'\text{B}'')\text{O}_3$ (a) $r_{\text{B}'} > r_{\text{B}''}$, (b) $r_{\text{B}'} < r_{\text{B}''}$ -----	137
Figure 4.4	X-ray diffraction patterns of $(\text{Ba}_{1-x}\text{Pb}_x)(\text{In}_{0.50}\text{Nb}_{0.50})\text{O}_3$; $x =$ a) 0, b) 0.1, d) 0.3, f) 0.5, h) 0.8, i) 1.0 (* - pyrochlore phase) ----	139
Figure 4.5	(A) The Resultant powder X-ray diffraction profile fits to $\text{Ba}_2\text{InNbO}_6$. The refinement statistics at convergence were $R_{\text{wp}}=7.5$, $R_p=5.4$, $\chi^2 = 1.2$; (B) The Resultant Powder X-Ray diffraction profile fits to $\text{Pb}(\text{In}_{0.50}\text{Nb}_{0.50})\text{O}_3$. The refinement statistics at convergence were $R_{\text{wp}}=8.0$, $R_p=6.4$, $\chi^2 = 2.4$ -----	140
Figure 4.6	Raman spectra of $(\text{Ba}_{1-x}\text{Pb}_x)(\text{In}_{0.50}\text{Nb}_{0.50})\text{O}_3$, where $x =$ a) 0, b) 0.1, c) 0.2, d) 0.3, e) 0.4, f) 0.5, g) 0.6, h) 0.8, i) 1.0. Inset of Fig. 2(A) shows Raman spectra of wave number region 40 – 80 cm^{-1} -----	145
Figure 4.7	Representative structural fragment in the complex perovskite along $\langle 111 \rangle$ -----	146
Figure 4.8	Composition dependence of (A) FWHMs of A_{1g} and E_g modes, (B) wavenumber (ω) of $F_{2g}(2)$ mode and (C) ratio of intensities $I_{F_{2g}(2)}/I_{F_{2g}(1)}$ for $(\text{Ba}_{1-x}\text{Pb}_x)(\text{In}_{0.50}\text{Nb}_{0.50})\text{O}_3$ -----	148
Figure 4.9	Deconvoluted Raman spectrum of $(\text{Ba}_{0.2}\text{Pb}_{0.8})(\text{In}_{0.50}\text{Nb}_{0.50})\text{O}_3$ -----	149

Figure 4.10	Raman spectra of $(\text{Ba}_{1-x}\text{Pb}_x)[\text{In}_{0.50}(\text{Sn}_{0.03}\text{Nb}_{0.476})]\text{O}_3$, where $x = \text{a)0, b)0.1, c)0.2, d)0.3, e)0.4, f)0.5, g)0.6, h)0.8, i)1.0$. Inset of Fig. 6(A) shows Raman spectra of wave number region $40 - 80\text{cm}^{-1}$ -----	151
Figure 4.11	Composition dependence of (A) FWHMs of A_{1g} and E_g modes, (B) wavenumber (ω) of $F_{2g}(2)$ mode and (C) ratio of intensities $I_{F_{2g}(2)}/I_{F_{2g}(1)}$ for $(\text{Ba}_{1-x}\text{Pb}_x)[\text{In}_{0.50}(\text{Sn}_{0.03}\text{Nb}_{0.476})]\text{O}_3$ --	152
Figure 4.12	Dielectric permittivity as a function of temperature for (A) $\text{Pb}(\text{In}_{0.50}\text{Nb}_{0.50})\text{O}_3$;(B) $\text{Pb}[\text{In}_{0.50}(\text{Sn}_{0.03}\text{Nb}_{0.476})]\text{O}_3$;(C) $(\text{Ba}_{0.2}\text{Pb}_{0.8})(\text{In}_{0.50}\text{Nb}_{0.50})\text{O}_3$;(D) $(\text{Ba}_{0.2}\text{Pb}_{0.8})[\text{In}_{0.50}(\text{Sn}_{0.03}\text{Nb}_{0.476})]\text{O}_3$ -----	153
Figure 5.1	Schematic diagram of the primitive cell of AFE and FE states -----	163
Figure 5.2	Ternary phase diagram for PbZrO_3 - PbTiO_3 - PbSnO_3 system. Red point indicated the composition chosen for this study -----	165
Figure 5.3	(A) XRD patterns and (B) plot of temperature dependent dielectric permittivity of (i) undoped PZST; (ii) Cu-doped PZST and (iii) Mn-doped PZST. Insets of (A) shows XRD patterns at 2θ between 26 and 36° and (B) those in the temperature region from 170°C to 225°C -----	168
Figure 5.4	Temperature dependent P-E curves of undoped PZST; where (a) 30°C , (b) 130°C , (c) 140°C , (d) 150°C . Respective I-E curves are shown in insets -----	169
Figure 5.5	Temperature dependent P-E curves of Cu-doped PZST; where (a) 30°C , (b) 130°C , (c) 140°C , (d) 150°C . Respective I-E curves are shown in insets -----	170
Figure 5.6	Temperature dependent P-E curves of Mn-doped PZST; where (a) 30°C , (b) 130°C , (c) 140°C , (d) 150°C . Respective I-E curves are shown in insets -----	171
Figure 5.7	Temperature dependent S-E curves at (a) 30°C , (b) 130°C and (c) 150°C , where (i) undoped PZST; (ii) Cu-doped PZST and (iii) Mn-doped PZST-----	172
Figure 5.8	Observed (i) and simulated (ii) EPR spectra of (A) Mn-doped PZST, (B) Cu-doped PZST; where P_D represents the lattice symmetry-attained defect dipole -----	174

- 1.1 Introduction to Ferroelectrics
- 1.2 Introduction to Relaxor Ferroelectrics
- 1.3 Introduction to Antiferroelectrics
- References

This chapter gives a brief introduction to ferroelectrics, relaxor ferroelectrics and antiferroelectric ceramics. A review on the defect chemistry, effect of point defects on ferroelectric aging, lattice dynamics and structural rearrangements in relaxor ferroelectrics, phase transformations and structural modulations in antiferroelectric ceramics has also been incorporated.

1.1 Introduction to Ferroelectrics

1.1.1 Perovskite structure

Most of the ferroelectric materials crystallise in the ABO_3 -type perovskite structure. The ideal ABO_3 perovskite structure can be described as a simple cubic unit cell with a large cation (A) on the corners, a smaller cation (B) in the body center and oxygens (O) in the centers of the faces as given in Fig.1.1. The structure is a network of corner-linked oxygen octahedra, with the smaller cation filling the octahedral holes and the large cation filling the dodecahedral holes^{1,2}. The perovskite structure have the flexibility to accommodate variety of the elements at the A and B-sites thereby leading to the large number of compounds having this or related structures.

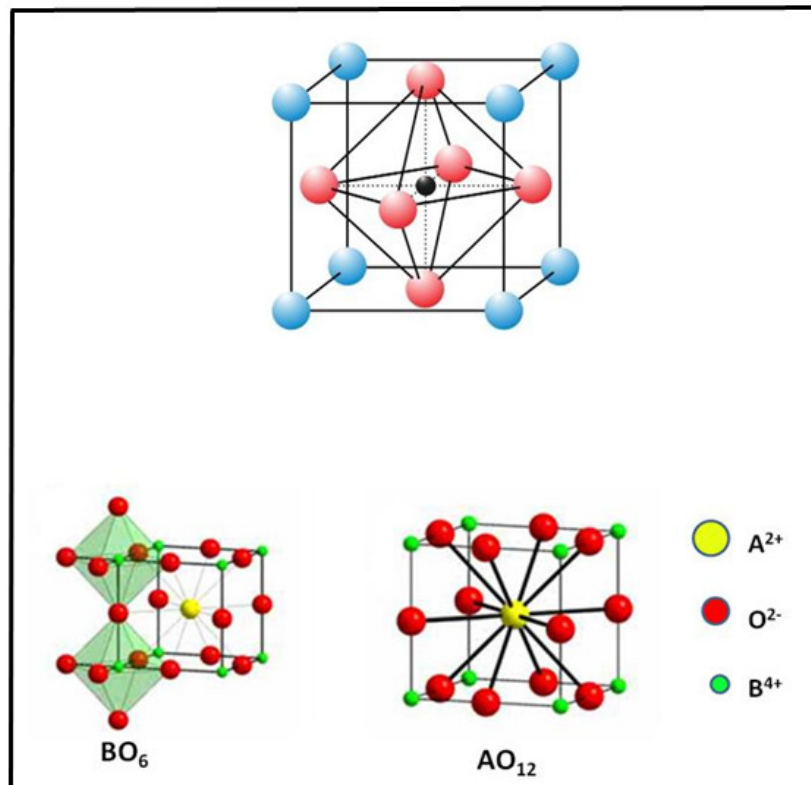


Figure 1.1 Ideal ABO_3 Perovskite Structure

The ideal cubic perovskite structure is not very common and structure of perovskite itself is slightly distorted. Various factors are responsible for the departure from ideal cubic symmetry such as size of constituent ions, deviations from the ideal composition, Jahn-Teller effect and etc. The relationship between relative ionic size of atoms and the stability and degree of distortion in the perovskite structure is described by Goldschmidt's tolerance factor 't',

$$t = \frac{r_A + r_B}{\sqrt{2}(r_B + r_O)} \quad (1.1)$$

where, r_A is the ionic radius of A-cation, r_B is the ionic radius of B-cation and r_O is the ionic radius of oxygen respectively. The ideal cubic perovskite like SrTiO_3 has 't' = 1.00. In practice, those structures whose tolerance factor 't' is about 0.95-1.0 are cubic and those with lower and higher values are distorted. Distortion in cubic perovskites is associated with lowering of symmetry of the unit cell associated with the displacement of cations relative to anions. Such distortions in perovskite structure are the reason for development of Spontaneous Polarisation, \mathbf{P}_S in ferroelectric materials. In BaTiO_3 , different ferroelectric phases are formed through the structural distortion of cubic perovskite along its edge, face diagonal and body diagonal respectively as shown in Fig. 1.2.

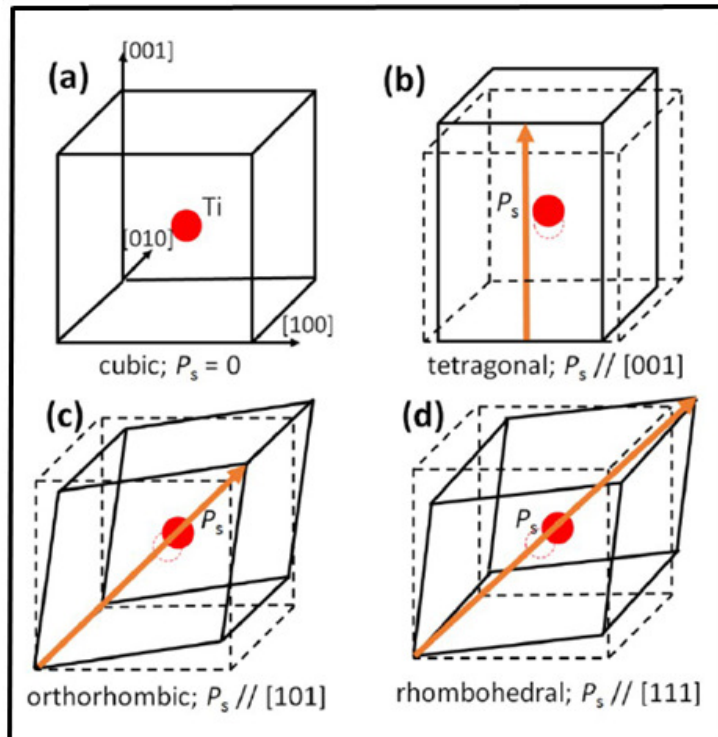


Figure 1.2 Spontaneous polarisation directions (indicated by arrows) in a typical ABO_3 unit cell $BaTiO_3$ (a) cubic (reference) (b) tetragonal (c) orthorhombic and (d) rhombohedral

[Source: B. Jaffe et al, *Piezoelectric Ceramics*, 1971].

1.1.2 Chemical bonding in perovskites

An ABO_3 -type perovskite has principal bonds between A/B cations and oxygen. The different types of bonds present in perovskite are (i) $A^{2+} - O^{2-}$ σ -bond (ii) $B^{4+} - O^{2-}$ σ -bond and (iii) $B^{4+} - O^{2-}$ π -bond depending on the type of B-cation (Fig. 1.3). The σ -bond between A-cation and oxygen is formed by overlap of $2p$ -orbital of oxygen with np or ns -orbital of A-cation.

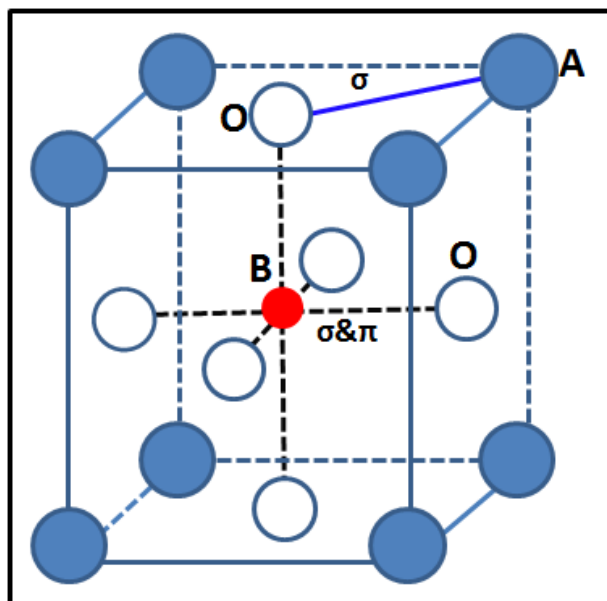


Figure 1.3 Representative σ and π bonding in a Perovskite Structure

Chemical bonds (σ , π) between B-cation and oxygen can be described by using molecular orbital concept in oxygen octahedron, BO_6 . Schematic representation of molecular orbital approach for B-O bond is given in Fig.1.4. Linear combination of $2s$ and $2p$ -orbitals of oxygen form 6 orbitals of a_{1g} , e_g and t_{1u} symmetries. These orbitals forms σ -bonds with B-cationic orbitals of same symmetries, $nd_{x^2-y^2}$, nd_z^2 (e_g), $(n+1)s$ (a_{1g}) and $(n+1)p$ (t_{1u}). Among the five d-orbitals of B-cation, $d_{x^2-y^2}$ and d_z^2 forms σ -bonds and d_{xy} , d_{xz} , d_{yz} orbitals involved in π -bonding. The d_{xy} , d_{xz} and d_{yz} orbitals form π -bonds with molecular orbitals of oxygen of t_{2g} symmetry.

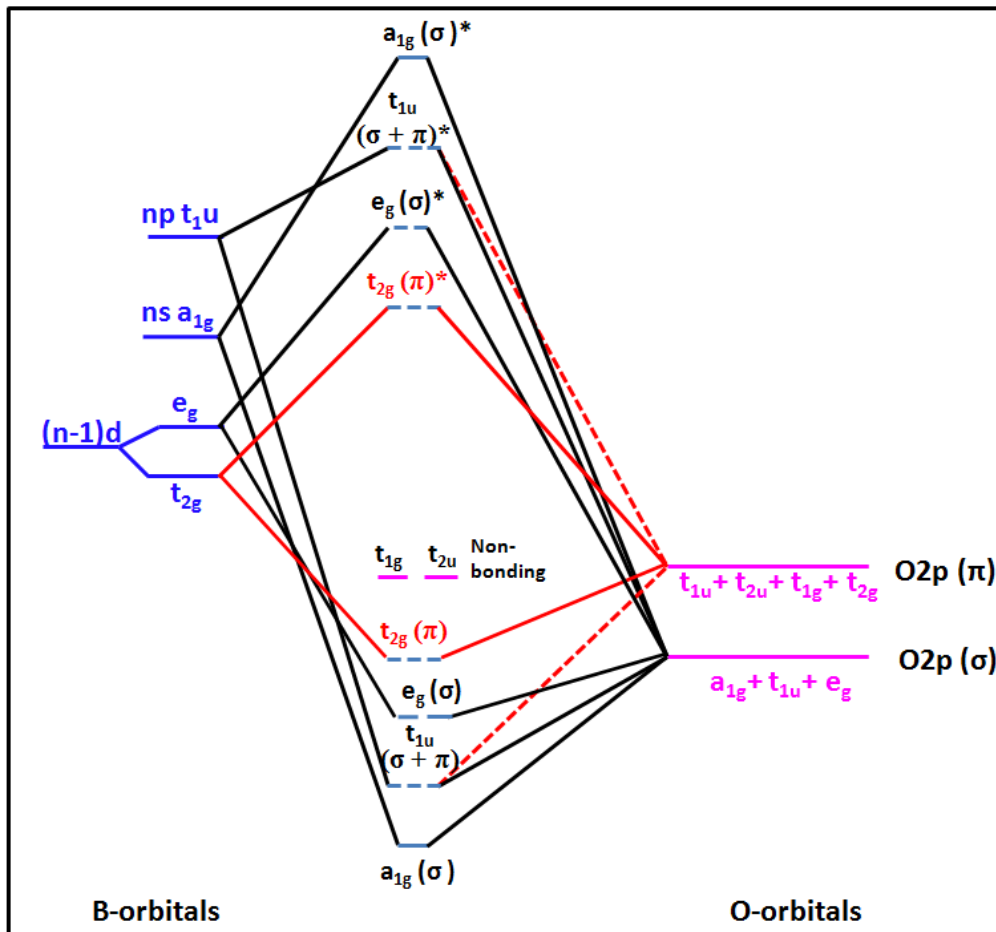


Figure 1.4 Molecular orbital diagram of BO_6 octahedron in ABO_3 perovskite

1.1.3 Ferroelectric polarisation

Ferroelectric materials undergo a phase transition from a non ferroelectric cubic crystalline phase into ferroelectric phase at a temperature called Curie point T_c . Consider the phase transition in lead titanate as shown in Fig. 1.5. Below Curie point T_c , as a result of phase transformation, B-site ion displaced with respect to O-atoms in the same plane, structure is not centrosymmetric any longer and crystal is polarised due to the formation of dipoles. The sum of the dipole moments in entire unit cell volume gives the

spontaneous polarisation (\mathbf{P}_S). Spontaneous polarisation possesses different orientations dictated by the crystal symmetry. By application of an electric field, the dipoles may be switched between these orientations. Generation of spontaneous polarisation due to the phase transformation creates strong anomalies in dielectric, elastic and thermal properties of material along with dimensional change. Strain associated with the change in dimension of the unit cell is called spontaneous strain.

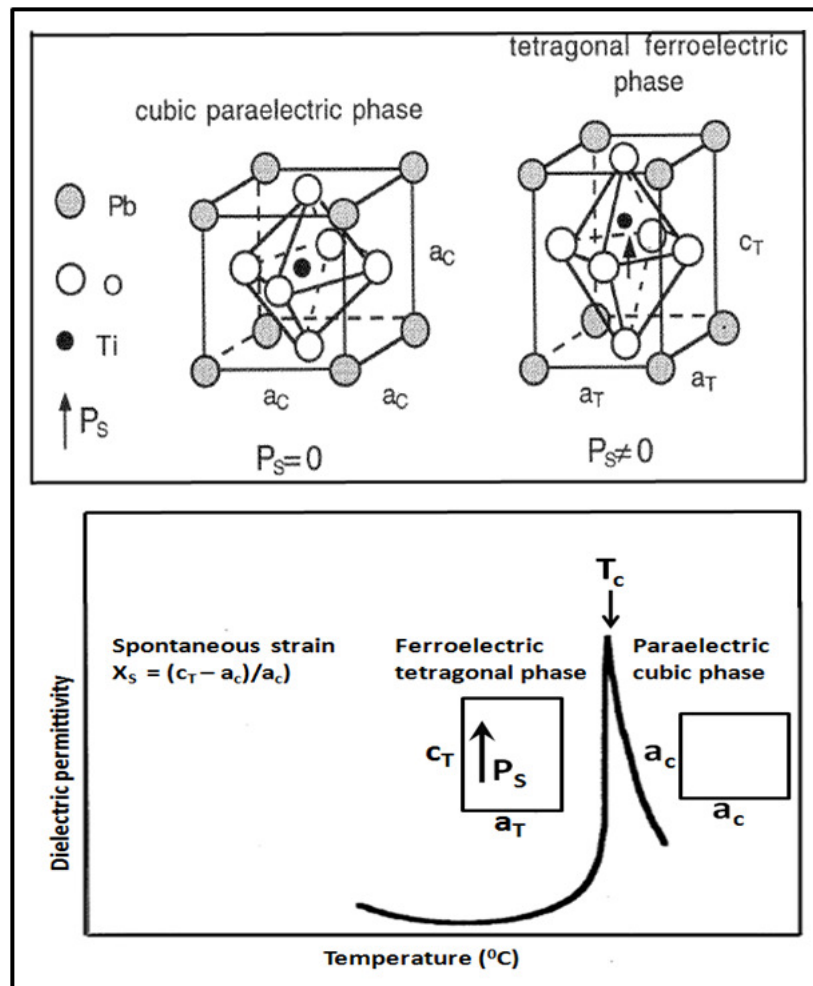


Figure 1.5 Illustration of the changes in a ferroelectric material which transforms from cubic paraelectric phase into tetragonal ferroelectric phase with temperature

Ferroelectric materials exhibit a sharp peak in dielectric permittivity (ϵ_r) near the Curie point, T_c . Upon reaching the maximum value of ϵ_r near T_c , a phase transition to paraelectric state occurs and the magnitude of ϵ_r drops as shown in Fig. 1.6. Above the T_c , in the paraelectric state, the dielectric permittivity ϵ_r decreases sharply as a function of $\frac{1}{T}$, following the Curie-Weiss law:

$$\epsilon_r = \frac{C}{T - T_c} \quad (1.2)$$

where ϵ_r is the dielectric permittivity, 'C' is a constant, T_c is the Curie point and T is the absolute temperature. The value of the constant 'C' is determined by a plot of $\frac{1}{\epsilon_r}$ versus T . The plot will be straight line with a slope of $\frac{1}{C}$ and an intercept T_0 , Curie temperature which is slightly different from the measured T_c as shown in Fig. 1.6.

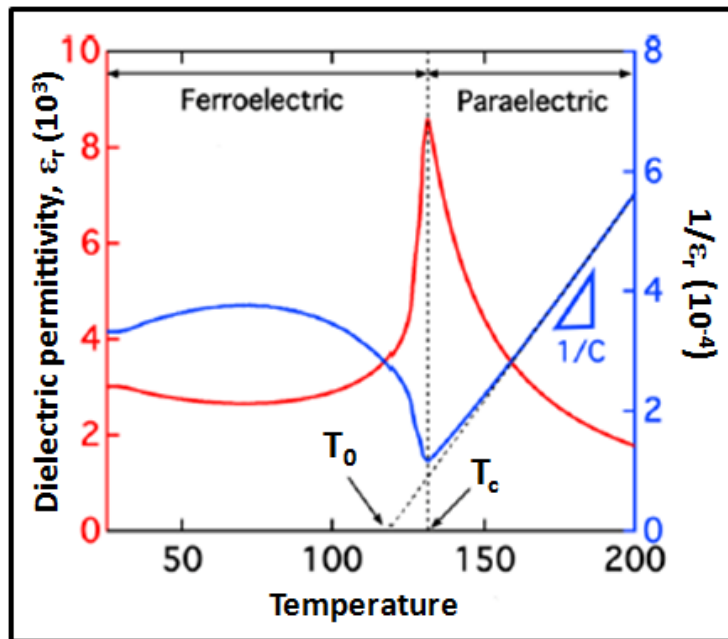


Figure 1.6 Curie- Weiss plot for typical ferroelectric BaTiO₃

1.1.4 Ferroelectric domains

Ferroelectric domains form to minimize elastic energy associated with mechanical stress due to dimensional change during paraelectric-ferroelectric phase transition. Ferroelectric domains are regions in the crystal having spontaneous polarisation in the same direction. Ferroelectric domains are separated by a region known as ferroelectric domain walls. The types of domain walls formed depend on the symmetry of both the nonferroelectric and ferroelectric phases of the crystal. The domain wall separating the domain regions having antiparallel orientation of spontaneous polarisation is known as 180° domain wall and that between regions of perpendicular orientations is 90° domain wall (Fig. 1.7). In a typical ferroelectric PbTiO_3 , 180° domain walls are ferroelectric and 90° domain walls are both ferroelectric and ferroelastic since 90° domain walls differ not only in the direction of the spontaneous polarisation but are also strain producing (Fig. 1.8).

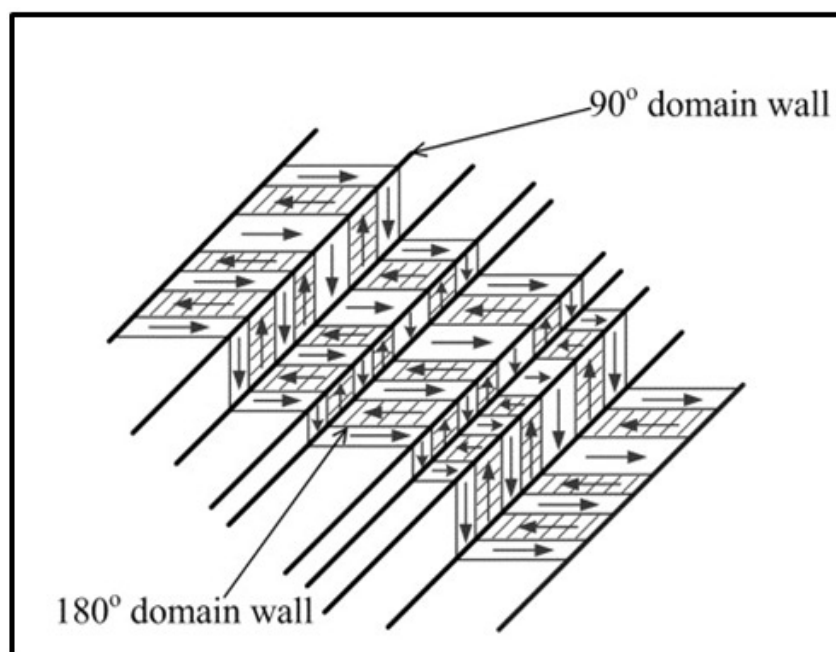


Figure 1.7 Schematic representations of 180° and 90° domains and domain walls

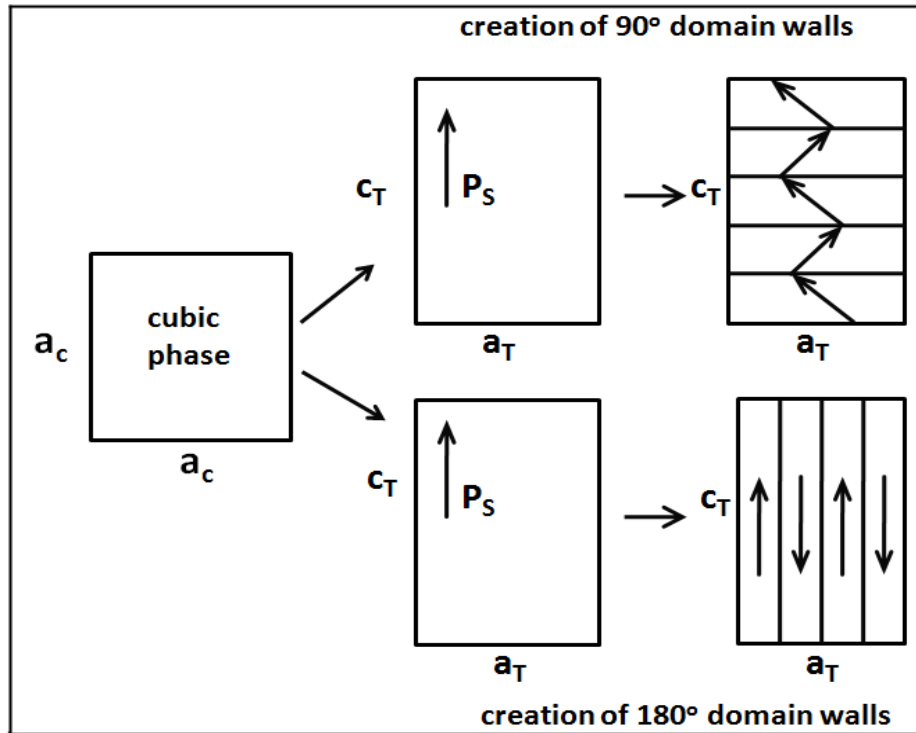


Figure 1.8 Formation of 90° and 180° ferroelectric domain walls

1.1.5 Poling of ferroelectrics

The spontaneous polarisation in a ferroelectric material is not uniformly oriented along one direction throughout the crystal. Polycrystalline ferroelectric ceramics are divided into several domains of different or random orientation of spontaneous polarisation. Due to this random distribution of spontaneous polarisation net polarisation is zero and material will not be piezoelectric. On application of a strong electric field these randomly distributed domains can reorient along the direction of the field at temperatures close to T_c , giving a remnant polarisation \mathbf{P}_R and exhibit piezoelectric properties. This process is known as poling.

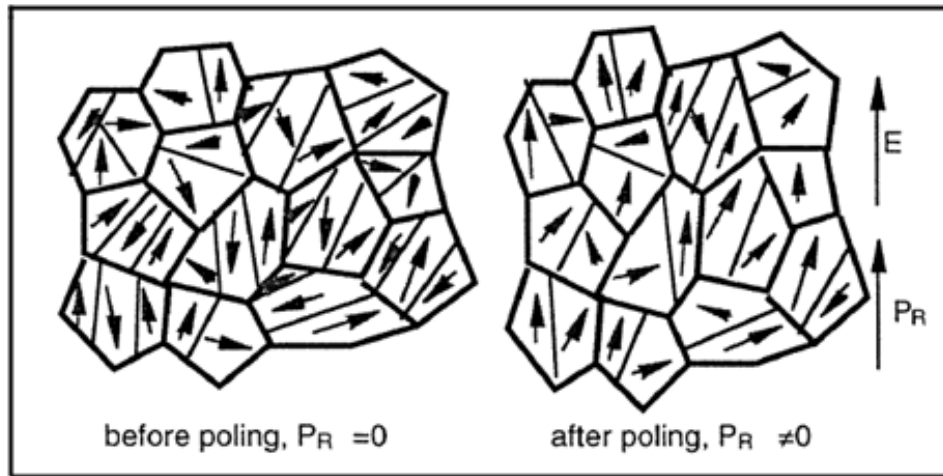


Figure 1.9 Polycrystalline ferroelectric with random orientation of grains before and after poling

[Source: D. Damjanovic, *Rep. Prog. Phys.*, 61(1998) 1267-1324].

1.1.6 Ferroelectric properties

1.1.6.1 Polarisation-Electric field hysteresis curve

Polarisation saturation and reversal on application of an electric field is an important characteristic of ferroelectric materials. A typical polarisation-electric field (P-E) loop of ferroelectric material is shown in Fig.1.10, where point 'C' corresponds to alignment of all domains in one direction and saturates at 'D' (P_S). E represents the polarisation value at zero field known as remnant polarisation (P_R). For zero polarisation state, the field must be reversed (point 'F') and this field is called as coercive field E_C . Further increase of the field in the negative direction will cause alignment of dipoles in opposite direction and then saturation (point 'G'). The field strength is then reduced to zero and reversed to complete the cycle^{3,4}.

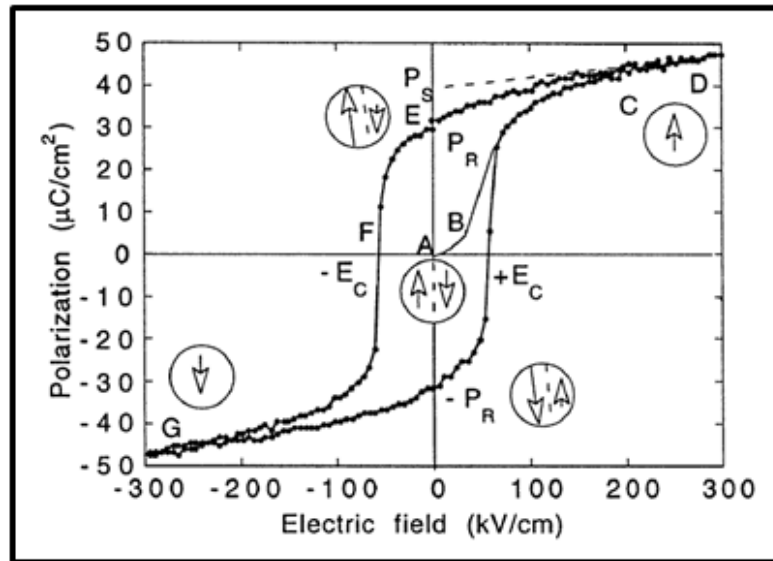


Figure 1.10 Ferroelectric Polarisation-Electric field hysteresis loop

[Source: D. Damjanovic, *Rep. Prog. Phys.*, 61(1998) 1267-1324]

1.1.6.2 Strain-Electric field curve

Polarisation switching by an external electric field leads to strain in ferroelectric materials. A typical strain- electric field (S-E) loop of ferroelectric material resembles the shape of butterfly as shown in Fig.1.11. When external field is zero, the strain of the crystal is zero. As electric field increased strain increases nonlinearly along the curve 'A' and reaches maximum physical strain value at point 'B'. When electric field decreases, strain also decreases along curve 'C'. As the electric field decreased to critical value in negative direction known as coercive field (E_C), polarisation reversal is occurs. After polarisation reversal, as electric filed increases in negative direction, the material found to expands again along curve 'E' until it reaches its physical strain limit at point 'F'. When the electric field is reversed again the same hysteretic behavior produced and butterfly loop resulted^{5,6}.

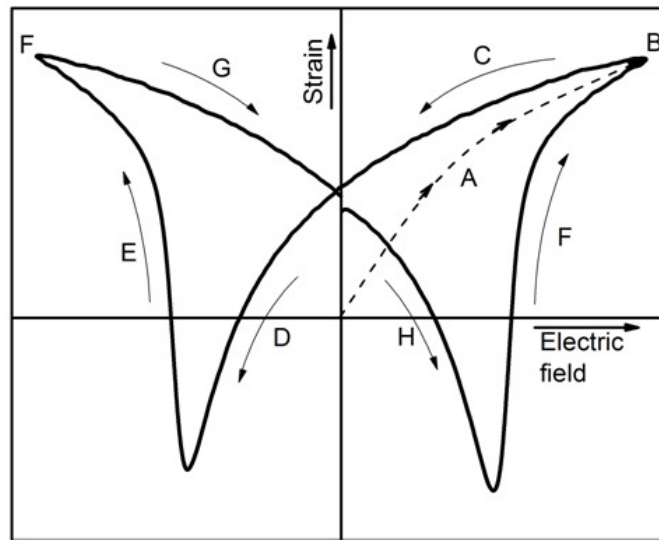


Figure 1.11 Ferroelectric Strain-Electric field hysteresis loop

If ferroelectric ceramics exhibits electrostrictive effect, induced strain is independent of polarity of the electric field and is proportional to square of the electric field. The electrostrictive effect can be explained as an electric field dependent contribution of the non linear strain to the linear piezoelectric effect. Electric field dependence of polarisation and strain in electrostrictive materials are shown in Fig.1.12. The electrostriction induces an expansion of materials in the direction of field regardless of its polarity, and when the field is removed this expansion relaxes back to zero.

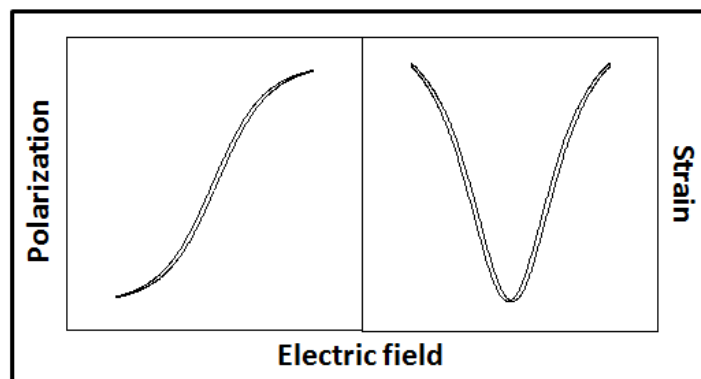


Figure 1.12 Electric field dependence of polarisation and strain in electrostrictive material

1.1.7 Lead Zirconate Titanate (PZT) solid solution

Most of the piezoelectric actuators, transducers, etc. are based on ferroelectric Lead Zirconate Titanate (PZT) ceramics due to their superior piezoelectric properties over an extensive range of operation temperature. Furthermore, presence of nearly temperature independent Morphotropic Phase Boundary (MPB) where it provide maximum electromechanical properties and easy manipulation of properties near this region driven interest in development of ceramic materials at or near this region. Phase diagram of Lead Zirconate-Lead Titanate is shown in the Fig.1.13.

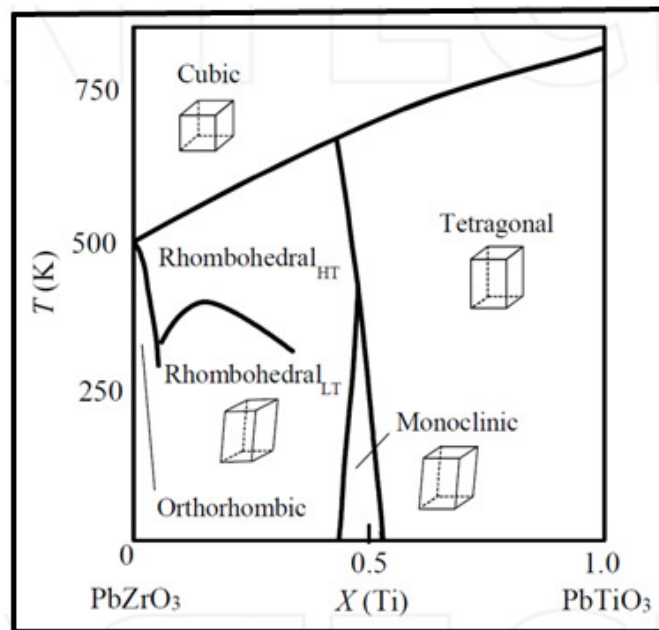


Figure 1.13 Phase diagram of PZT solid solution

At high temperature, structure of composition is cubic and is paraelectric. Compositions which are moves to Ti-rich side are tetragonal while those which are Zr-rich side phase transformation scenario are more complex. At higher Zr-content and at room temperature the structure is orthorhombic and when Ti-content increased structure become rhombohedral

with another phase transition from a high to a low temperature rhombohedral structure as shown in Fig.1.13. At a particular Zr/Ti ratio near the centre of the phase diagram a temperature independent boundary exists which separates the tetragonal and rhombohedral phase known as MPB. The MPB has a finite width and in compositions within this region, tetragonal, rhombohedral monoclinic phases coexist. The dielectric and piezoelectric properties such as piezoelectric coefficients, electromechanical coupling coefficients, dielectric permittivity and remnant polarisation attains maximum values in the MPB region. Maximum values of all properties at MPB region is attributed to the maximum polarisation in the vicinity of MPB region. Noheda et al^{7,8} discovered a monoclinic phase, between rhombohedral and tetragonal phases near the MPB in PZT and this monoclinic symmetry allows polarisation rotation leading to enhanced piezoelectric and dielectric properties.

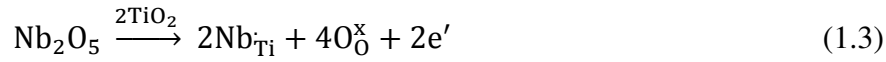
1.1.7.1 'Soft' and 'Hard' PZT- Effects of defects

Usually PZT is not used in its pure form for applications. In order to achieve desired properties for specific applications, PZT has been compositionally modified by substitution of various impurities to shift T_c and/or modify dielectric permittivity and electromechanical characteristics^{2,4,9,10,13,14}. Impurities can be isovalent (Ba^{2+} , Sr^{2+} at Pb^{2+} -site or Hf^{4+} , Zr^{4+} , Sn^{4+} at Ti^{4+} -site) or aliovalent (Mn^{3+} , Fe^{3+} , Nb^{5+} at Ti^{4+} -site or Na^{+1} , K^{+1} , Bi^{3+} , La^{3+} at Pb^{2+} -site). Aliovalent impurities are classified as acceptors and donors according to their valency. Acceptor ions have lower positive charge than the replaced ion and donors have higher positive charge than the substituted site. According to the range of properties obtained by doping, doped PZT compositions are categorised into two, 'hard' and 'soft' PZT. The changes in characteristics of modified PZT compositions are attributed to the

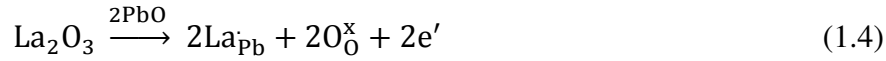
defects formed in the lattice as a part of charge compensation through these doping. Defects are represented by using Kroger-Vink notations¹¹.

Donor dopants such as La^{3+} in the place of Pb^{2+} or Nb^{5+} in the place of (Zr^{4+} , Ti^{4+}) supply extra electrons to the structure. Depending on the concentrations of donors, different charge compensation mechanisms operate. For small concentrations, charge compensation is achieved by formation of electrons as given below in equations 1.3 and 1.4.

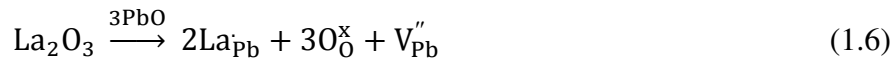
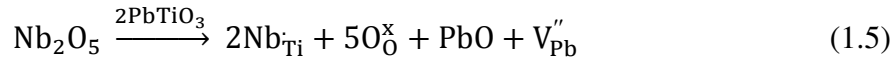
i) for B-site substitution,



ii) for A-site substitution,

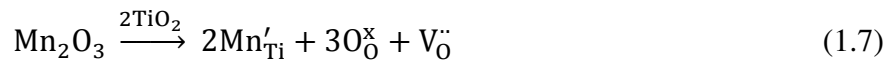


where Nb_{Ti} , La_{Pb} represent typical singly positively charged donor doped site with respect to neutral lattice and O_O^\times represents neutral lattice oxygen. For larger concentrations, A-site lead-vacancies are created for charge compensation as given below in equations 1.5-1.6.



where V_{Pb}'' represents a typical doubly negatively charged lead vacancy with respect to neutral lattice. The formed lead vacancies help to reduce the internal stresses in the ceramic and make domain walls more mobile^{2,9,12}. This leads to marked changes in characteristics like high dielectric permittivity (ϵ_r), dielectric loss ($\tan\delta$) and lower coercive field. These are easy to pole and depole and possess high piezoelectric coefficients, hence named '*Soft*' PZT.

The acceptor ions, for example, replacing Pb^{2+} with monovalent cations such as Na^{+1} or replacing $(\text{Zr}^{4+}, \text{Ti}^{4+})$ with Mn^{3+} , Fe^{3+} contributes fewer electrons than the ion it replaces. Lower valent ions like Fe^{3+} , Mn^{3+} and Al^{3+} at the B-site which have similar ionic radii as that of Ti^{4+} are some examples of acceptor dopants. Acceptor doping will result in the increase of oxygen vacancies in the lattice according to the following equation.



Where Mn'_{Ti} represents a typical singly negatively charged acceptor-doped site, V''_{O} represents doubly positively charged oxygen vacancy with respect to neutral lattice and O^x_{O} represents neutral lattice oxygen. Compensating defects in acceptor-doped ferroelectric oxides is double positively charged oxygen vacancies (V''_{O}). This oxygen vacancy is mobile in the oxygen octahedra and forms defect dipoles of the type $[\text{M}'_{\text{Ti}} - \text{V}''_{\text{O}}]$ with singly negatively charged acceptor doped site (M'_{Ti})¹⁵⁻¹⁷. The resulting defect dipoles will pin the domain walls and favour a certain direction for spontaneous polarisation within domain^{4,13,14}. As a result of this domain pinning, it is difficult to pole and depole these compositions. Restriction in domain wall mobility results in 'hardening' of piezocharacteristics such as low dielectric permittivity, dielectric loss and lower values of piezoelectric coefficient (d_{33}), electromechanical coupling factor (k_p) and higher values of mechanical quality factor (Q_m). These compositions are named 'Hard' PZT.

1.1.8 Domain stabilization in 'Hard' ferroelectrics and its consequences

In the above section, it is shown that 'hardening' of ferroelectric characteristics by acceptor doping involves creation of oxygen vacancy in order to maintain charge neutrality. The charged defects favour particular direction for spontaneous polarisation. In 'hard' ferroelectrics the interaction

of mobile charged defects with the spontaneous polarisation leads to gradual stabilization of domain pattern in residing domains and immobilization of domain walls with time¹⁸⁻²². Gradual stabilization of domain patterns by charged defects generates internal bias (E_i) which manifests in pinched P-E hysteresis loop or displaced P-E hysteresis loop^{13,23,24} as shown in Fig. 1.14.

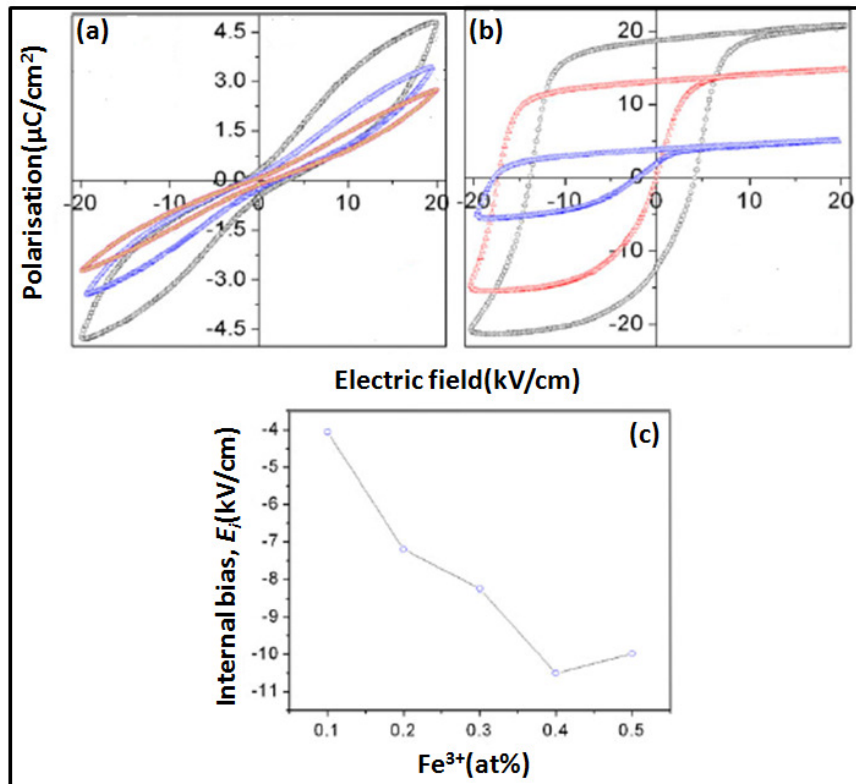


Figure 1.14 P-E hysteresis characteristics of unaged Fe^{3+} -doped PZT at room temperature for (a) unpoled (b) poled. Internal bias (E_i) at various Fe^{3+} concentrations given in (c)
 [Source: K. P. Rema et al, *J. Mater. Sci: Mater. Electron.*, 21(2010) 1149–1153].

The stabilization of domain configuration by defects influences ferroelectric properties. Ferroelectrics exhibit aging, the change of ferroelectric, dielectric, and piezoelectric properties with time even in the absence of external mechanical or electrical stimuli. Aging strongly influences

the device application of ferroelectrics, in particular the reliability^{25,26}. For e.g. P-E hysteresis characteristics of unaged and aged piezoelectrics are shown in Fig. 1.15. ‘Hard’ ferroelectrics show strong aging effects in both large and small signal properties¹⁸⁻²⁴. Aged ‘hard’ ferroelectrics exhibit pinched polarisation-hysteresis loop in unpoled state or displaced hysteresis loop in poled state as shown in Fig. 1.15. Decrease in small signal properties like dielectric and piezoelectric constant are also observed in aged ferroelectrics.

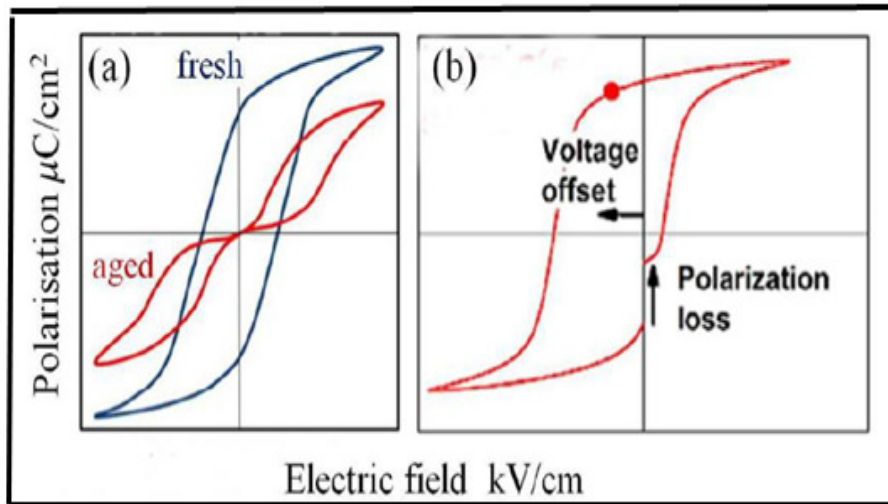


Figure 1.15 P-E hysteresis loops before and after aging (a) unpoled (b) poled

In acceptor doped ferroelectrics, the aging process is related to the presence of mobile defects like oxygen vacancies. In donor doped ferroelectrics, cation vacancies are created to maintain the charge neutrality described as in equations 1.5 and 1.6 which are immobile since in the perovskite structure cations have oxygens in the immediate coordination sphere and are separated from the same kind of cations by a whole unit cell. Hence tendency for the formation of vacancy pairs like $[\text{La}_{\text{Pb}} - \text{V}_{\text{Pb}}'']'$ is less. Therefore domain walls are not pinned in donor-doped ferroelectrics due to which aging effects are not observed in ‘Soft’ PZT^{4,28-32}.

1.1.8.1 Domain stabilization theories

In ferroelectrics, aging is attributed to migration of charged defects like oxygen vacancy, V_O^\bullet and their interaction with spontaneous polarisation. Three major mechanisms have been proposed for stabilization of domain configuration by the charged defects¹⁸⁻²⁸. They are (i) grain boundary effect (ii) domain-wall effect and (iii) volume effect.

1.1.8.1.1 Grain boundary effect

This effect is related to interface effect in which ions, vacancies or electrons diffuse to grain boundaries and lead to generation of space charges in the grain boundary region. Segregation of secondary phases or dopants at the grain boundary also generates space charge at the interface. The space charge layer will influence the domain configurations in course of time along a preferred direction of polarisation. After the polarisation reorientation processes the space charge field will tend to restore the original direction of polarisation in the domains³⁴⁻³⁷.

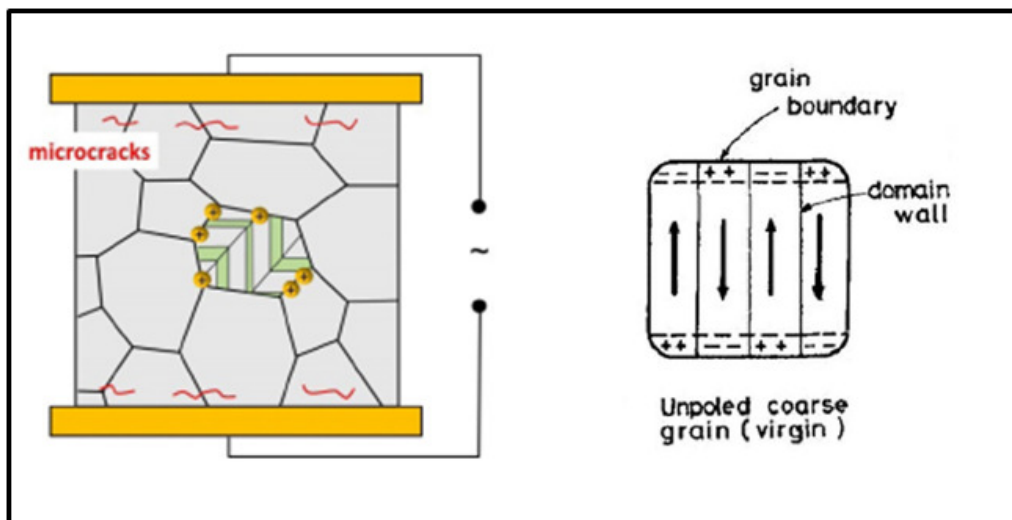


Figure 1.16 Schematic representation of grain boundary effect

[Source: Y. A. Genenko et al, *Mater. Sci. Eng., B* 192(2015) 52-82]

1.1.8.1.2 Domain wall effect

This model relates to the stabilization of domain-wall configuration by diffusion of defects into domain walls³⁸⁻⁴⁰. Defects such as electrons or vacancies diffuse into the domain wall in course of time, pinning the domain walls and stabilizing the domain pattern. Since they immobilize domain-wall contribution, the ferroelectric properties are drastically decreased.

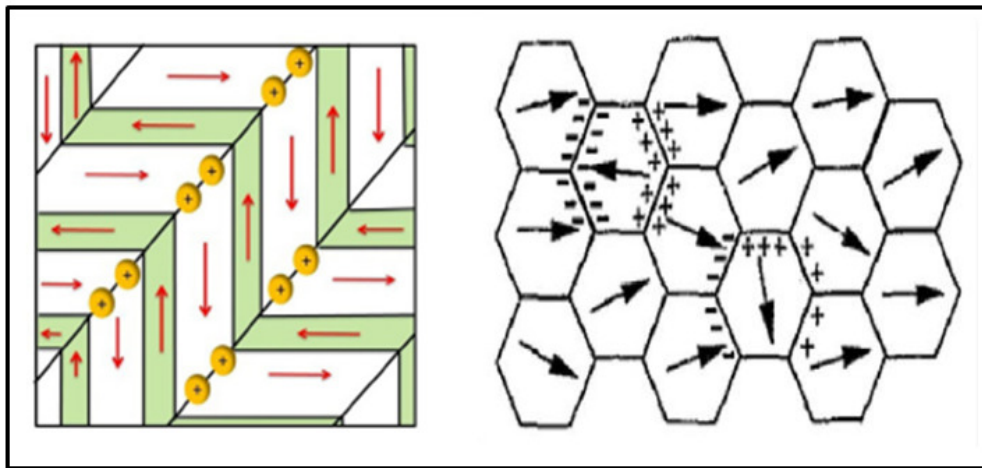


Figure 1.17 Schematic representation of domain wall effect

[Source: Y. A. Genenko et al, *Mater. Sci. Eng., B* 192(2015) 52]

1.1.8.1.3 Volume effect

On B-site acceptor doping, as represented in equation 1.7 oxygen vacancies ($V_{\text{O}}^{\bullet\bullet}$) are formed. Due to the coulombic interaction, defect dipoles of the type $[M'_{\text{Ti}} - V_{\text{O}}^{\bullet\bullet}]$ are formed as shown in Fig.1.18. In the course of aging, these defect dipoles are found to slowly reorient to the energetically more favourable direction. By orientation dependent EPR signal studies in polycrystalline BaTiO_3 , W. L. Warren and R. Ramesh⁴¹ et al proposed that reorientation of defect dipoles are dictated by the direction of spontaneous polarisation. This reorientation of defects along the spontaneous polarisation

stabilizes the domain configuration. Reorientation of defect associates can be easily possible by migration of oxygen ion from one site to another adjacent site within the coordination sphere of that acceptor-doped site since diffusion lengths are of only a few lattice constants. Thus migration of defects plays an important role in volume effect model which can be explained by symmetry conforming short range ordering (SC-SRO) mechanism of point defects

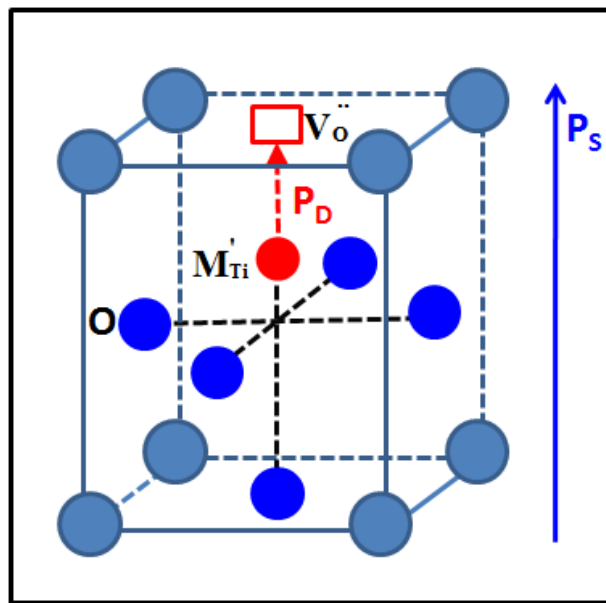


Figure 1.18 Schematic representation of volume effect

1.1.9 Symmetry Conforming - Short Range Ordering of point defects

Symmetry Conforming Short Range Ordering mechanism^{42-44,46} relates to the tendency of the defect dipoles in the lattice in attaining the symmetry of crystal lattice.

Consider the phase transition in acceptor (M^{3+})-doped ferroelectric material from cubic paraelectric to tetragonal ferroelectric phase. In order to maintain the charge neutrality, in such systems oxygen vacancy is created as explained in equation 1.7. Hence defect dipoles of the type $[M'_{Ti} - V_O^{\bullet\bullet}]$ are

formed. Above Curie point, in the cubic paraelectric state the six oxygen atoms in oxygen octahedra are equivalent about the central acceptor ion. So the probability of finding an oxygen vacancy is equal at all the six sites of octahedron as shown in the Fig. 1.19(a) and can be expressed as $P_1^V = P_2^V = P_3^V = P_4^V = P_5^V = P_6^V$ (P_i^V where $i=1-6$, oxygen sites in octahedron). So in the cubic paraelectric state, defect and crystal have cubic symmetry as shown in the Fig. 1.19(a). Small and large squares represent defect symmetry and crystal symmetry respectively.

When the crystal undergoes phase transition to tetragonal ferroelectric phase through the Curie point, central positive ion and oxygen ions in the octahedron are displaced relative to each other with a spontaneous polarisation (\mathbf{P}_s) along the $\langle 001 \rangle$ of tetragonal phase as shown in the Fig.1.19(b). Since transition from cubic paraelectric to tetragonal ferroelectric state is a diffusion less process, defect structure keep the cubic symmetry even though crystal symmetry changed to tetragonal phase as seen from the Fig.1.19(b). As a result, the fresh ferroelectric sample has a cubic defect symmetry, which does not match with the tetragonal crystal symmetry and such a state is energetically unstable. In tetragonal structure, central acceptor ion is situated at an off center position along axial direction and close to site 1 in octahedra compared to site 6. There is a large probability of oxygen vacancy at site 1 is due to a coulombic attraction between positively charged oxygen vacancy and negatively charged acceptor doped site. Therefore the defect probability change to $P_1^V > P_2^V = P_3^V = P_4^V = P_5^V > P_6^V$. Therefore in order to attain such a defect probability, migration of oxygen vacancy from one site to another required and this process demands time duration. During aging, defect symmetry conforms to the crystal symmetry by migration of oxygen vacancy attain a stable state as shown in the Fig.1.19(c).

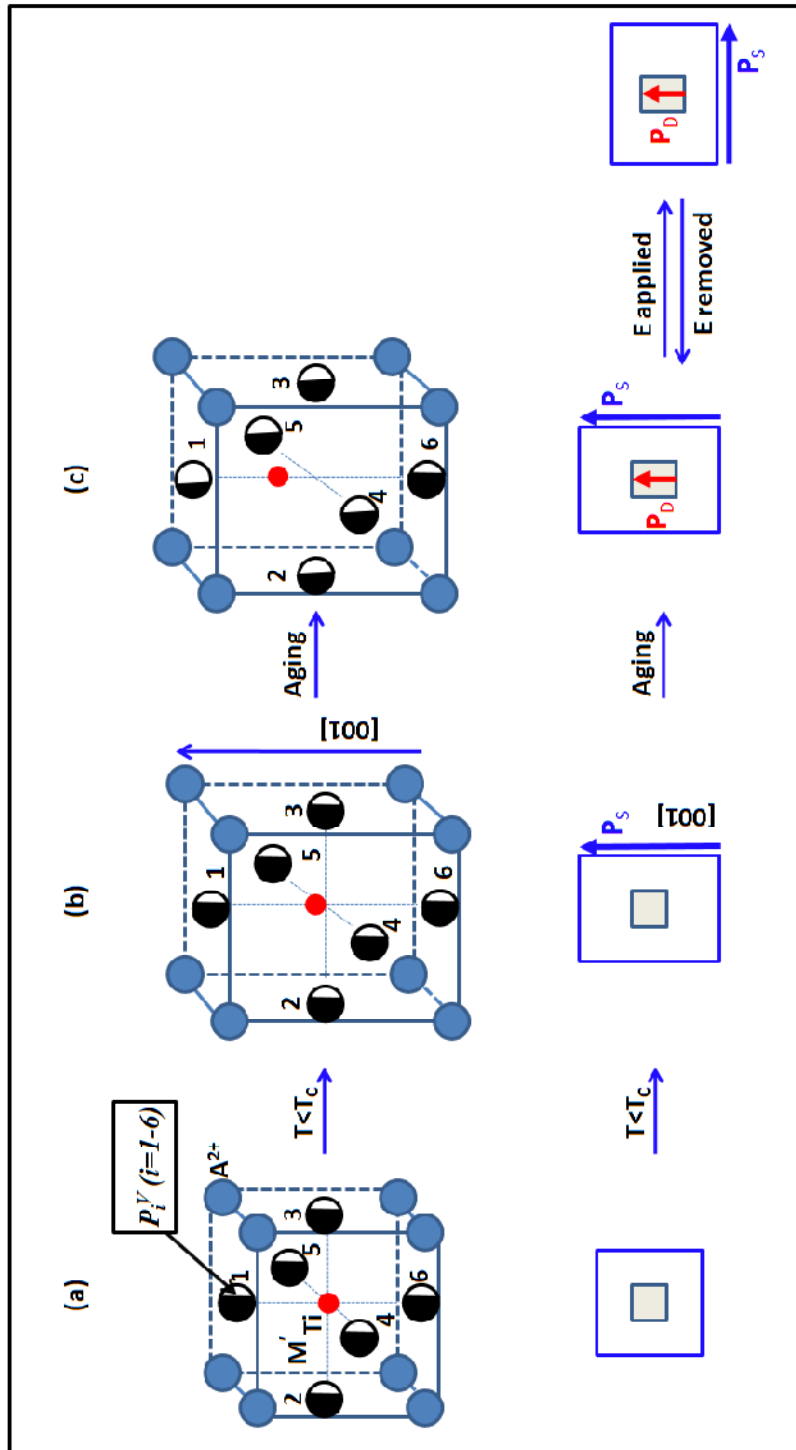


Figure 1.19 Tetragonal crystal symmetry and the related defect symmetry in unaged and aged state. Circle with maximum unshaded are represents the most probable site of oxygen vacancy.

[Source: Z. Feng and X. Ren, *Phys. Rev. B*, 77(2008)134115]

This symmetry adopted defects possess a dipole moment and a polarisation (\mathbf{P}_D) oriented along the direction of spontaneous polarisation (\mathbf{P}_S) of the residing domain. Thus orientation of defects along the spontaneous polarisation stabilizes the domain configuration and then every domain in its thermodynamically stable state. When we apply an external electric field to this stable ferroelectric domain state, ferroelectric dipoles undergo switching as dictated by the symmetry of the crystal lattice. Switching of ferroelectric domains is fast and does not involve diffusion process or atomic rearrangement. By contrast the defect symmetry and defect polarisation \mathbf{P}_D is not switched by application of electric field since the switching involves diffusion. The nonswitched defect dipoles provide a restoring force to the switch back the ferroelectric dipoles when the electric field is removed gives rise to a double-hysteresis loop.

1.1.9.1 SC-SRO mechanism in rhombohedral and orthorhombic ferroelectrics

The SC-SRO mechanism operates in crystals of other symmetries also. For example, operation of SC-SRO mechanism in rhombohedral and orthorhombic symmetries⁴⁴. In the case of rhombohedral ferroelectrics (Fig. 1.20), after the phase transition defect probability change to $P_1^V = P_3^V = P_5^V > P_2^V = P_4^V = P_6^V$ and the polar defect symmetry in the aged state creates a defect polarisation \mathbf{P}_D aligning along \mathbf{P}_S direction, i.e., along $\langle 111 \rangle$. In the case of orthorhombic ferroelectrics (Fig. 1.21), after phase transition defect probability change to $P_1^V = P_3^V > P_5^V = P_4^V > P_2^V = P_6^V$ and aged state creates a defect polarisation \mathbf{P}_D aligning along \mathbf{P}_S direction, i.e., along $\langle 110 \rangle$. The defect polarisation \mathbf{P}_D provides a restoring force for a reversible domain switching in the both aged ferroelectric materials.

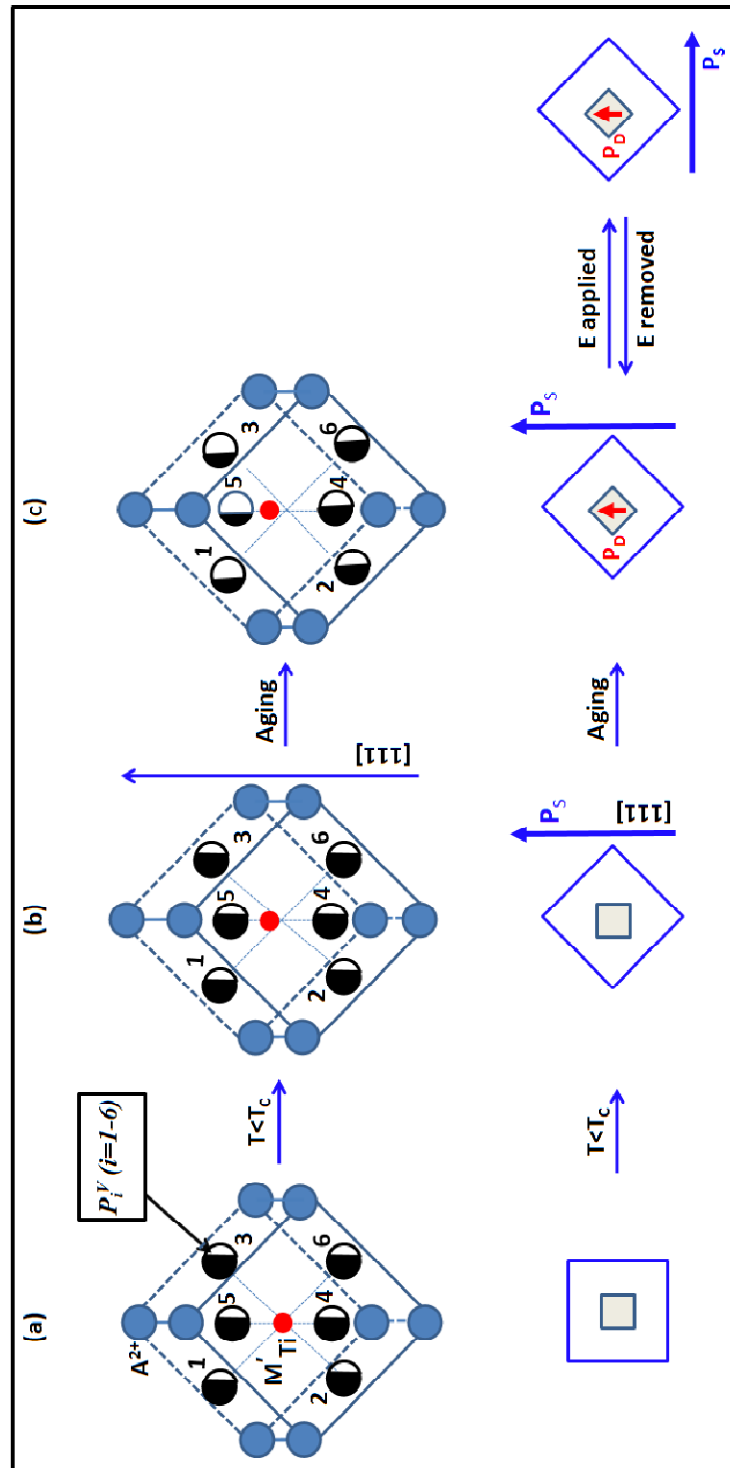


Figure 1.20 Rhombohedral crystal symmetry and the related defect symmetry in unaged and aged state. Circle with maximum unshaded area represents the most probable site of oxygen vacancy.

[Source: Z. Feng and X. Ren, *Phys. Rev. B*, 77(2008)134115]

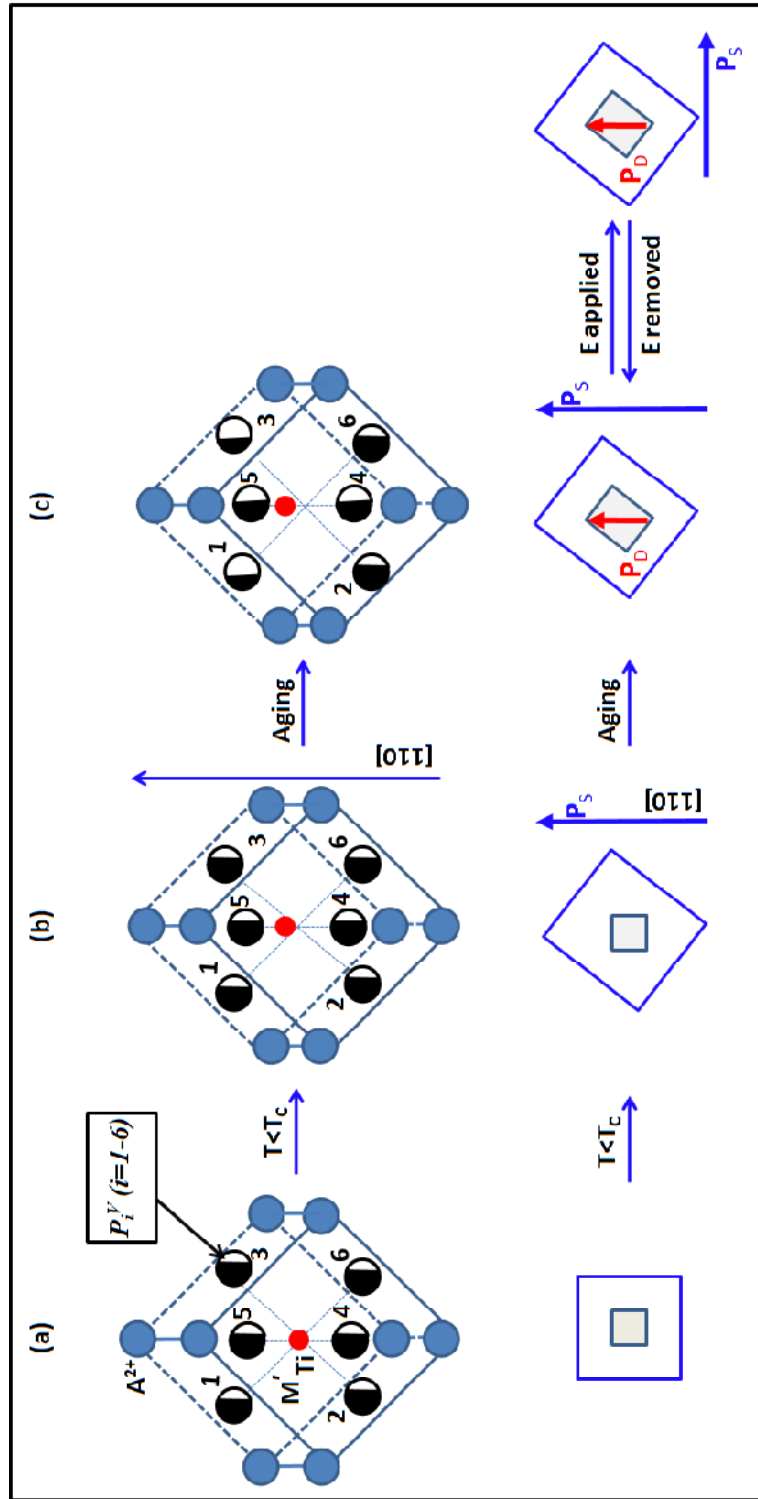


Figure 1.21 Orthorhombic crystal symmetry and the related defect symmetry in structure unaged and aged state. Circle with maximum unshaded area represents the most probable site of oxygen vacancy.

[Source: Z. Feng and X. Ren, *Phys. Rev. B*, 77(2008)134115]

1.1.10 Factors influencing SC-SRO mechanism

1.1.10.1 Locking of defect dipoles in the lattice

In some ‘hard’ ferroelectrics defect dipoles are locked in certain preferred direction leading to internal bias (E_i) which influences switching of ferroelectric domains^{24,47}. Internal bias for different B-site acceptor-doped PZT is given in Fig.1.22. It can be seen that internal bias (E_i) is highest in the case of Fe^{3+} for all concentrations. The lability of such formed defect dipoles also influences their short range ordering (SRO) rate.

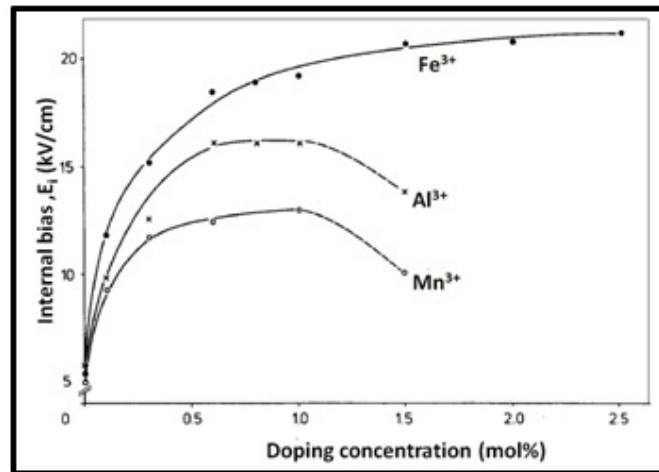


Figure 1.22 Dependence of internal bias, E_i on doping concentration of PZT ceramics in the unpoled aged state

[Source: K. Carl et al, *Ferroelectrics*, 17 (1978) 473-486].

Consider P-E and S-E curves of Mn^{3+} and Fe^{3+} -doped BST [(Ba_{0.80}Sr_{0.20})TiO₃] in aged state shown in the Fig.1.23. Typical P-E and S-E curves for acceptor-doped systems in aged state are well developed only in the case of Mn^{3+} -doped system. In Fe^{3+} -doped system, due to the large internal bias, the switching of the spontaneous polarisation is restricted leading to poorly developed P-E and S-E hysteresis loops. Also the SC-SRO mechanism is sluggish leading to poor recoverability of the switched spontaneous

polarisation. But, due to relatively lower internal bias, $[\text{Mn}'_{\text{Ti}} - \text{V}^{\ddot{\text{O}}}]$ defect dipoles are more labile and attain the crystal symmetry on aging and provide restoring force for switched ferroelectric dipoles on removal of applied field.

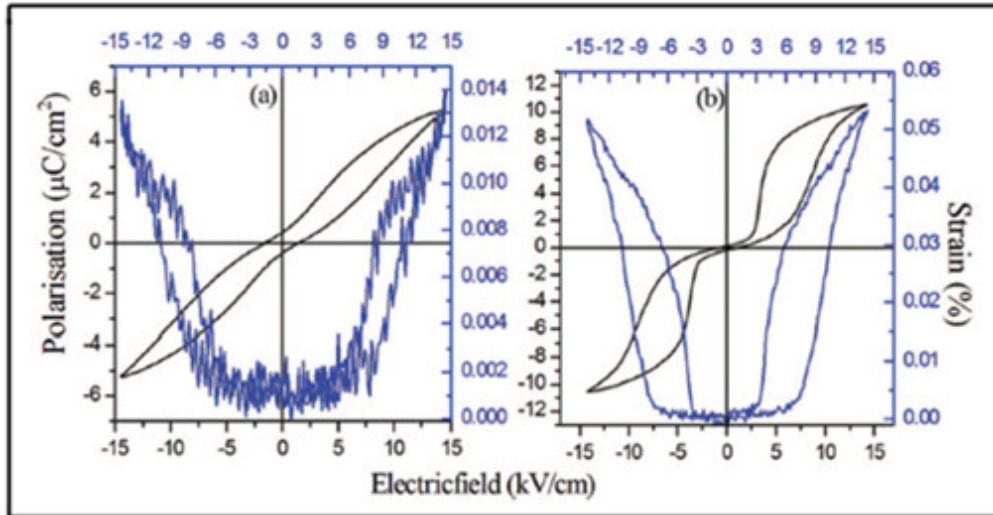


Figure 1.23 P-E and S-E curves of aged samples of (a) Fe^{3+} and (b) Mn^{3+} doped $[(\text{Ba}_{0.80}\text{Sr}_{0.20})\text{TiO}_3]$

[Source: K. Vani et al, *AIP Advances*, 2 (2012) 042177-1-4]

1.1.10.2 Kinetics of migration of oxygen vacancy in perovskite structure

In SC-SRO mechanism the migration of oxygen vacancy ($\text{V}^{\ddot{\text{O}}}$) is diffusion controlled. Therefore, kinetics of migration of oxygen vacancy has a crucial role in controlling ferroelectric aging. Guo et al⁴⁸ studied aging effects in Al^{3+} , Ga^{3+} and Mg^{2+} doped barium titanate. Ferroelectric aging is expected in all the three systems due to the symmetry-conformed thermodynamically stable state. But this study reported remarkable aging effects only in Mg^{2+} and Ga^{3+} -doped compositions and such an effect was not observed in Al^{3+} -doped compositions even with higher aging time compared to other doped systems as shown in Fig. 1.24. This was explained on the basis of lattice volume available for oxygen vacancy ($\text{V}^{\ddot{\text{O}}}$) migration. Ionic radii for various ions for co-

ordination number, CN=6 is $r_{\text{Al}^{3+}} = 0.54\text{\AA}$, $r_{\text{Ga}^{3+}} = 0.62\text{\AA}$, $r_{\text{Mg}^{2+}} = 0.72\text{\AA}$ and $r_{\text{Ti}^{4+}} = 0.61\text{\AA}$. In Al^{3+} -doped compositions, lattice shrinkage was observed due to small size of Al^{3+} ions compared to substituted site Ti^{4+} and therefore migration of oxygen vacancy was retarded. Consequently aging effect is not observed. It is expected that migration of oxygen vacancy will be more easier in an expanded lattice leading to enhanced aging effects in such systems.

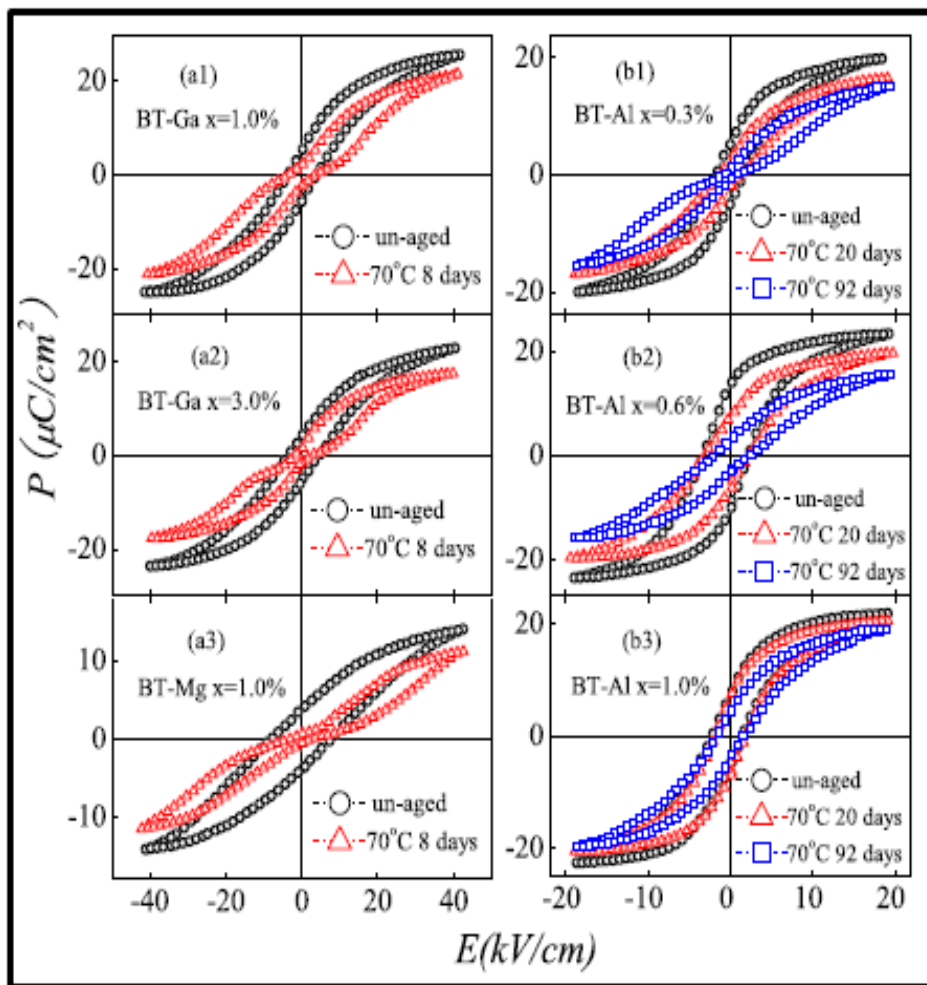


Figure 1.24 P-E hysteresis loops at room temperature for Ga^{3+} , Al^{3+} , Mg^{2+} -doped Barium titanate samples in the unaged and aged states
 [Source: Y. Y. Guo et al, *Appl. Phys. Lett.*, 97(2010)112906-1-3]

1.1.11 Recoverable nonlinear electrostrain by reversible domain switching

The aging effect in ferroelectrics is not always detrimental. It can also be exploited for useful applications. Studies^{42,43,44,49} show that aging effect can be utilized to achieve very large recoverable electrostrain in unpoled and aged acceptor-doped ferroelectrics. In fresh ferroelectrics the electrostrain is related to the domain switching by the external electric field. Consider an aged hard ferroelectric having tetragonal structure (Fig. 1.25). In the aged state, point defect \mathbf{P}_D aligns along the direction of spontaneous polarisation \mathbf{P}_S . When an electric field \mathbf{E} is applied along a direction perpendicular to \mathbf{P}_S , \mathbf{P}_S will switch to the direction of \mathbf{E} by 90° domain switching, but the defect dipole \mathbf{P}_D which is not switched, still keeps the original symmetry. When electric field \mathbf{E} is removed, defect dipoles (\mathbf{P}_D) act as a restoring force that switches domains (\mathbf{P}_S) to the initial state. Such a process generates huge recoverable strain with a maximum theoretically achievable strain of $c/a-1$.

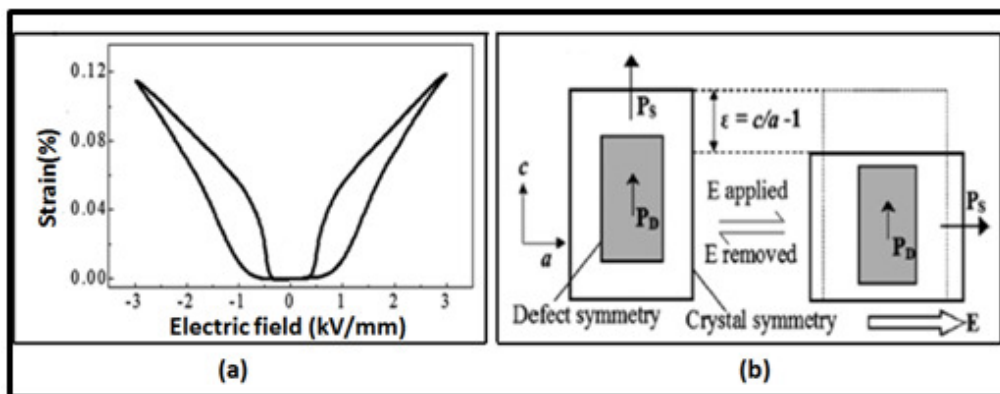


Fig. 1.25 (a) Electrostrain in aged sample of Mn^{3+} -doped BT; (b) Point defect mediated reversible domain switching mechanism in tetragonal ferroelectric unit cell generates large electrostrain.

[Source: L. X. Zhang et al, *Appl. Phys. Lett.*, 85 (2004) 5658-5660]

It is also interesting to note from Fig. 1.26 that with decreasing field frequency [Fig. 1.26(a)] as well as increasing the number of cycles [Fig.

1.26(b)], strain level increases. Also the recoverability of spontaneous polarisation (\mathbf{P}_s) is less under these conditions in aged acceptor-doped ferroelectrics. Decrease in field frequency and increase in number of cycles may assist switching of some of the point defects along field direction⁴⁹. Hence the number of defect dipoles resisting the domain switching becomes less, domain switching becomes easier, consequently the larger strain value results. Since there is a decrease in the number of defect dipoles to reorient the switched ferroelectric domains, recoverability in the strain also becomes weak.

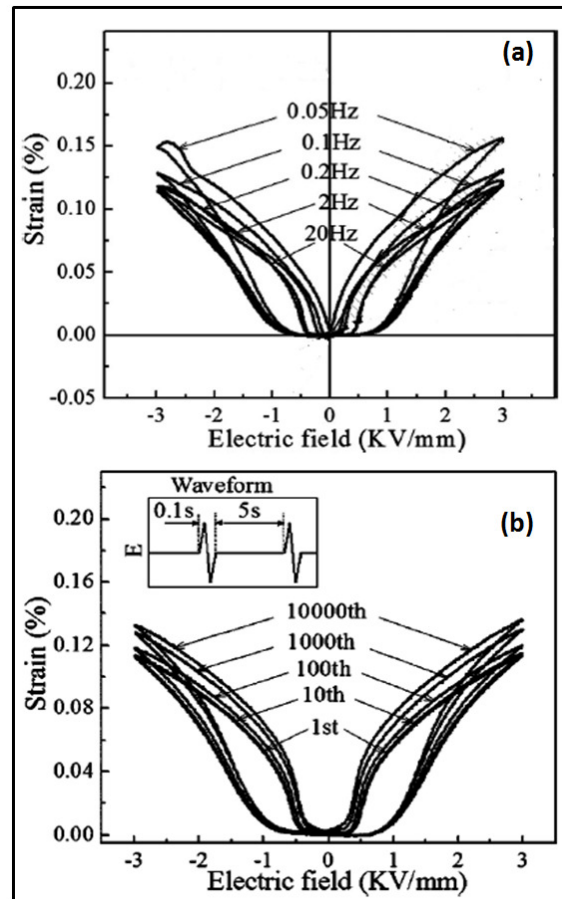


Figure 1.26 (a) Field Dependence of electrostrain of Mn³⁺-doped BST; (b) Cycle dependence of electrostrain of Mn³⁺-doped BST

[Source: L. X. Zhang *et al*, *Appl. Phys. Lett.*, 85 (2004) 5658-5660]

1.2 Introduction to Relaxor ferroelectrics

For many practical applications, ferroelectrics with broad dielectric maximum are desirable. In the family of ferroelectrics, Relaxors are identified for this type of technological applications owing to their broad phase transition from paraelectric state. Relaxors exhibit distinct differences in their electrical and electromechanical characteristics from normal ferroelectrics^{50,51}. They exhibit a very broad and diffuse transition in dielectric permittivity as a function of temperature in contrast to normal ferroelectrics which shows sharp, narrow peak at Curie point, T_c as shown in Fig.1.27. Strong frequency dispersion of the dielectric permittivity observed near T_m , temperature of maximum dielectric permittivity, is associated with a shift to higher temperature with respect to frequency. At temperatures above T_m , they show deviation from Curie-Weiss law as shown in Fig. 1.27.

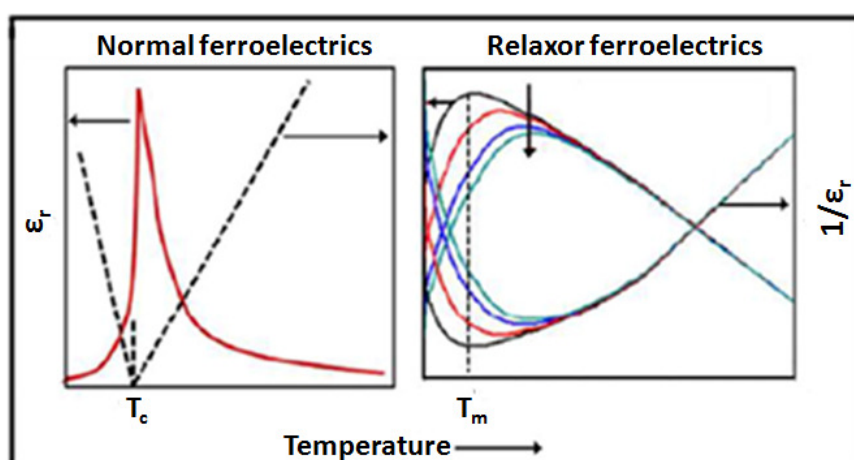


Figure 1.27 Temperature dependence of dielectric permittivity and Curie-Weiss ($1/\epsilon_r$ vs T) plot at $T > T_c$ (T_m)

The saturation and remnant polarisations of normal ferroelectric and relaxor materials with respect to temperature are shown in Fig. 1.28. For ferroelectrics polarisation value decrease with increase in temperature and

suddenly disappear at T_c due to the absence of polarisation above Curie point. Above Curie point ferroelectric undergoes a first order phase transition to non-polarised cubic paraelectric state. In the case of relaxors, polarisation decrease continuously with temperature but do not vanish at T_m .

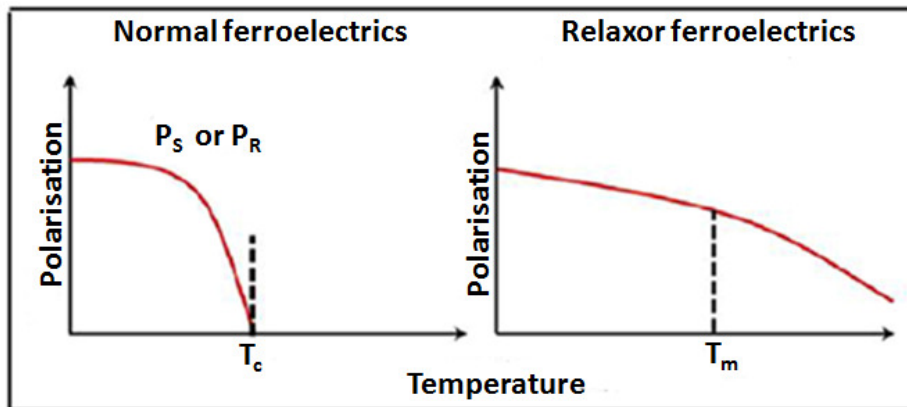


Figure 1.28 Temperature dependence of saturation and remnant polarisations

It is observed from the Fig. 1.29 that a well saturated P-E loop with a large remnant polarisation P_R , is observed for ferroelectric materials while for relaxor materials slim-loop like dielectric hysteresis is observed with unusually small remnant polarisation.

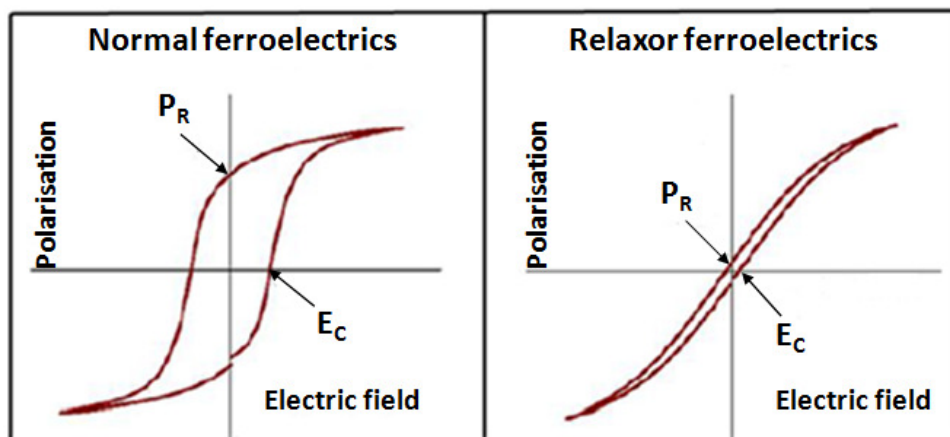


Figure 1.29 P-E hysteresis characteristics normal relaxor ferroelectrics

Differences in these properties of relaxors and ferroelectrics are related to their lattice dynamics which is attributed to nanoscale structural complexity.

1.2.1 Lattice dynamics of relaxor ferroelectrics

Similar to normal ferroelectrics, at high temperatures relaxors exist in a non-polar cubic paraelectric phase. On cooling from high temperature to low temperature through Curie point T_c , normal ferroelectrics are directly transformed to ferroelectric state while relaxors undergo a sequence of temperature-induced transformations. Upon cooling, relaxors are transformed from paraelectric state into an ergodic relaxor (ER) state at the temperature called Burns temperature (T_B). In this state, below T_B , local regions of dipole moments which are oriented in random directions appear within the paraelectric matrix. These polar regions are in nanometer scale and therefore referred to as polar nano regions PNR as shown in Fig. 1.30. At T_B no macroscopic structural change is observed. At temperature close to T_B the formed PNRs are mobile.

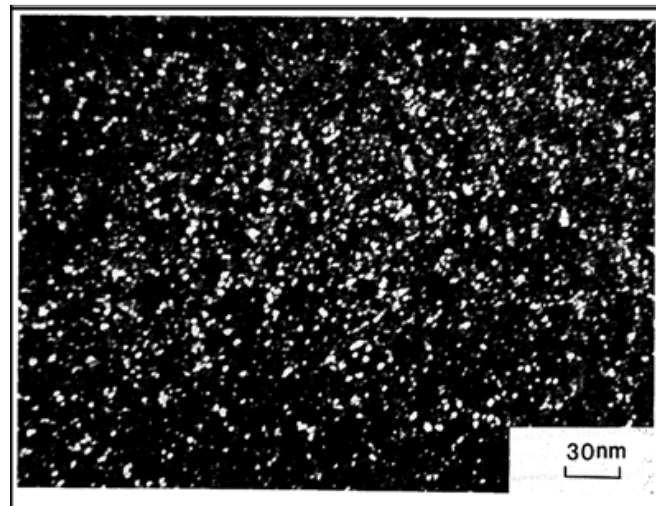


Figure 1.30 Dark field image of ordered domains in nanoscale in PMN

[Source: C. A. Randall et al, *Jpn. J. Appl. Phys.*, 29(1990)327-333]

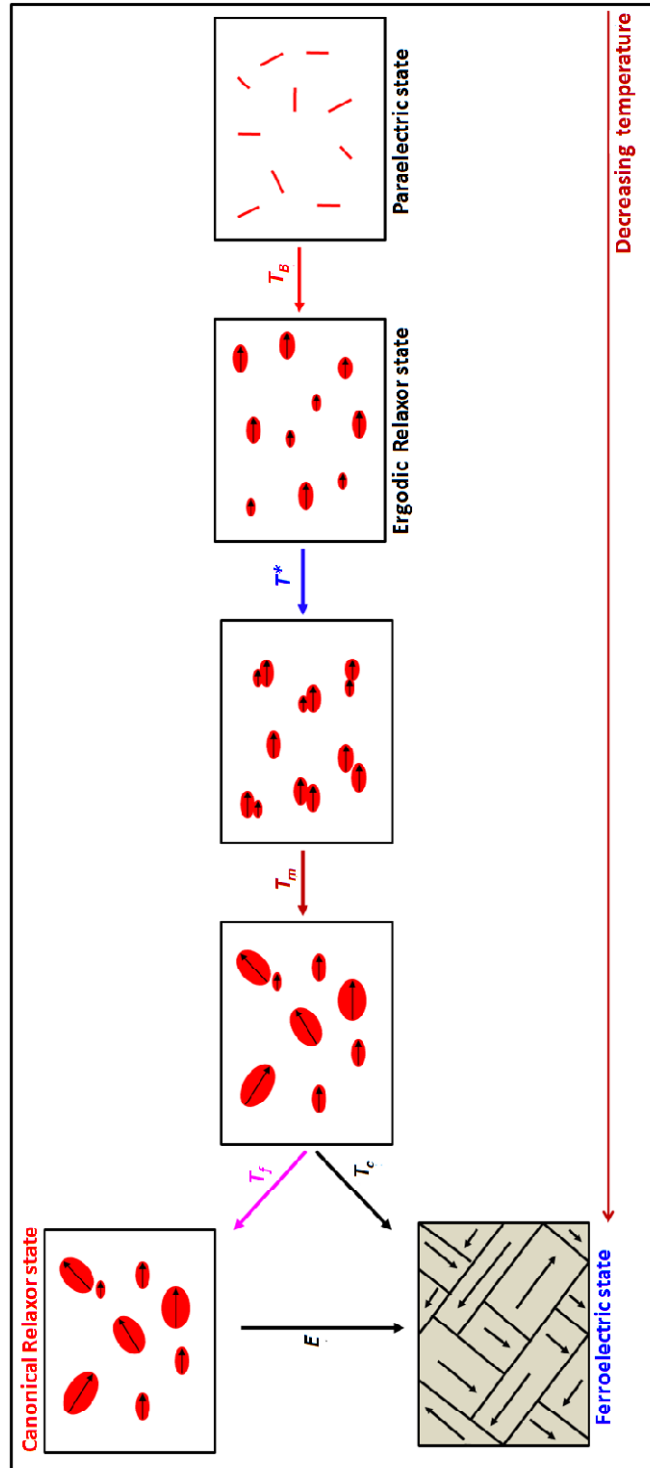


Figure 1.31 Schematic representation of temperature evolution of polar nano regions and macroscopic ferroelectric domains in relaxors

Formed PNRs will polarise the medium within the space region bounded by a correlation radius ' r_c '. On cooling from T_B , at a temperature designated as T^* the correlation radius is expected to increase and this process will continue until a number of PNRs of similar size start to coalesce to form a polarisation cluster. On further cooling, approaching temperature of maximum dielectric permittivity T_m , results in further increase in the size of the PNRs. Further below T_m , relaxors either undergo a phase transition to a normal ferroelectric state (FE) at T_c or transform to a canonical relaxor state at T_f . On cooling to T_f dynamics of PNR slows down and at T_f PNRs freeze into a non-ergodic state (canonical relaxor). Canonical relaxors are irreversibly transformed into a regular long-range ordered ferroelectric state by applying a strong electric field. Schematic representation of temperature evolution of polar nano regions and macroscopic ferroelectric domains in relaxors is given in Fig. 1.31.

1.2.2 Origin of PNR and evolution of relaxor state

It is proposed that the unique properties of relaxors are determined by the polar nanoregions, PNRs present in the system. There are several reports related to origin and the nature of the PNRs. The deviation of the refractive index from the linear behaviour of the paraelectric state below T_B , characterized the formation of polar nano regions⁵². The nature of existence of PNRs, has been demonstrated by different methods likes elastic neutron and X-ray scattering⁵³⁻⁵⁹, Raman spectroscopy⁶⁰⁻⁶³ and nuclear magnetic resonance^{64,65}. It is established that the formation of PNRs is closely associated with chemically-induced disorder and that in their formation and evolution, the nature of cations plays an important role. There are many models suggested to explain the unique nature of dielectric response and polarisation behaviour of relaxor ferroelectrics. According to Smolenskii^{66,67} origin of diffused phase transition is attributed to chemical inhomogeneity on

microscopic level due to compositional fluctuations in the B-site. The difference in concentration of B-site ions in various micro-regions give rise to different local Curie temperatures. The concept of polar micro region was modified by Burns et al^{52,68}. According to them, a local polarisation appears below a certain temperature known as Burns temperature far above T_m indicating that the local symmetry is lower than the global symmetry. The deviation from Curie-Weiss law above T_m also suggests the presence of local polar regions⁵². By analogy with super paramagnetic state, a super paraelectric model was proposed by L. E. Cross⁶⁹. In this model the polar micro regions were considered as independent dipoles which switch between equivalent orientation states according to the symmetry of the local polar state. In the high temperature region the micro polar regions are dynamically disordered. This disordered state is not random, but show some preferential orientation along one of the possible polar directions leading to a net polarisation in a micro region. Viehland et al⁷⁰ proposed a model analogous to spin-glass systems. It was suggested that the transition to a glassy state with randomly oriented frozen dipoles is due to frustrated correlation between superparaelectric moments over a distance of a correlation length ' r_c '. Upon cooling the dynamics of polar regions will slow down leading to freezing of dipoles as in the case of dipoles analogous to spin glasses. Instead of critical slow down, a progressive slowing down with relaxation time is observed on cooling. On cooling, the correlation length increases and dipole moments couple more strongly and at temperature T_f correlation length saturates. Dielectric relaxation is an additional indication of dipole glassy behaviour of relaxor materials. The temperature dependence of relaxation time, τ can be modeled on Vogel-Fulcher relationship as given in equation^{71,72}.

$$\tau = \tau_0 \exp \left[\frac{E_a}{k_B(T-T_f)} \right] \quad (1.8)$$

where τ_0 the pre exponential term is the limiting response frequency, E_a is the activation energy of local polarisation and T_f is the characteristic freezing temperature of the polar nano regions. The Vogel- Fulcher fitting of temperature dependence of relaxation time in a typical relaxor is given in Fig.1.32.

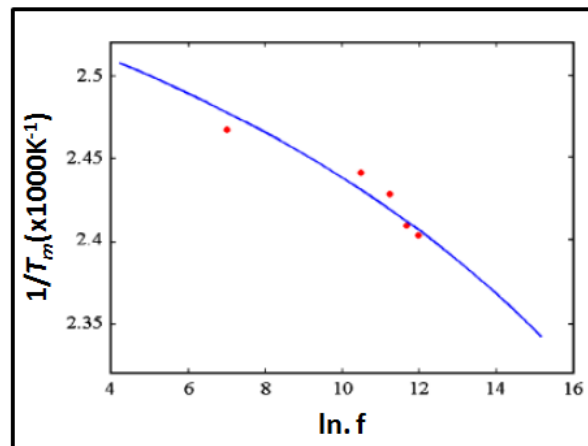


Figure 1.32 Vögel-Fulcher fitting curve of typical relaxor ($\text{Pb}_{0.92}\text{La}_{0.08}$) ($\text{Zr}_{0.65}\text{Ti}_{0.35}$) $\text{Cu}_{0.004}\text{O}_3$. Circles represent experimental data and solid line represents fitting curve

[Source: A. S. Divya et al, *J. Am. Ceram. Soc.*, 92 (2009) 2029-2032]

Another theoretical concept about relaxors was established based on the work of Imry and Ma⁷³ and supported by the quenched random-field model, developed by Westphal, Kleemann and Glinchuk^{74,75}. Random-field-domain stabilized approach is an alternate mechanism to dipolar glassy model. According to this model the relaxor characteristics is attributed to strong contributions of quenched random electric fields arising from charged nano domains and compositional fluctuations.

1.2.3 Relaxors with perovskite structure

Lead-based compositions having complex perovskite structure are relaxors. Complex perovskites of ABO_3 structure incorporates two types of cations which differ in charge and size at A and/or B sites. For e.g. the substitution of two (B' , B'') ions in 1:1 ratio at B-site result in a complex perovskite of general formula $A(B'_{1/2}B''_{1/2})O_3$. Similarly A-site can also be substituted. Thus relaxors can be classified into two main groups.

1.2.3.1 A-site substituted complex perovskite (Pb, A'') BO_3

The substitution of non-isovalent ions at A-site, for eg:- La^{3+} for Pb^{2+} leads to A-site vacancies and gives A-site substituted complex perovskite having the general formula, $(Pb_{1-x}La_x)(Zr_{1-y}Ti_y)O_3$ [PLZT]. Eg:- $(Pb_{1-x}La_x)(Zr_{0.65}Ti_{0.35})O_3$ with $0.04 \leq x \leq 0.12$.

1.2.3.2 B-site substituted complex perovskite, $Pb(B', B'')O_3$

In complex perovskites of the type $Pb(B'_xB''_{1-x})O_3$, two type of cations B' and B'' are located on B-site which differ in both charge and size. eg: PST $Pb(Sc_{1/2}Ta_{1/2})O_3$, PMN $Pb(Mg_{1/3}Nb_{2/3})O_3$, PIN $Pb(In_{1/2}Nb_{1/2})O_3$, PZN $Pb(Zn_{1/3}Nb_{2/3})O_3$ etc. Relaxor behavior observed in such B-site substituted complex perovskites depends on the degree of ordering of the different B-site cations.

For example; (1) In PIN⁷⁶ completely disordered B-site arrangement shows relaxor behaviour with a T_m around 50°C [Fig.1.33(a)] while completely ordered state shows antiferroelectric character having T_c at about 160°C [Fig.1.33(c)]. The partially ordered PIN shows broad dielectric response without dispersion [Fig.1.33 (b)] and a shift in T_c to 100°C.

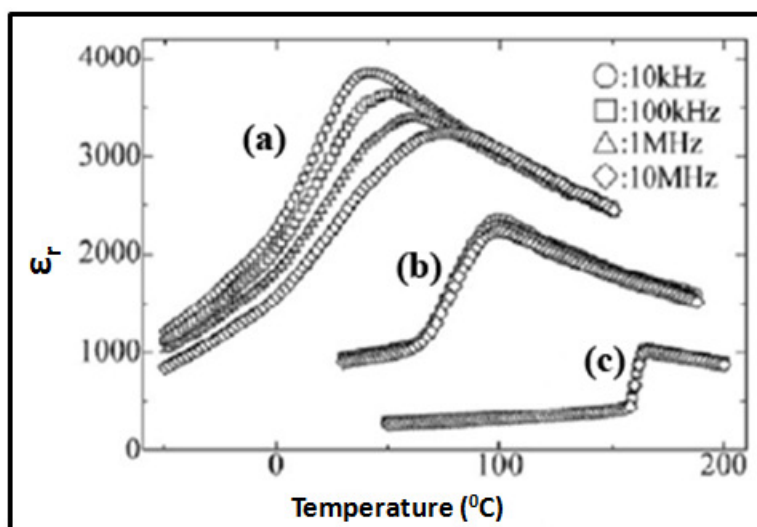


Figure 1.33 Temperature dependence of dielectric constant of (a) disordered (b) partially ordered and (c) ordered PIN

[Source: H. Ohwa et al, *J. Phys. Soc. Jpn.*, 69 (2000) 1533-1545]

(2) In PST^{77} completely disordered B-site arrangement shows relaxor behaviour while ordered state shows antiferroelectric character (Fig. 1.34).

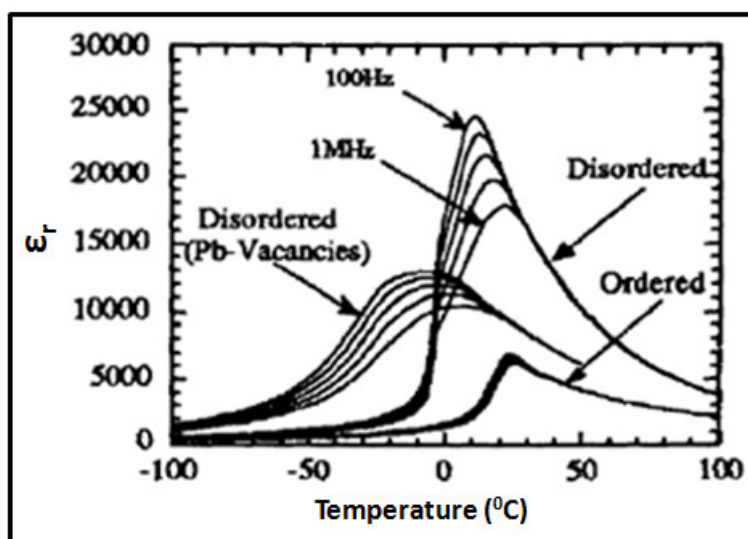


Figure 1.34 Temperature dependence of dielectric constant of disordered and ordered PST

[Source: F. Chu et al, *J. Appl. Phys.*, 74(1993)5129-5134]

1.2.3.3 B-site ordering in $\text{Pb}(\text{B}'\text{B}'')\text{O}_3$ type complex perovskites

In $\text{Pb}(\text{B}'_x\text{B}''_{1-x})\text{O}_3$, B' and B'' ions can be arranged either in an orderly fashion by sharing B sites or in a disordered manner, or between these extremes. B-site cations are said to be ordered when adjacent unit cells on the B-sublattice are unlike and next-adjacent unit cells are similar. The degree of B-site cation order largely depends on the size difference of the B-site ions and on the difference in their valence states. A higher degree of order is expected if there is a larger difference in the sizes of B-cations and their valence states. In B-site ordered compounds, each type of cations should be located in its own sublattice creating a superstructure with complete translational symmetry as shown in Fig. 1.35(a). In B-site disordered compounds, each type of B-cations are distributed in a random fashion as shown in Fig. 1.35(b). Arrows indicates the regions of disordered arrangement.

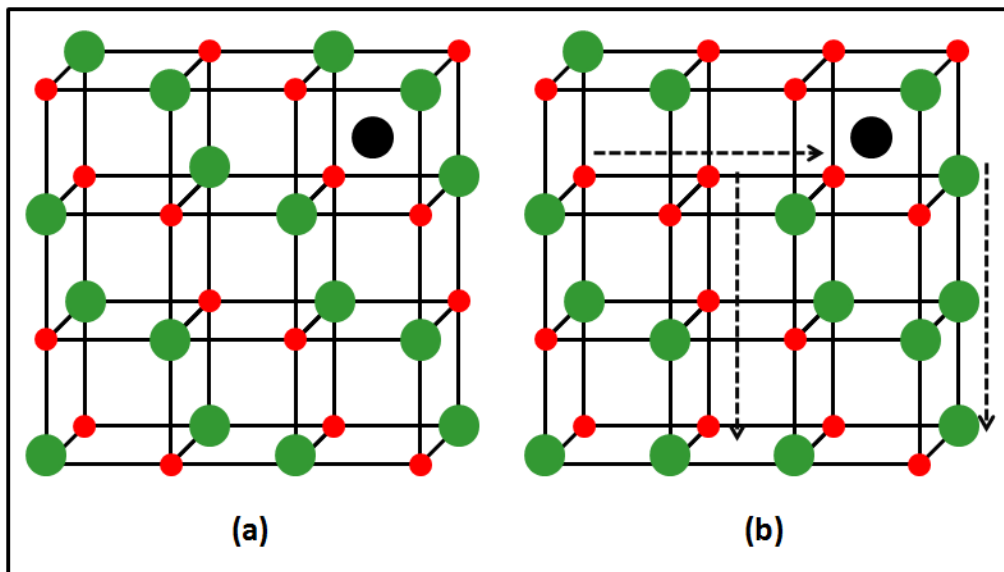


Figure 1.35 Schematic representation of (a) ordered; (b) disordered $\text{Pb}(\text{B}'\text{B}'')\text{O}_3$ perovskite. Black, green and red circles represent Pb, B' and B'' cations respectively. Dashed arrows show the region having disordered arrangement.

1.2.4 Local structural preferences and special bonding considerations in Lead-based complex perovskites

Consider the arrangement of B-cations in two types of B-site substituted complex perovskites of general formula $A(B'_{1/2}B''_{1/2})O_3$ and $A(B'_{1/3}B''_{2/3})O_3$. From stoichiometric consideration, it is noted that complex perovskite of type $A(B'_{1/2}B''_{1/2})O_3$ prefer 1:1 B-site ordering [Fig. 1.36(a)] whereas complex perovskite of type $A(B'_{1/3}B''_{2/3})O_3$ prefer 1:2 B-site ordering [Fig. 1.36(b)].

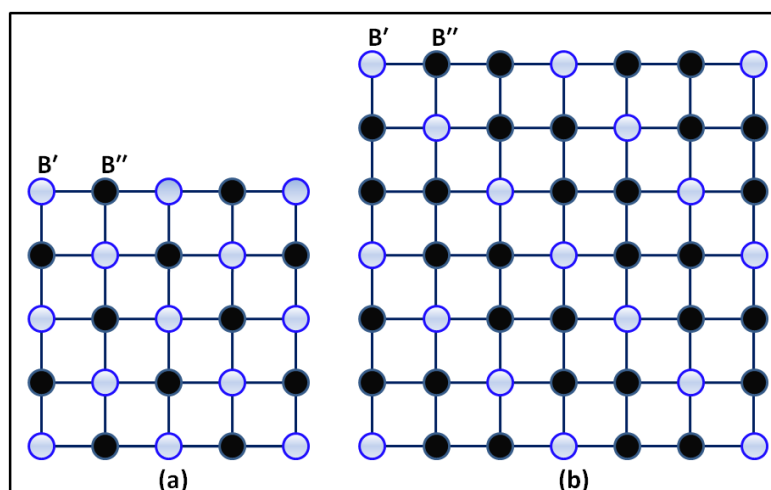


Figure 1.36 B-site ordering in (a) $A(B'_{1/2}B''_{1/2})O_3$ and (b) $A(B'_{1/3}B''_{2/3})O_3$

Interestingly, in Lead-containing complex perovskites like PMN [$Pb(Mg_{1/3}Nb_{2/3})O_3$], having 1:2 stoichiometry at B-sites, regions having 1:1 ordering have been observed along $\langle 111 \rangle$ ^{78,79}. This behaviour in Lead-containing complex perovskites is attributed to special Pb-O-B bonding as a result of the influence of the ns^2 lone pair of electrons of Lead. These Pb-O bonds exist as PbO_3 pyramid capped on oversize B'-cation. This bonding initiates an ordering as Pb-B'-Pb-B'' along $\langle 111 \rangle$ and results in local rhombohedral ($R\bar{3}m$) symmetry as shown in Fig. 1.37.

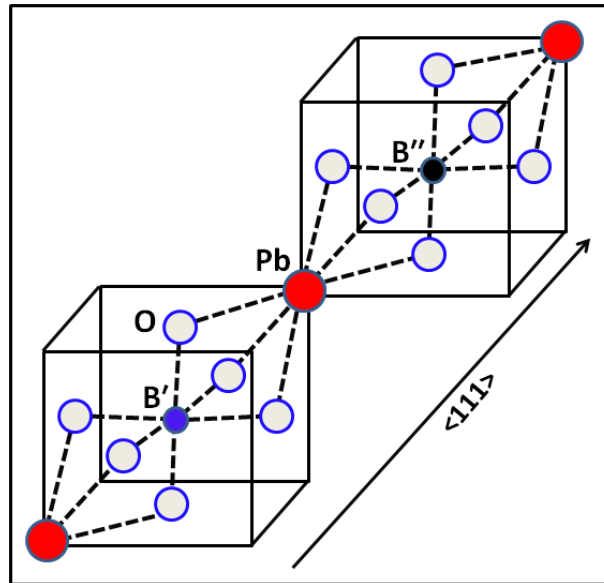


Figure 1.37 Atomic arrangements in $R\bar{3}m$ symmetry for $Pb(B',B'')O_3$ structure

Thus relaxor behavior is observed in many complex perovskites as shown in Table 1.1. When B' cations are larger than the B'' cation, EXAFS study (Table 1.1) has also revealed alterations in B'' -O bond lengths due to the deviation in local atomic structure along $\langle 111 \rangle$.

Table 1.1 EXAFS results of bond distance in several $Pb(B',Nb)O_3$ (Z=Zn, C=Co, N=Ni, I=In; CN stands for coordination number)

Material	Pb-O		B'-O		Nb-O	
	R(Å)	CN	R(Å)	CN	R(Å)	CN
PZN	2.38	2.6	2.03	5.2	1.92	3
					2.12	3
PCN	2.39	2.9	2.08	6.0	1.92	3
					2.13	3
PNN	2.40	2.6	2.06	6.1	1.93	3
					2.13	3
PIN	2.39	2.8	--	--	1.93	3
					2.12	3

It is therefore, of interest, to undertake an in-depth study on the bonding preferences in such complex perovskite systems.

1.3 Introduction to Antiferroelectrics

After PZT, many compositions in the PbZrO_3 - PbTiO_3 - PbSnO_3 ternary phase diagram were developed for transducer applications. Many compositions in this ternary phase diagram are antiferroelectrics as shown in Fig.1.38.

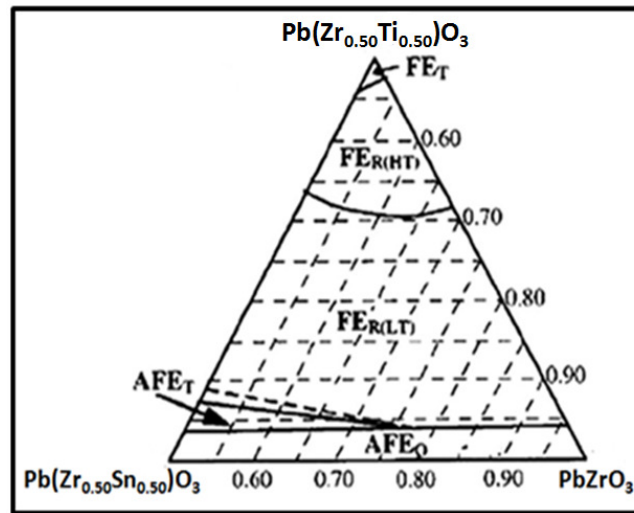


Figure 1.38 Ternary phase diagram for PbZrO_3 - PbTiO_3 - PbSnO_3 system

[Source: W.Y. Pan et al, *J. Am. Ceram. Soc.*, 72(1989)571-578]

Antiferroelectric (AFE) state in materials was first defined by Kittel in 1951⁸². AFE materials are those that have spontaneous polarisation with adjacent dipoles being opposite. On cooling from high temperature undergoes phase transformation from cubic paraelectric (PE_C) state to centrosymmetric AFE state. Polarisation-electric field response of AFE materials gives a linear response as shown in Fig.1.39.

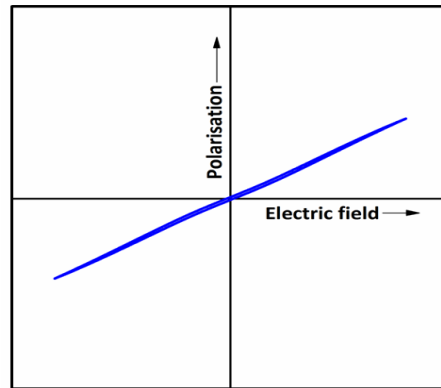


Figure 1.39 Polarisation-Electric field characteristics for antiferroelectric phase

1.3.1 Lead Zirconate

Lead zirconate is a classical example for perovskite antiferroelectric and has been widely studied. Lead zirconate has orthorhombic structure at room temperature. AFE effect in Lead zirconate originates from the antiparallel shift of Pb^{2+} ions about 0.2\AA in the a-b plane along $\langle 110 \rangle$ of orthorhombic cell⁸³⁻⁸⁵ as shown in Fig. 1.40.

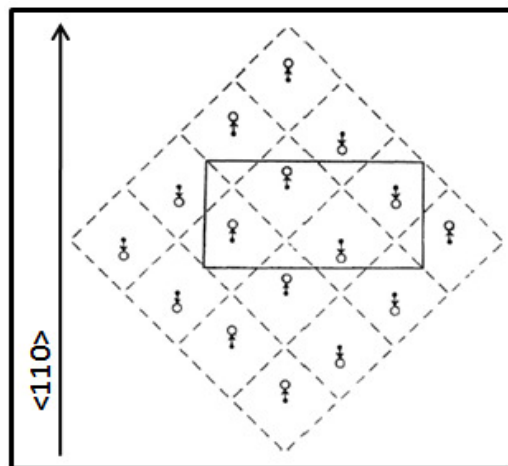


Figure 1.40 Antiferroelectric structure of Lead zirconate. Arrows represent the direction of shifts of Pb^{2+} ions; solid line shows an orthorhombic unit cell; dashed lines show the unit cells of the high temperature cubic phase.

[Source: E. Sawaguchi et al, *Phys. Rev.* 83 (1951) 1078]

1.3.2 Importance of AFE materials

In spite of absence of net spontaneous polarisation and piezoelectricity, antiferroelectric materials attract researchers' attention due to their unique electric field driven AFE - FE phase transition accompanied by a volume expansion. Due to the phase switching process, many studies have been carried out on AFEs over the past several years for industrial applications such as storage capacitors with high energy density and energy conversion devices⁸⁶⁻⁸⁸. Understanding the mechanistic aspects of phase transitions in AFE materials is important since the phase transitions are related to the tuning of electrical characteristics for practical applications.

1.3.2.1 Crystal structure change during AFE-FE phase transformation

AFE-FE phase transformation is accompanied crystal structure change which is the basis of the practical applications of AFE materials. An AFE form has a lesser lattice volume compared to the cubic paraelectric state while ferroelectric form has greater volume than paraelectric state. So the transition from AFE phase to FE phase will bring a large volume change and therefore field induced AFE-FE phase transformation will induce large strain and dielectric polarisation in the lattice. Consider phase transition from tetragonal or orthorhombic AFE to rhombohedral FE phase. Fig.1.41 shows the AFE and FE axes in the unit cell. The unit cell volume of FE state is higher than that of AFE states. Therefore during the AFE-FE phase transformation occurs, volume expansion occurs leading to high field-induced strain.

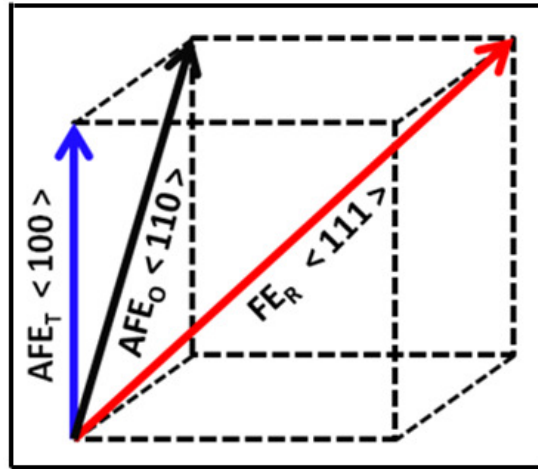


Figure 1.41 Schematic diagram of the primitive cell in AFE and FE states

1.3.2.2 Polarisation and Strain behaviour during AFE-FE phase transformation

Fig. 1.42 represents polarisation versus electric field characteristics for field forced antiferroelectric to ferroelectric phase transition. As the electric field is increased from zero to a value E_F , AFE material shows a linear response like a dielectric material. When the electric field is further increased over E_F , the polarisation response become nonlinear and adjacent dipoles which are aligned in opposite direction start to align in parallel direction and ferroelectric state is induced. Once all the dipoles are aligned in the same direction, polarisation response becomes linear giving maximum value P_F . When the field strength starts to decrease to the point E_A dipoles are realigned and revert back to AFE state. E_F and E_A are known as critical forward phase field and critical backward phase field respectively. Typical strain-electric field curve for field forced AFE-FE transformation is given Fig.1.43. When the electric field is above E_F , AFE phase transforms to FE phase with an expansion in crystal volume, resulted high strain.

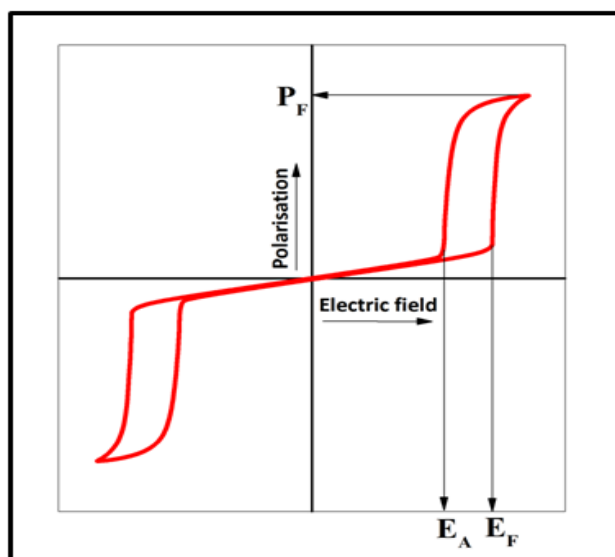


Figure 1.42 Polarisation-Electric field characteristics for field forced antiferroelectric to ferroelectric phase transition

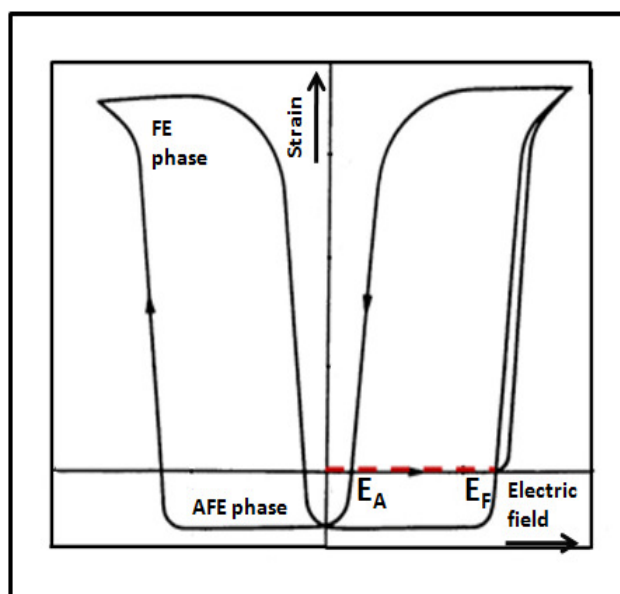


Figure 1.43 Polarisation-Electric field characteristics for field forced antiferroelectric to ferroelectric phase transition

1.3.2.3 Phase switching induced currents

Large increment in current is observed at AFE-FE phase transformation. Typical current-electric field curve is shown in the Fig.1.44.

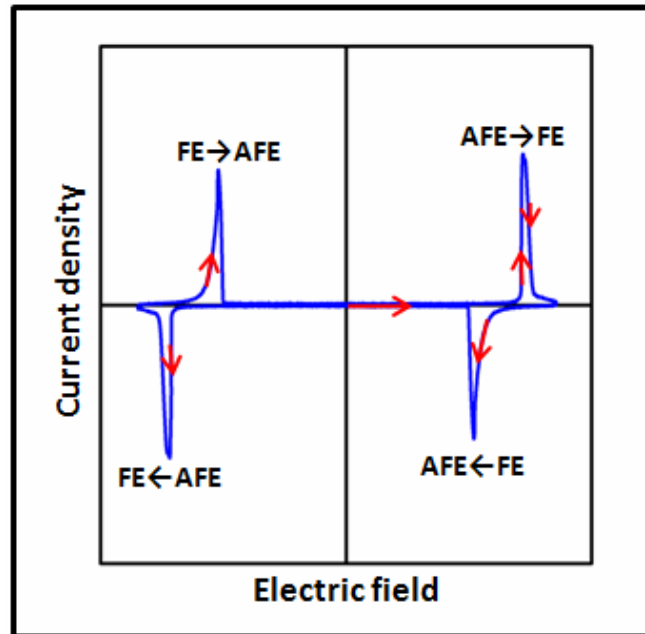


Figure 1.44 Current- Electric field curves of AFEs during AFE-FE phase transformation

During the AFE-FE transformation, when the applied electric field reaches critical value for transformation, all adjacent dipoles are aligned in the same direction and FE state is induced. There is abnormal increase in the polarisation value due to the turning of dipoles leading to instantaneous large current. When the electric field is decreased below the critical level, AFE state is recovered and corresponding peak appears in current-electric field curve. So four peaks appears in the curve.

1.3.3 AFE-FE phase switching sequence

Park et al⁸⁹ proposed AFE-FE phase transformation procedure into six steps as given in Fig.1.45.

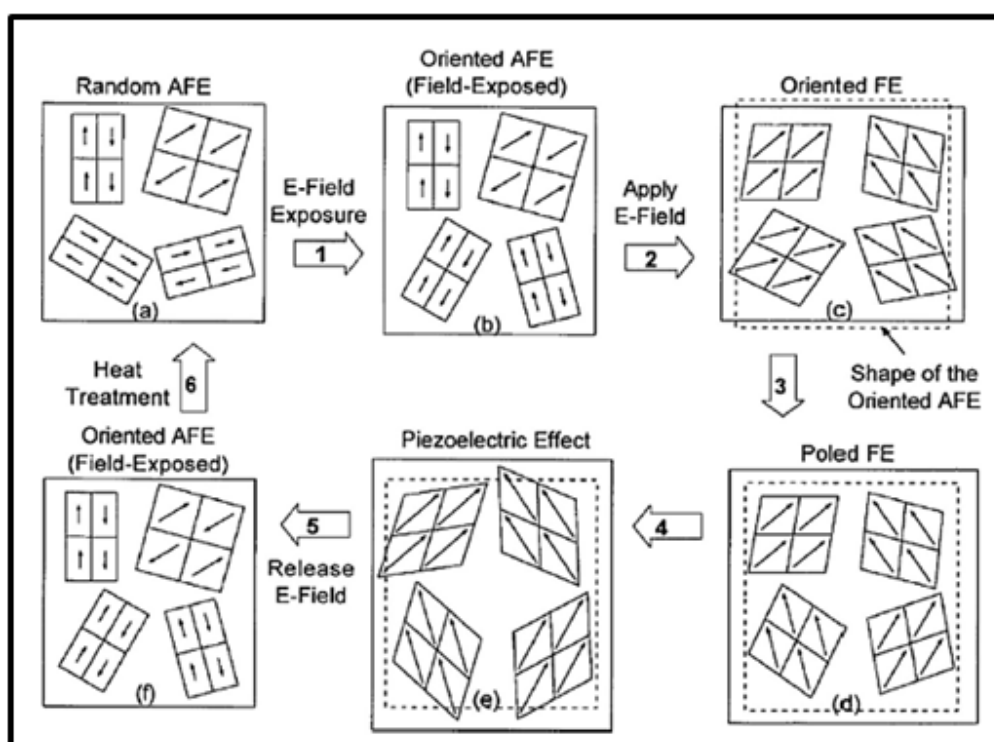


Figure 1.45 Schematic diagram of AFE-FE phase switching procedure

[Source: S. E. Park et al, *J. Appl. Phys.*, 82(1997) 1798-1803]

At first step, at a lower electric-field exposure randomly oriented AFE domains in the material are aligned in preferential direction. At second step, when we are increasing electric field, at the critical forward phase field, preferentially oriented AFE domains undergo transformation into FE state and tend to align their polarisation direction along electric field direction in order to minimize the free energy. At third step, with further increasing electric field, polarisation direction of the induced FE domains is reoriented and polarisation continues to rise. At fourth step, at the higher electric field piezoelectric effect in the induced FE state appears. At fifth step, upon the removal of electric field, realignment of FE domains occurs and induced FE states slip back to oriented AFE states. At sixth step, oriented AFE state

returned to random AFE state after heating above its AFE- paraelectric transition, Curie point.

1.3.4 Stability of phases in AFEs

From thermodynamic considerations, the stability is dictated by the phase having the lowest free energy, G . Phase switching in AFE materials is attributed to smaller free energy difference between the AFE and FE phases^{90,91}. Fig. 1.46 demonstrates the free energy difference, ΔG as a function of temperature for FE and AFE states.

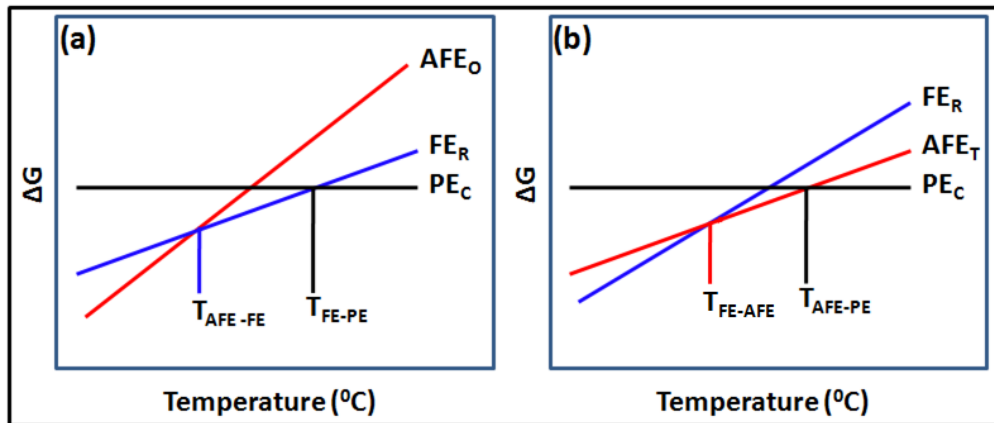


Figure 1.46 Sequence of phase transitions as a function of temperature for (a) AFE_O and (b) AFE_T phases

Two types of AFE phases are present; orthorhombic AFE (AFE_O) and tetragonal AFE (AFE_T). With increasing temperature, phase switching of these two AFE phases are different⁹² [Fig. 1.46(a) and (b)]. For orthorhombic AFEs [Fig. 1.46(a)], the free energy of AFE_O phase is smallest, compared to FE and PE phases at low temperatures. So at low temperature AFE_O phase is stable. Above the temperature $T_{\text{AFE-FE}}$, which is the phase transformation temperature from AFE_O to FE_R , the free energy of FE phase is least as compared to AFE and PE phases; as a result the FE phase is stable. As the temperature is further increased, the free energy of PE phase shows the smallest value at $T \geq T_{\text{FE-PE}}$ as

compared to AFE and FE phases, thus the material stays in PE_C state. The temperature T_{FE-PE} is Curie point. As shown in Fig. 1.46(b), the temperature-dependent phase transition process of tetragonal AFEs is different. At low temperatures FE phase is stable because of its smallest free energy. During the temperature range from T_{FE-AFE} to T_{AFE-PE} , the free energy of AFE phase is the least one, so the material exists in AFE state. T_{FE-AFE} represents the phase transition temperature from FE to AFE and T_{AFE-PE} represents Curie point.

1.3.5 Stability of ferroelectric phase in antiferroelectric Lead zirconate

Temperature dependent dielectric constant of Lead zirconate is shown in Fig.1.47.

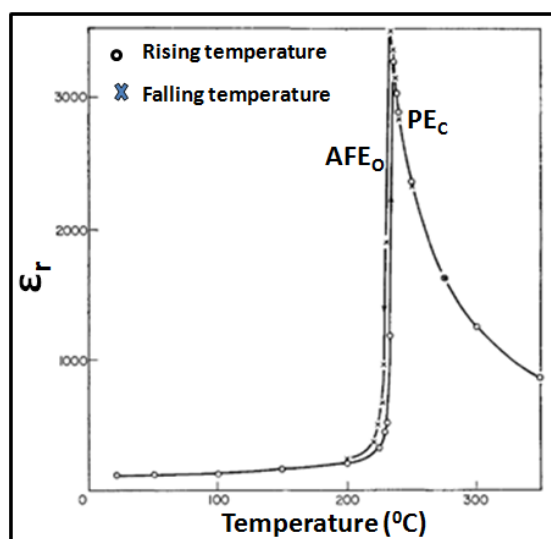


Figure 1.47 Dielectric constant versus temperature curve for $PbZrO_3$

[Source: S. Roberts, *J Am. Ceram. Soc.*, 33(1949)63-66]

From the curve, it is clear that Lead zirconate undergoes a phase transition from PE cubic (PE_C) state to orthorhombic AFE (AFE_0) state at the Curie point, $230^\circ C^{93,94}$. Interestingly, in between orthorhombic AFE_0 and PE_C phases an intermediate FE state has been reported in a narrow temperature

region⁹⁵⁻⁹⁷. This stable intermediate FE phase has rhombohedral symmetry (FE_R)⁹⁸⁻¹⁰⁰ and is observed in both polycrystalline and single crystal of Lead zirconate 10⁰C below Curie point¹⁰¹. The existence of a stable FE phase makes it possible for field enforced AFE→FE phase transition near the Curie point giving double hysteresis loop. At room temperature this phase transformation was not observed since the critical field for the transition was higher than breakdown field. In order to reduce the critical field, $PbZrO_3$ was modified by chemical substitution using various ions at A- and B-sites. Two intermediate phases, existing between AFE_O and PE_C , have also been reported, one rhombohedral FE and other tetragonal AFE (AFE_T) phases. There are several additives to $PbZrO_3$ in small amounts which stabilize either FE_R or AFE_T below Curie point between AFE_O and PE_C . Most widely used additives are Ba^{2+} , Sr^{2+} and La^{3+} at A-site and Sn^{4+} , Ti^{4+} and Nb^{5+} at B-site. As the AFE stability in Lead zirconate is maintained by the Pb^{2+} ions, it is of interest to substitute lead ions either by isovalent ions like Ba^{2+} , Sr^{2+} or aliovalent ions like La^{3+} . The ionic radius of substituent ions is a key factor for deciding the phase stability in the case of A-site substitution. For example, doping with Ba^{2+} (higher ionic radius) at Pb^{2+} site will stabilize the FE_R phase between AFE_O and PE_C phases and temperature window of FE state also has been reported to be expanded as shown in Fig. 1.48(a). Substitution with Sr^{2+} (lower ionic radius) favour the AFE phase stabilization as shown in Fig. 1.48(b) and introduce tetragonal AFE phase between orthorhombic AFE and cubic PE states^{102,103}.

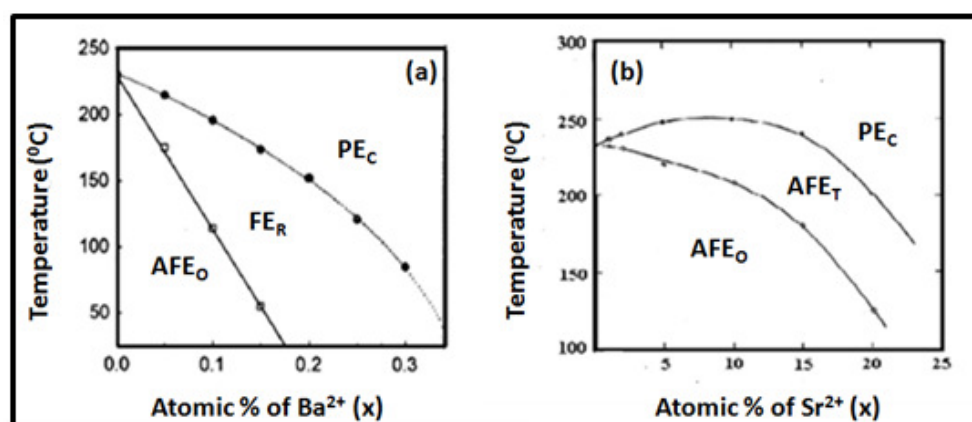


Figure 1.48 Phase diagram of (a) $(\text{Pb}_{1-x}\text{Ba}_x)\text{ZrO}_3$ (b) $(\text{Pb}_{1-x}\text{Sr}_x)\text{ZrO}_3$

[Source: G Shirane, *Phys. Rev.*, 86 (1952) 219-227]

Substitution of La^{3+} in Lead zirconate has a dual effect. On one hand substitution of La^{3+} disturbs Pb^{2+} -order by creating lead vacancies thus destabilizing the antiferroelectric phase. But on the other hand, since ionic radius of La^{3+} is smaller than that of Pb^{2+} , it leads to tilting of the oxygen octahedron leading to the stabilization of the antiferroelectric phase¹⁰⁴⁻¹⁰⁶. Both FE and AFE phases in Lead zirconate are sensitive to application of external field like hydrostatic pressure, DC bias etc. Application of hydrostatic pressure has been reported to enhance the short range AFE interactions in Lead zirconate¹⁰⁷⁻¹⁰⁹. With increasing DC bias, temperature window of stability of FE phase is reported to be enhanced. This observation reveals that application of DC field leads to stabilization of FE phase by field-forced long range ordering^{110,111}.

FE phase in Lead zirconate can also be induced by certain B-site substituents. On addition of small concentrations of Ti^{4+} ¹¹² and Nb^{5+91} at Zr^{4+} -site an intermediate ferroelectric phase is observed [Figs. 1.49 & 1.50] while addition of Sn^{4+} induces tetragonal AFE phase¹¹³.

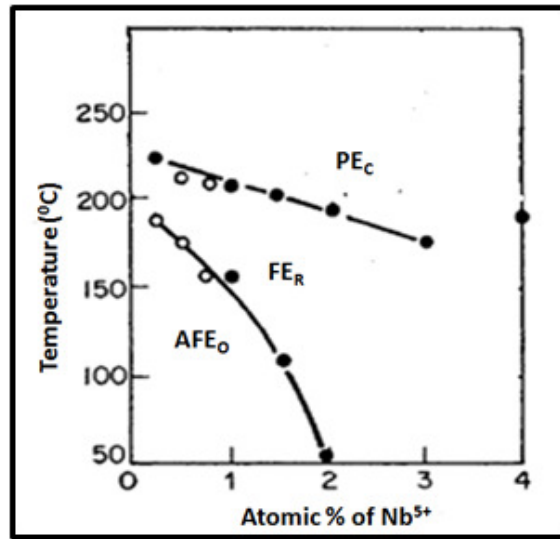


Figure 1.49 Phase diagram of PbZrO₃ with admixtures of Nb⁵⁺

Substitution of Ti⁴⁺ for Zr⁴⁺ in antiferroelectric Lead Zirconate lead to most investigated PZT solid solution systems. Substitution of about 3 at% Ti⁴⁺ brings about a ferroelectric phase in a narrow temperature range. By an addition of 7 at% Ti⁴⁺ the FE phase exists from room temperature to the Curie point. The room temperature morphotropic phase boundary for AFE_O and FE_R exist at Zr/Ti ratio of 95/5.

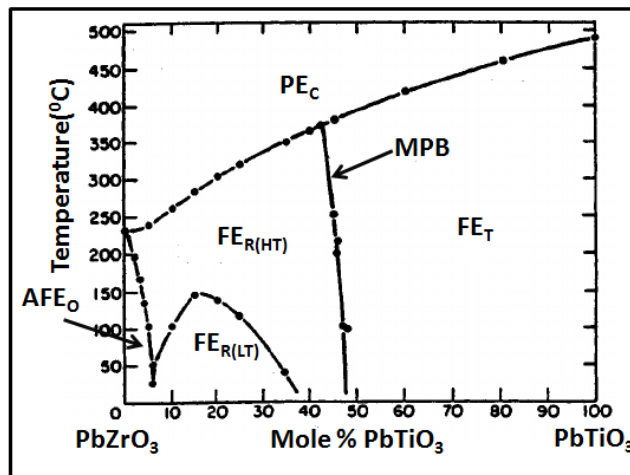


Figure 1.50 PbZrO₃- PbTiO₃ phase diagram

1.3.6 Ferroelectric and antiferroelectric Sn-modified Lead Zirconate Titanate

Ternary phase diagram for PbZrO_3 - PbTiO_3 - PbSnO_3 is given Fig.1.51. AFE_O state is stabilized at compositions near the high Zr-content region and FE_T phase is stabilized in high Ti-content region.

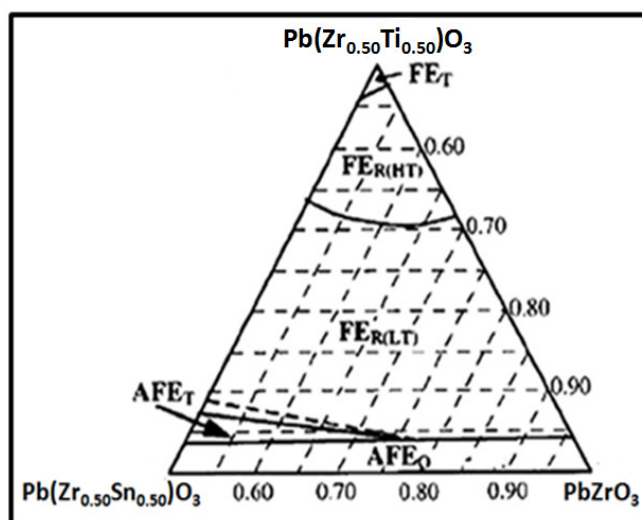


Figure 1.51 Ternary phase diagram for PbZrO_3 - PbTiO_3 - PbSnO_3 system

[Source: W.Y. Pan et al, *J. Am. Ceram. Soc.*, 72(1989)571-578]

In this ternary phase diagram, various phases can be seen to exist including antiferroelectric orthorhombic (AFE_O), antiferroelectric tetragonal (AFE_T), high temperature ferroelectric rhombohedral ($\text{FE}_{R(\text{HT})}$) and low temperature ferroelectric rhombohedral ($\text{FE}_{R(\text{LT})}$). Addition of Sn^{4+} into the PZT solid solution lowers the distortion of ferroelectric rhombohedral phase and reduces the volume difference between the ferroelectric and antiferroelectric phases¹⁰⁷. Hence free energy difference between the phases is nearly small and FE-AFE transformation is easier. The relative phase stabilities in this solid solution strongly depend on the compositional

variations. The compositions near high Zr^{4+} content hold strong scientific interest due to the presence of both ferroelectric and antiferroelectric phases.

However, many material systems in the $PbZrO_3$ - $PbTiO_3$ - $PbSnO_3$ ternary systems have also evinced considerable interest with respect to the sequence of the phase transformations below Curie point. Berlincourt et al¹⁰⁷ reported complex phase transformation sequence for the compositions in this ternary system with heating and cooling treatments. Interestingly, the sequence of phase transformations is different with heating and cooling treatments. Temperature-composition phase diagram for $Pb_{0.98}Nb_{0.02}[(Zr_{0.90}Sn_{0.10})_{1-y}Ti_y]_{0.98}O_3$ is shown in Fig. 1.52. When $y=0.03$, phase transitions follow the order $AFE_O \rightarrow AFE_T \rightarrow FE_R \rightarrow PE_C$ during the heating cycle [Fig.1.52 (a)] while AFE_T does not appear during cooling [Fig.1.52 (b)] and the sequence on cooling is $AFE_O \leftarrow FE_R \leftarrow PE_C$.

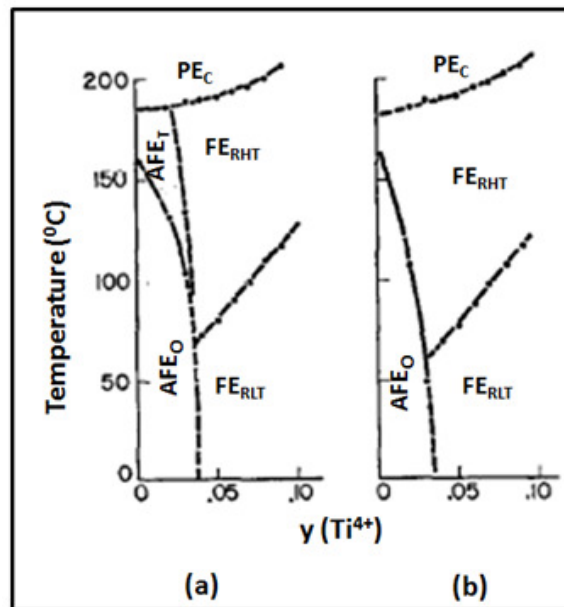


Figure 1.52 Temperature-composition phase diagram for $Pb_{0.98}Nb_{0.02}[(Zr_{0.90}Sn_{0.10})_{1-y}Ti_y]_{0.98}O_3$ with y variable, (a) for increasing temperature and (b) for decreasing temperature.

[Source: D. Berlincourt et al, *J. Phys. Chem. Solids*, 25 (1964) 659-674]

Apart from the different effect seen in the sequence of phase transformations, in certain Sn-modified lead zirconate titanate compositions phase transition from paraelectric phase into AFE state is seen to proceed through an additional intermediate phase known as multi cell cubic (MCC) state as shown in Fig. 1.53(a) and (b) where the MCC state is interposed between PE_C and AFE_T phases.

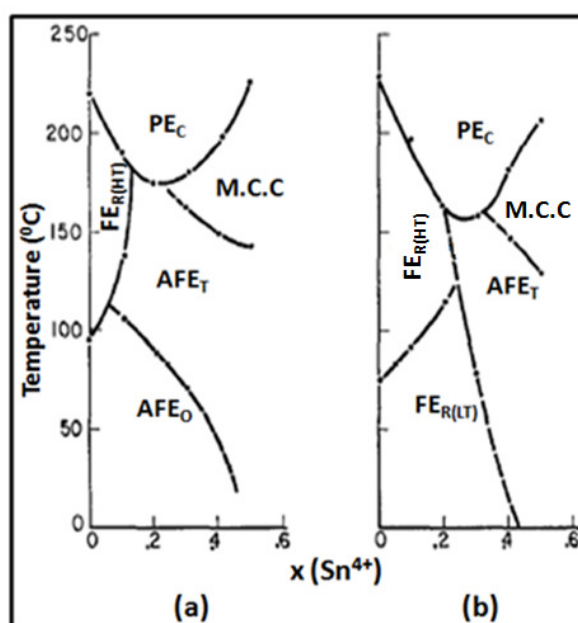


Figure 1.53 Temperature-composition phase diagram for $Pb_{0.98}Nb_{0.02}[(Zr_{1-x}Sn_x)_{1-y}Ti]_{0.98}O_3$ with 'x' variable, $y = (a)0.03$ and $(b)0.06$.

[Source: D. Berlincourt et al, *J. Phys. Chem. Solids*, 25 (1964) 659-674]

Typical dielectric curves of compositions where intermediate MCC state appears is shown in Fig. 1.54. It is observed that the presence of MCC state effectively eliminates the sharp dielectric constant peak that would otherwise occur at $FE \leftarrow PE_C$ or $AFE \leftarrow PE_C$ transformations. Maximum dielectric constant is found near the temperature of the formation of multicell cubic state. The volume relationship between the cubic paraelectric phase and FE/AFE phase remains unchanged even after the formation of intermediate MCC state.

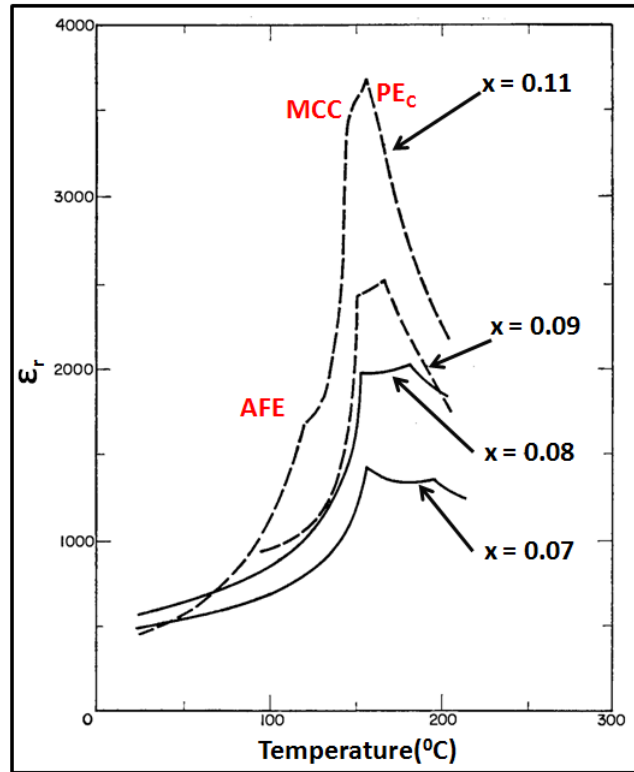


Figure 1.54 Temperature dependent dielectric response in compositional series of formula $\text{Pb}_{0.995}\text{Nb}_{0.01}[(\text{Zr}_{0.60}\text{Sn}_{0.40})_{1-x}\text{Ti}_x]_{0.99}\text{O}_3$

[Source: B. Jaffe et al, *Piezoelectric Ceramics*, 1971].

Temperature dependent free energy of MCC state is shown in Fig. 1.55. At temperatures, $T < T_{MCC-PE}$, MCC state has low free energy compared to that of paraelectric cubic state. In temperature region where MCC state was stable broadening of the dielectric response resulted as shown in Fig. 1.54.

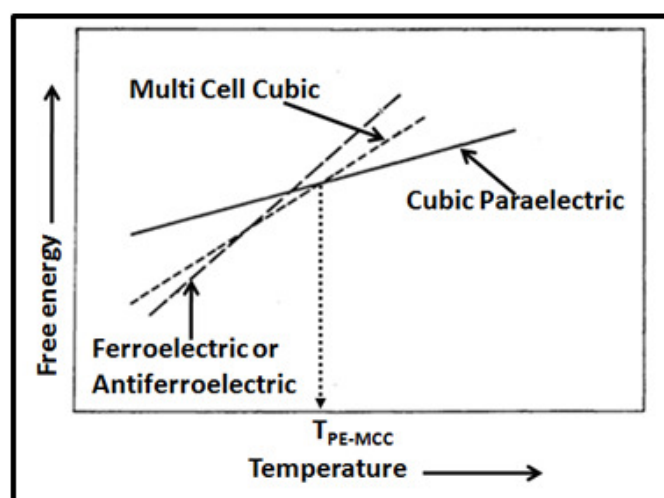


Figure 1.55 Free energies of Cubic Paraelectric (PE_c), Multi Cell Cubic (MCC) and Ferroelectric (FE)/ Antiferroelectric (AFE) phases.
 [Source: B. Jaffe et al, *Piezoelectric Ceramics*, 1971]

1.3.7 Incommensuration in Sn-modified Lead Zirconate Titanate

Selected area electron diffraction (SAED) technique in transmission electron microscopy observed incommensurate modulations in some of the Sn-modified lead zirconate systems below Curie point¹¹⁴⁻¹¹⁹. For example, in the composition $Pb_{0.98}Nb_{0.02}[(Zr_{0.58}Sn_{0.42})_{0.96}Ti_{0.04}]_{0.98}O_3$, such incommensurate modulations are characterized by $(1/x)$ $[110]$ super lattice reflections where 'x' is the super lattice period¹¹⁶. The modulation wavelength (λ) can be calculated by the separation of superlattice spots from relevant main reflections. Since the super lattice period 'x' is not an integer value, there is no relation between lattice parameter and modulation wavelength and modulation wavelength is incommensurate with the periodicity of lattice. A representative $[001]$ SAED pattern of incommensurate modulations is shown in the Fig. 1.56. In these temperature dependent SAED patterns superlattice spots (arrowed) are observed between $[110]$ reflections.

Chemical modifications and temperature have prominent effects on incommensurate modulations. However in certain range of temperature where modulation remains incommensurate with lattice, modulation wavelength was found to be relatively independent of temperature as shown in Fig. 1.57(a). This indicates that the phase with the incommensurate modulations becomes metastably locked-in. The metastability of incommensurate modulations manifest as plateau region in the dielectric response as shown Fig. 1.57(b).

Metastability of incommensurate modulations can be modified by changing Sn/Ti ratio, application of DC bias, etc:-¹¹⁶.

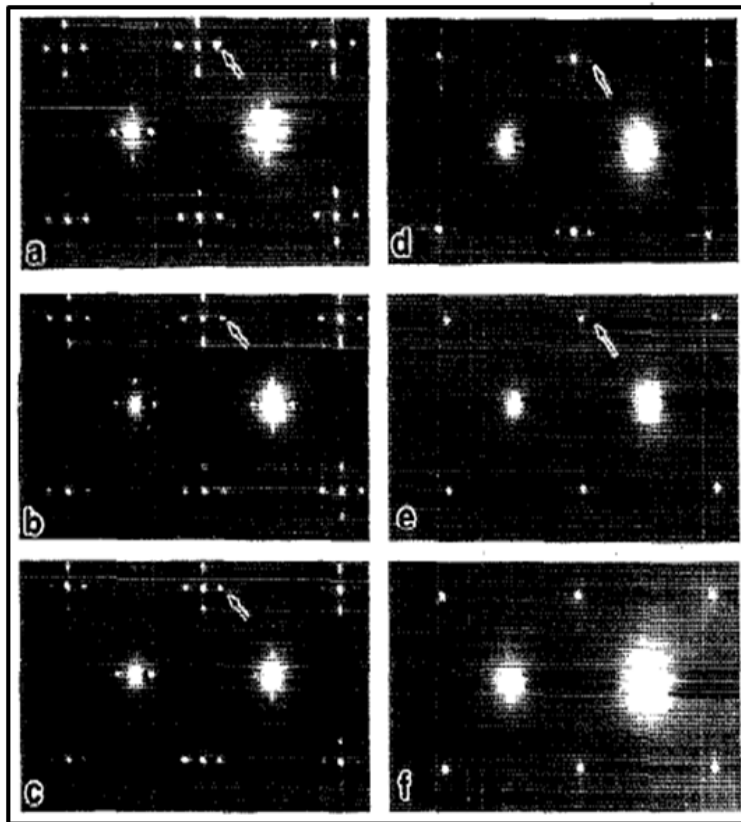


Figure 1.56 [001] SAED patterns for $\text{Pb}_{0.98}\text{Nb}_{0.02}[(\text{Zr}_{0.58}\text{Sn}_{0.42})_{0.96}\text{Ti}_{0.04}]_{0.98}\text{O}_3$, at temperature a) 25°C, b) 75°C, c) 100°C, d) 140°C, e) 155°C and (f) 165°C.

[Source: D. Viehland et al, *J. Appl. Phys.*, 75 (1994) 4137-4143]

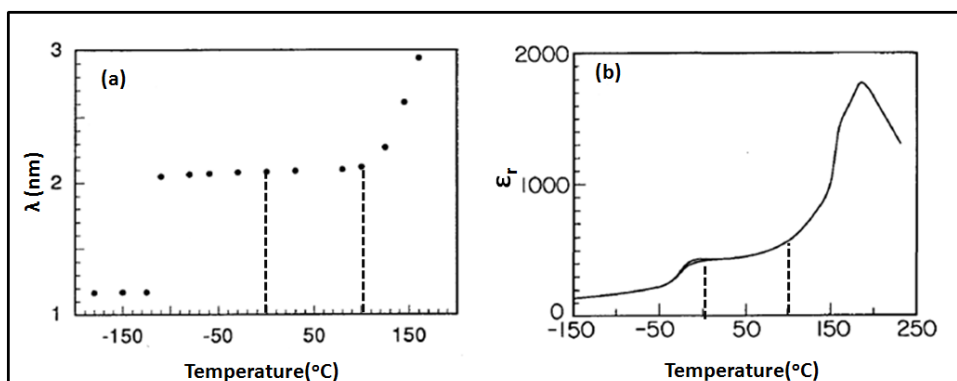


Figure 1.57 (a) Modulation wavelength (λ) of incommensurate structure and (b) dielectric response as a function of temperature

[Source: Z. Xu et al, *J. Mater. Res.*, 10 (1995) 453-460]

1.3.7.1 Compositional effects (Sn/Ti ratio) on incommensuration

In Fig. 1.58 influence of Sn-content (x) on the dielectric response of $\text{Pb}_{0.98}\text{Nb}_{0.02}[(\text{Zr}_{1-x}\text{Sn}_x)_{0.94}\text{Ti}_{0.06}]_{0.98}\text{O}_3$ at a fixed Ti-content is presented. From Fig. 1.58 it is observed that increasing Sn-content, there is a strong suppression of the dielectric constant and broadening of the dielectric maximum. The broadened MCC region depicts improved stability of incommensurate structures.

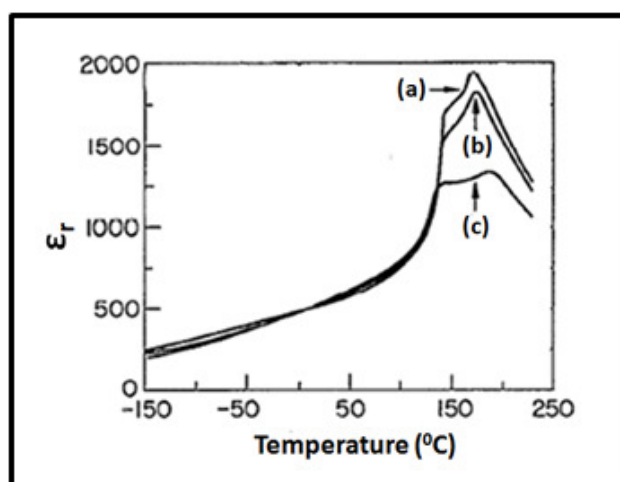


Figure 1.58 Dielectric response of $\text{Pb}_{0.98}\text{Nb}_{0.02}[(\text{Zr}_{1-x}\text{Sn}_x)_{0.94}\text{Ti}_{0.06}]_{0.98}\text{O}_3$ as a function of temperature where $x =$ a) 0.40, b) 0.45 and c) 0.50.

[Source: D. Viehland et al, *J. Appl. Phys.*, 75 (1994) 4137-4143]

The influence of Ti-content (y) on the dielectric response of $\text{Pb}_{0.98}\text{Nb}_{0.02}[(\text{Zr}_{0.55}\text{Sn}_{0.45})_{1-y}\text{Ti}_y]_{0.98}\text{O}_3$ at a fixed Sn-content is given in Fig. 1.59. With increasing Ti-content dielectric permittivity maximum increased to higher value with a narrow MCC state. Consequently increasing Ti-content suppress the formation of incommensuration and MCC state.

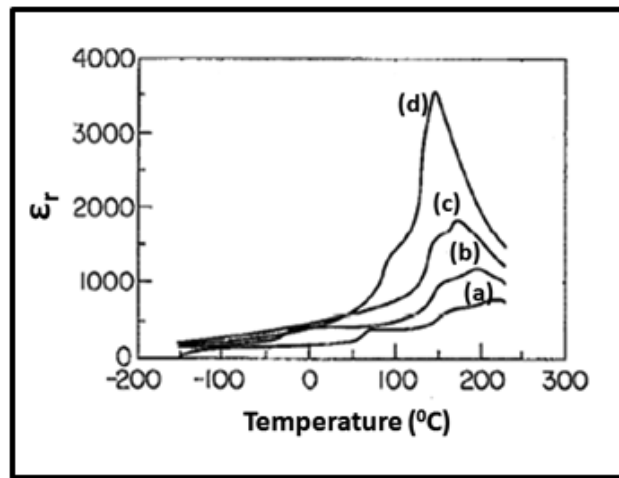


Figure 1.59 Dielectric response of $\text{Pb}_{0.98}\text{Nb}_{0.02}[(\text{Zr}_{0.55}\text{Sn}_{0.45})_{1-y}\text{Ti}_y]_{0.98}\text{O}_3$ as a function of temperature where $y =$ a) 0, b) 0.03, c) 0.06 and d) 0.09

[Source: D. Viehland et al, *J. Appl. Phys.*, 75 (1994) 4137-4143]

1.3.7.2 Effect of DC bias on incommensuration

In Fig. 1.60 dielectric constant of $\text{Pb}_{0.98}\text{Nb}_{0.02}[(\text{Zr}_{0.57}\text{Sn}_{0.43})_{0.90}\text{Ti}_{0.10}]_{0.98}\text{O}_3$ as a function of temperature for DC bias levels of 0, 2.5, 5, 10, 15 kV/cm is presented.

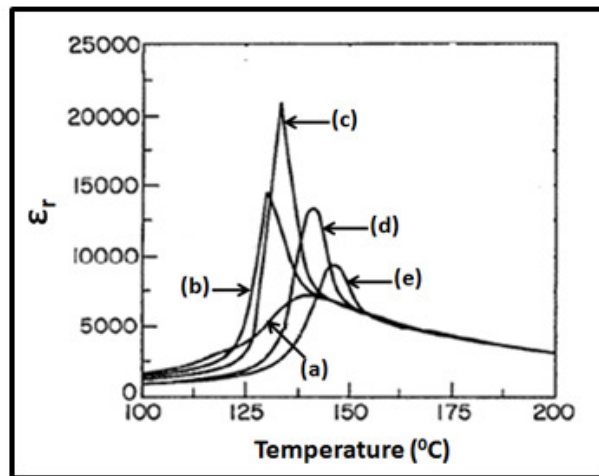


Figure 1.60 Dielectric response of $\text{Pb}_{0.98}\text{Nb}_{0.02}[(\text{Zr}_{0.57}\text{Sn}_{0.43})_{0.90}\text{Ti}_{0.10}]_{0.98}\text{O}_3$ as a function of temperature at dc bias levels a) 0, b) 2.5, c) 5, d) 10 and e) 15 kV/cm

[Source: D. Viehland et al, *J. Appl. Phys.*, 75 (1994) 4137-4143]

On application of electric field ($E \leq 5.0 \text{ kV/cm}$) the dielectric permittivity increases and the temperature of maximum dielectric permittivity also shifts to lower temperatures [Fig. 1.60(a), (b) and (c)]. On further increase of the DC bias, the dielectric permittivity is suppressed and temperature of maximum dielectric permittivity shifts to higher temperatures [Fig. 1.60(d) and (e)]. It is observed that by the application of electric field suppression of broadened MCC state is takes place and metastability of incommensurate phase is removed.

Based on the aforementioned effects of chemical composition, DC bias, temperature, etc on incommensurate modulations, Viehland et al¹¹⁴⁻¹¹⁸ suggested that frustration coming from competing ferroelectric ordering and antiferroelectric ordering is responsible for the presence of the incommensurate modulations. As we discussed in section 1.3.6, in Sn-modified PZT, free energy of ferroelectric and antiferroelectric states is nearly equal. This leads to an intrinsic competition between ferroelectric and antiferroelectric couplings just below Curie point resulting incommensurate modulations in the lattice¹¹⁴⁻¹¹⁷.

1.3.8 Incommensuration in La-modified antiferroelectric Lead Zirconate Titanate

Depending on compositions various phases exist in La-modified lead zirconate titanate (PLZT) phase diagram¹²⁰ including (i) antiferroelectric orthorhombic (AFE_O) (ii) rhombohedral ferroelectric (FE_R), (iii) tetragonal ferroelectric (FE_T), (iv) relaxor ferroelectric (RFE) and (v) paraelectric cubic (PE_C) as shown in Fig.1.61. For PZT compositions of lower Zr/Ti ratio, the introduction of La^{3+} at Pb-site results in relaxor characteristics. Systematic studies of La^{3+} -modified Lead Zirconate titanate of higher Zr- content has showed that with increased doping, the paraelectric-antiferroelectric transition proceed through an intermediate incommensurate region¹²¹⁻¹²³. The incommensurate structure was found stable below the temperature of maximum dielectric permittivity. FE and AFE states are of equal energy in PZT compositions having higher Zr content and small amount of La^{3+} -substitution interrupts long-range ferroelectric coupling and thus short range antiferroelectric state is stabilized.

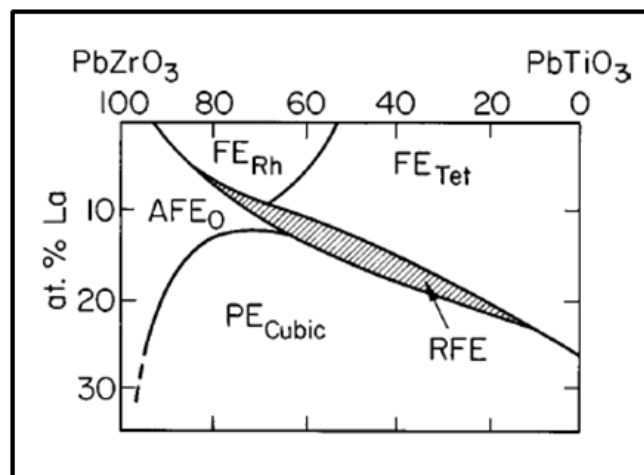
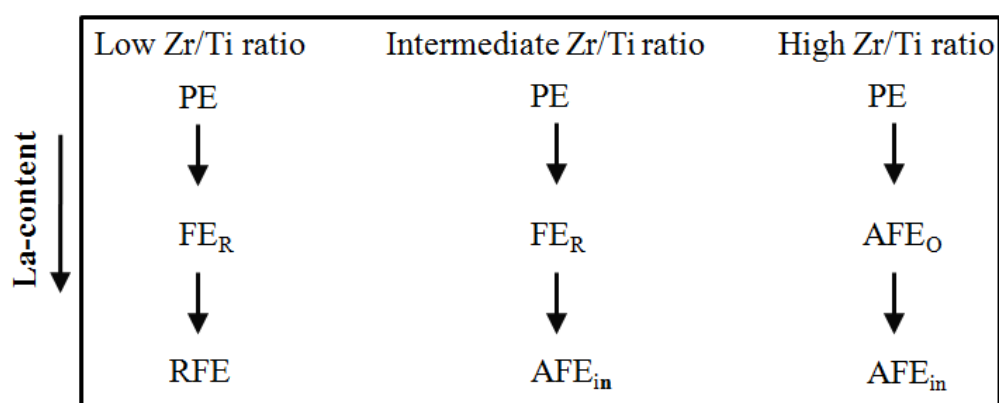


Figure 1.61 PLZT phase diagram

Further introduction of La^{3+} results in breaking of dipolar interaction associated with the ferroelectricity. Consequently there is a competition between broken dipolar and antiferroelectric interactions and hence incommensuration results. Investigations have demonstrated a general trend in the sequence of phase transformations in increased La^{3+} -content for various Zr/Ti ratios as given below.



Thus understanding the mechanistic aspects of such phase transition sequences are important.

References

- [1] V. M. Goldschmidt, *Skr. Nor. Viedenk.-Akad., Kl. I: Mater.-Naturvidensk. Kl.* 8 (1926).
- [2] B. Jaffe, W. R. Cook Jr. and H. Jaffe, "Piezoelectric ceramics", Academic Press, (1971) 49-51.
- [3] D. Damjanovic, "The science of hysteresis", I. Mayergoyz and G. Bertotti (Eds.), Elsevier, 3(2005).
- [4] D. Damjanovic, "Ferroelectric, dielectric and piezoelectric properties of ferroelectric thin films and ceramics", *Rep. Prog. Phys.*, 61(1998) 1267-1324.
- [5] N. Uchida and T. Ikeda, "Temperature and bias characteristics of Pb(Zr-Ti)O₃ families ceramics", *Jpn. J. Appl. Phys.*, 4 (1965) 867-880.
- [6] T. Surumi, Y. Kumano, N. Ohashi, T. Takenaka and O. Fukunaga, "90° domain reorientation and electric-field-induced strain of tetragonal lead zirconate titanate ceramics", *Jpn. J. Appl. Phys.*, 36 (1997) 5970-5976.
- [7] B. Noheda, J. A. Gonzalo, R. Guo, S.-E. Park, L. E. Cross, D. E. Cox and G. Shirane, "The monoclinic phase in PZT: new light on morphotropic phase boundaries", *AIP Conf. Proc.*, 535 (2000) 304-308.
- [8] B. Noheda, D. E. Cox, G. Shirane, J. A. Gonzalo, L. E. Cross and S.-E. Park, "A monoclinic ferroelectric phase in the PZT solid solution", *Appl. Phys. Lett.*, 74 (1999) 2059-2061.

- [9] R. Gerson, "Variation in ferroelectric characteristics of lead zirconate titanate ceramics Due to minor chemical modifications", *J. Appl. Phys.*, 31(1960)188-194.
- [10] F. Kulscar, "Electromechanical properties of lead titanate zirconate ceramics modified with certain three or five-valent additions", *J. Am. Ceram. Soc.*, 42 (1959) 343-349.
- [11] F. A. Kroger and H. J. Vink, "Relations between the concentrations of imperfections in crystalline solids", *Solid State Phys., Adv. Res. Appl.*, 3(1956) 307-435.
- [12] R. Gerson, "Dielectric properties of lead titanate zirconate ceramics at very low frequencies", *J. Appl. Phys.* 31 (1960) 1615-1617.
- [13] S. Takahashi, "Internal bias field effects in lead zirconate titanate ceramics doped with multiple impurities", *Jpn. J. Appl. Phys.*, 20 (1981) 95-101.
- [14] S. Takahashi, "Effects of impurity doping in lead zirconate titanate ceramics", *Ferroelectrics*, 41(1982) 143-156.
- [15] E. S. Kirkpatrick, K. A. Muller and R. S. Rubins, "Strong axial electron paramagnetic resonance spectrum of Fe^{3+} in SrTiO_3 due to nearest-neighbour charge compensation", *Phys. Rev.*, 135 (1964) A86-A90.
- [16] K. A. Muller, W. Berlinger and K. W. Blazey, "Electron paramagnetic resonance of Mn^{4+} in BaTiO_3 ", *Solid State Commun.*, 61 (1987) 21-25.
- [17] E. Siegel and K. A. Muller, "Structure of transition-metal-oxygen-vacancy pair centers", *Phys. Rev. B*, 19 (1979) 109-120.

- [18] P. V. Lambeck and G. H. Jonker, “Ferroelectric domain stabilization in BaTiO₃ by bulk ordering of defects”, *Ferroelectrics*, 22 (1978)729-731.
- [19] P. V. Lambeck and G. H. Jonker, “The nature of domain stabilization in ferroelectric perovskites” , *J. Phys. Chem. Solids*, 41(1986) 453-461.
- [20] M. E. Drougard and D. R. Young, “Domain clamping effect in barium titanate Single crystals” , *Phys. Rev.*, 94 (1954) 1561-1564.
- [21] D. C. Lupascu, Y. A. Genenko and N. Balke, “Aging in ferroelectrics”, *J. Am. Ceram. Soc.*, 89 (2006) 224–229.
- [22] U. Robels and G. Arlt, “Domain wall clamping in ferroelectrics by orientation of defects” , *J. Appl. Phys.*, 73 (1993) 3454-3460.
- [23] G. Arlt and H. Neumann, “Internal bias in ferroelectric ceramics: origin and time dependence”, *Ferroelectrics*, 87 (1988) 109-120.
- [24] K. Carl and K. H. Hardtl, “Electrical after-effects in Pb(Ti,Zr)O₃ ceramics”, *Ferroelectrics*, 17(1977) 473-486.
- [25] K. Uchino, *Ferroelectric device*, Dekker, New York (2000).
- [26] W. A. Schulze and K. Ogino, “Review of literature on aging of dielectrics”, *Ferroelectrics*, 87 (1988) 361-377.
- [27] G. H. Jonker, “Nature of aging in ferroelectric ceramics”, *J. Am. Ceram. Soc.*, 55 (1972) 57-58.
- [28] M. I. Morozov and D. Damjanovic, “Charge migration in PZT ceramics and its relation to ageing, hardening and softening”, *J. Appl. Phys.* 107 (2010) 034106-1-10.

- [29] Q. Tan, J. F. Li and D. Viehland, “Ferroelectric behaviours dominated by mobile and randomly quenched impurities in modified lead zirconate titanate ceramics”, *Philos. Mag. B*, 76 (1997) 59-74.
- [30] W. Liu, W. Chen, L. Yang, L. Zhang, Y. Wang, C. Zhou, S. Li and X. Ren, Ferroelectric aging effect in hybrid-doped BaTiO₃ ceramics and the associated large recoverable electrostrain”, *Appl. Phys. Lett.*, 89 (2006) 172908-1-3.
- [31] H. Bao , J. Gao , D. Xue , C. Zhou ,L. Zhang, W. Liu and X. Ren, “Control of ferroelectric aging by manipulating point defects”, *Ferroelectrics*, 401 (2010) 45-50.
- [32] C. Zhou, W. Liu, H . Bao, J. Gao, D. Xue and X. Ren, “Aging effect in acceptor-donor co-doped ferroelectrics”, *Ferroelectrics*, 404 (2010) 141-146.
- [33] Y. A. Genenko, J. Glaum, M. J. Hoffmann and K. Albe, “Mechanisms of aging and fatigue in ferroelectrics”, *Mater. Sci. Eng. B*, 192 (2015) 52–82.
- [34] M. Takahashi, “Space charge effect in lead zirconate ceramics caused by addition of impurities”, *Jpn. J. Appl. Phys.*, 9 (1970) 1236-1246.
- [35] M. Takahashi, “Electrical resistivity of lead zirconate titanate ceramics containing impurities”, *Jpn. J. Appl. Phys.*, 10 (1971) 643-651.
- [36] K. Okazaki and K. Sakata, “Space charge polarisation and aging of barium titanate ceramics”, *Electrotech. J. Jpn.*, 7(1962) 13-18.

- [37] H. Thomann, “Stabilization effects in piezoelectric lead zirconate titanate ceramics”, *Ferroelectrics*, 4 (1972) 141-146.
- [38] W. L. Warren, D. Dimos, B. A. Tuttle, R. D. Nasby and G. E. Pike “Electronic domain pinning in $\text{Pb}(\text{Zr,Ti})\text{O}_3$ thin films and its role in fatigue”, *Appl. Phys. Lett.*, 65 (1994) 1018-1020.
- [39] V. S. Postnikov, V. S. Pavlov and S. K. Turkov, “Internal friction in ferroelectrics due to interaction of domain boundaries and point defects”, *J. Phys. Chem. Solids*, 3 (1970) 1785-1791.
- [40] W. L. Warren, D. Dimos, B. A. Tuttle and D. M. Smyth, “Electronic and ionic trapping at domain walls in BaTiO_3 ”, *J. Am. Ceram. Soc.*, 77 (1994) 2753-2757.
- [41] W. L. Warren, D. Dimos, G. E. Pike, K. Vanheusden and R. Ramesh, “Alignment of defect dipoles in polycrystalline ferroelectrics”, *Appl. Phys. Lett.*, 67 (1995) 1689-1691.
- [42] X. Ren, “Large electric-field-induced strain in ferroelectric crystals by point-defect mediated reversible domain switching”, *Nat. Mater.*, 3 (2004) 91-94.
- [43] L. X. Zhang, W. Chen, and X. Ren, “Large recoverable electrostrain in Mn-doped $(\text{Ba,Sr})\text{TiO}_3$ ceramics”, *Appl. Phys. Lett.*, 85 (2004) 5658-5660.
- [44] Z. Feng and X. Ren, “Striking similarity of ferroelectric aging effect in tetragonal, orthorhombic and rhombohedral crystal structures”, *Phys. Rev. B*, 77 (2008) 134115-1-6.

- [45] W. L. Warren, D. Dimos, G. E. Pike, K. Vanheusden and R. Ramesh, “Alignment of defect dipoles in polycrystalline ferroelectrics”, *Appl. Phys. Lett.*, 67 (1995) 1689-1691.
- [46] X. Ren and K. Otsuka, “Universal symmetry property of point defects in crystals”, *Phys. Rev. Lett.*, 85(2000) 1016-1019.
- [47] K. Vani and V. Kumar, “Influence of defect mobility on electrostrain in acceptor-doped $\text{Ba}_{0.80}\text{Sr}_{0.20}\text{TiO}_3$ ”, *AIP Advances*, 2 (2012) 042177-1-4.
- [48] Y. Y. Guo, M. H. Qin, T. Wei, K. F. Wang and J. M. Liu, “Kinetics controlled aging effect of ferroelectricity in Al-doped and Ga-doped BaTiO_3 ”, *Appl. Phys. Lett.*, 97(2010)112906-1-3.
- [49] L. X. Zhang and X. Ren, “In-situ observation of reversible domain switching in aged Mn-doped BaTiO_3 single crystals”, *Phys. Rev. B*, 71(2005) 174108-1-8.
- [50] G. A. Samara and E. L. Venturini, “Ferroelectric/relaxor crossover in compositionally disordered perovskites”, *Phase Transitions*, 79(2006) 21- 40.
- [51] G. A. Samara, “The relaxational properties of compositionally disordered ABO_3 perovskites”, *J. Phys. Condens. Matter*, 15 (2003) R367- R411.
- [52] G. Burns and F. H. Dacol, “Glassy polarisation behavior in ferroelectric compounds $\text{Pb}(\text{Mg}_{1/3}\text{Nb}_{2/3})\text{O}_3$ and $\text{Pb}(\text{Zn}_{1/3}\text{Nb}_{2/3})\text{O}_3$ ”, *Solid State Commun.*, 48 (1983) 853-856.
- [53] K. Hirota, S. Wakimoto and D. E. Cox, “Neutron and x-ray scattering studies of relaxors”, *J. Phys. Soc. Jpn.*, 75 (2006) 111006-1-13.

- [54] S. N. Gvasaliya, B. Roessli, R. A. Cowley, P. Huber and S. G. Lushnikov, “Quasi-elastic scattering, random fields and phonon-coupling effects in $\text{PbMg}_{1/3}\text{Nb}_{2/3}\text{O}_3$ ”, *J. Phys: Condens. Matter*, 17(2005) 4343-4359.
- [55] S. N. Gvasaliya, V. Pomjakushin, B. Roessli, T. Strässle, S. Klotz and S. G. Lushnikov, “Anomalous pressure dependence of the atomic displacements in the relaxor ferroelectric $\text{Pb}(\text{Mg}_{1/3}\text{Ta}_{2/3})\text{O}_3$ ”, *Phys. Rev. B*, 73 (2006) 212102-1-4.
- [56] J. Hlinka, J. Petzelt, S. Kamba, D Noujni, and T. Ostapchuk “Infrared dielectric response of relaxor ferroelectrics”, *Phase Transitions*, 79 (2006) 41-78.
- [57] W. Dmowski, M. K. Akbas, P. K. Davies, and T. Egami, “Local structure of $\text{Pb}(\text{Sc}_{1/2}\text{Ta}_{1/2})\text{O}_3$ and related compounds”, *J. Phys. Chem. Solids*, 61 (2000) 229-237.
- [58] R. Blinc, A. Gregorovi, B. Zalar, R. Pirc, and S. G. Lushnikov, “ ^{45}Sc -NMR study of the relaxor transition in a lead scandotantalate single crystal”, *Phys. Rev. B*, 61 (2000) 253-257.
- [59] P. M. Woodward and K. Z. Baba-Kishi, “Crystal structures of the relaxor oxide $\text{Pb}_2(\text{Sc,Ta})\text{O}_6$ in the paraelectric and ferroelectric states”, *J. Appl. Cryst.*, 35 (2002) 233-242.
- [60] H. Yokota, T. Oyama and Y. Uesu, “Second-harmonic-generation microscopic observations of polar state in Li-doped KTaO_3 under an electric field”, *Phys. Rev. B*, 72 (2005) 144103-1-6.
- [61] A. Kumar, N. M. Murari, R. S. Katiyar and J. F. Scott, “Probing the ferroelectric phase transition through Raman spectroscopy in $\text{Pb}(\text{Fe}_{2/3}\text{W}_{1/3})_{1/2}\text{Ti}_{1/2}\text{O}_3$ thin films”, *Appl. Phys. Lett.*, 90(2007) 262907-1-30.

- [62] T. Y. Kim, H. M. Jang and S. M. Cho, “Short-ranged clusters with tetragonal symmetry in La-modified PbTiO_3 relaxor ferroelectrics”, *Solid state commun.*, 119(2001) 527-532.
- [63] F. Jiang, S. Kojima, C. Zhao and C. Feng, “Raman scattering on the B-site order controlled by A-site substitution in relaxor perovskite ferroelectrics”, *J. Appl. Phys.*, 88(2000) 3608-1-3.
- [64] M. D. Glinchuk, V. V. Laguta, I. P. Bykov, S. Nokhrin, V. P. Bovtun, M. A. Leschenko, J. Rosa and L. Jastrabik, “Nuclear magnetic resonance study of ion ordering and ion shifts in relaxor ferroelectrics”, *J. Appl. Phys.* 81(1997) 3561-3569.
- [65] V. V. Laguta, M. D. Glinchuk, I. P. Bykov, R. Blinc and B. Zalar, “NMR study of ionic shifts and polar ordering in the relaxor ferroelectric $\text{Pb}(\text{Sc}_{1/2}\text{Nb}_{1/2})\text{O}_3$ ”, *Phys. Rev. B*, 69 (2004) 054103-1-9.
- [66] G. Smolenskii, V. A. Isupov, A. I. Agranovskaya and S. N. Popov, “Ferroelectrics with diffuse phase transitions”, *Sov. Phys. Solid State*, 2 (1961) 2584-2588.
- [67] V. A. Isupov, I. P. Pronin, V. I. Sizykh, “Investigation of the diffuse ferroelectric phase transition in lead magnesium niobate”, *Ferroelectrics*, 90 (1989) 147-150.
- [68] G. Burns and F. H. Dacol, “Crystalline ferroelectrics with glassy polarisation behavior”, *Phys. Rev. B*, 28 (1983) 2527-2530.
- [69] L. E Cross, “Relaxor Ferroelectrics”, *Ferroelectrics*, 76 (1987) 241-267.

- [70] D. Viehland, J. Jang, L. E. Cross and M. Wuttig, “The dielectric relaxation of lead magnesium niobate relaxor ferroelectrics”, *Philos. Mag. B*, 64 (1991) 335-344.
- [71] D. Viehland, J. F. Li, S. J. Jang and L. E. Cross, “Dipolar-glass model for lead magnesium niobate”, *Phys. Rev. B*, 43 (1991) 8316-8320.
- [72] D. Viehland, S. J. Jang, L. E. Cross and M. Wuttig, “Freezing of the polarisation fluctuations in lead magnesium niobate relaxors”, *J. Appl. Phys.*, 68 (1990) 2916- 2921.
- [73] Y. Imry and S. K. Ma, “Random-field instability of the ordered state of continuous symmetry”, *Phys. Rev. Lett.*, 35 (1975) 1399-1401.
- [74] V. Westphal, W. Kleeman, M. D. Glinchuk, “Diffuse phase transitions and random field- induced domain states of the relaxor ferroelectric $\text{Pb}(\text{Mg}_{1/3}\text{Nb}_{2/3})\text{O}_3$ ”, *Phys. Rev. Lett.*, 6 (1992) 847-850.
- [75] M. D. Glinchuk and R. Farhi, “A random field theory based model for ferroelectric relaxors”, *J. Phys: Condens. Matter*, 8 (1996) 6985-6996.
- [76] H. Ohwa, M. Iwata, H. Orihara, N. Yasuda and Y. Ishibashi, “Observation of the distribution of the transition temperature in $\text{Pb}(\text{In}_{1/2}\text{Nb}_{1/2})\text{O}_3$ ”, *J. Phys. Soc. Jpn.*, 69 (2000) 1533-1545.
- [77] F. Chu, I. M. Reaney and N. Setter, “Investigation of relaxors that transform spontaneously into ferroelectrics”, *Ferroelectrics*, 151 (1994) 343-348.
- [78] C. Boulesteix, F. Varnier, A. Llebaria and E. Husson, “Numerical determination of the local ordering of $\text{Pb}(\text{Mg}_{1/3}\text{Nb}_{2/3})\text{O}_3$ (PMN) from high resolution electron microscopy images”, *J. Solid State Chem.* 108 (1994) 141-147.

- [79] M. Yoshida, S. Mori, N. Yamamoto, Y. Uesu and J. M. Kiat, “TEM observation of polar domains in relaxor ferroelectric $\text{Pb}(\text{Mg}_{1/3}\text{Nb}_{2/3})\text{O}_3$ ”, *Ferroelectrics*, 217 (1998) 327-333.
- [80] I. W. Chen, P. Li and Y. Wang, “Structural origin of relaxor perovskites”, *J. Phys. Chem. Solids*, 57 (1996) 1525-1536.
- [81] I. W. Chen, “Structural origin of relaxor ferroelectrics-revisited”, *J. Phys. Chem. Solids*, 61 (2000) 197-208.
- [82] C. Kittel, “Theory of antiferroelectric crystal”, *Phys. Rev.*, 82 (1951) 729-732.
- [83] E. Sawaguchi, H. Maniwa and S. Hoshino, “Antiferroelectric structure of lead zirconate”, *Phys. Rev.*, 83 (1951) 1078.
- [84] F. Jona, G. Shirane, F. Mazzi and R. Pepinsky, “X-ray and neutron diffraction study of antiferroelectric lead zirconate”, *Phys. Rev.*, 105 (1957) 849-856.
- [85] T. Asada and Y. Koyama, “Coexistence of ferroelectricity and antiferroelectricity in lead zirconate titanate”, *Phys. Rev. B*, 70 (2004) 104105-1-5.
- [86] A. Chauhan, S. Patel, R. Vaish and C. R. Bowen, “Anti-ferroelectric ceramics for high energy density capacitors”, *Materials*, 8(2015) 8009-8031.
- [87] Z. Zhou, Q. Yang, M. Liu, Z. Zhang, X. Zhang, D. Sun, T. Nan, N. Sun and X. Chen, “Antiferroelectric materials, applications and recent progress on multiferroic heterostructures”, *Spin*, 5 (2015) 1530001-1-13.

- [88] B. Ma, D. K. Kwon, M. Narayanan and U. Balachandran, “Leakage current characteristics and dielectric breakdown of antiferroelectric $\text{Pb}_{0.92}\text{La}_{0.08}\text{Zr}_{0.95}\text{Ti}_{0.05}\text{O}_3$ film capacitors grown on metal foils”, *J. Phys. D: Appl. Phys.*, 41 (2008) 205003-1-7.
- [89] S. E. Park, M. J. Pan, K. Markowski, S. Yoshikawa and L. E. Cross, “Electric field phase transition of antiferroelectric lead lanthanum zirconate titanate stannate ceramics”. *J. Appl. Phys.*, 82 (1997) 1798–1803.
- [90] P. Yang and D. A. Payne, “Thermal stability of field-forced and field-assisted antiferroelectric-ferroelectric phase transformations in $\text{Pb}(\text{Zr},\text{Sn},\text{Ti})\text{O}_3$ ”, *J. Appl. Phys.*, 71 (1992) 1361–1367.
- [91] W. Y. Ling, C. Z. Ming, S. Y-Ren and D. X-Hu, “Phase transition study of PZT 95/5 ceramics”, *Physica B*, 150 (1988) 168-174.
- [92] X. Hao, J. Zhai, L. B. Kong and Z. Xu, “A comprehensive review on the progress of lead zirconate-based antiferroelectric materials”, *Prog. Mater. Sci.*, 63 (2014) 1–57.
- [93] G. Shirane, E. Sawaguchi and Y. Takagi, “Dielectric Properties of Lead Zirconate”, *Phys. Rev.*, 84 (1951) 476-481.
- [94] S. Roberts, “Dielectric properties of lead zirconate and barium-lead zirconate”, *J. Am. Ceram. Soc.*, 33 (1950) 63-66.
- [95] V. J. Tennery, “High-temperature phase transitions in PbZrO_3 ”, *J. Am. Ceram. Soc.*, 49 (1966) 483-486.
- [96] V. J. Tennery, “A study of the phase transitions in PbZrO_3 ”, *J. Electrochem. Soc.*, 112 (1965) 1117-1120.

- [97] Z. Ujma and J. Handerek, "Phase transitions and spontaneous polarisation in PbZrO_3 ", *Phys. Stat. Sol. (a)*, 28 (1975) 489-496.
- [98] Z. Xu, X. Dai, D. Viehland and D. A. Payne, "Ferroelectric domains and incommensuration in the intermediate phase region of lead zirconate", *J Am. Ceram. Soc.*, 78 (1995) 2220-2224.
- [99] D. Viehland, "Transmission electron microscopy study of high Zr-content lead zirconate titanate", *Phys. Rev. B*, 52 (1995) 778-791.
- [100] X. Dai, J. F. Li and D. Viehland, "Weak ferroelectricity in antiferroelectric lead zirconate", *Phys. Rev. B*, 51 (1995) 2651-2655.
- [101] B. A. Scott and G. Burns, "Crystal growth and observation of the ferroelectric phase of PbZrO_3 ", *J. Am. Ceram. Soc.*, 55 (1972) 331-333.
- [102] G. Shirane, "Ferroelectricity and antiferroelectricity in ceramic PbZrO_3 containing Ba or Sr", *Phys. Rev.*, 86 (1952) 219-227.
- [103] B. P. Pokharel and D. Pandey, "Dielectric studies of phase transitions in $(\text{Pb}_{1-x}\text{Ba}_x)\text{ZrO}_3$ ", *J. Appl. Phys.* 88 (2000) 5364-5373.
- [104] S. S. N. Bharadwaja, S. Saha, S. Bhattacharyya and S. B. Krupanidhi, "Dielectric properties of La-modified antiferroelectric PbZrO_3 thin films", *Mater. Sci. Eng. B*, 88 (2002) 22-25.
- [105] S. S. N. Bharadwaja and S. B. Krupanidhi, "Study of La-modified antiferroelectric PbZrO_3 thin films", *Thin Solid Films*, 423 (2003) 88-96.
- [106] J. Parui and S. B. Krupanidhi, "Effect of La-modification on antiferroelectric and dielectric phase transition in sol-gel grown PbZrO_3 thin films", *Solid State Commun.*, 150 (2010) 1755-1759.

- [107] D. Berlincourt, H. H. A. Krueger and B. Jaffe, “Stability of phases in modified lead zirconate with variation in pressure, electric field, temperature and composition”, *J. Phys. Chem. Solids*, 25 (1964) 659–674.
- [108] E. Cockayne and K. M. Rabe, “Pressure dependence of instabilities in perovskite PbZrO_3 ”, *J. Phys. Chem. Solids*, 61 (2000) 305-308.
- [109] J. Meng, G. Zou, Q. Cui, Z. Zhu and Z. Du, “Raman spectra and pressure-induced phase transition in nanocrystalline PbZrO_3 ”, *Solid State Commun.*, 91 (1994) 519-521.
- [110] O. E. Fesenko, R. V. Kolesova and Y. G. Sindeev, “The structural phase transitions in lead zirconate in super high electric fields”, *Ferroelectrics*, 20 (1978) 177–178.
- [111] J. Handerek, M. Pisarski and Z. Ujma, “The influence of an electric field and hydrostatic pressure on dielectric properties and phase transitions in PbZrO_3 ”, *J. Phys. C: Solid State Phys.*, 14 (1981) 2007-2016.
- [112] E. Sawaguchi, “Ferroelectricity versus antiferroelectricity in the solid solutions of PbZrO_3 and PbTiO_3 ”, *J. Phys. Soc. Jpn.*, 8 (1953) 615-629.
- [113] B. Jaffe, W. R. Cook, H. Jaffe, “Piezoelectric ceramics”, Academic Press, (1971) 129-131.
- [114] D. Viehland, D. Forst, Z. Xu and J. F. Li, “Incommensurately modulated polar structures in antiferroelectric Sn-modified lead zirconate titanate: the modulated structure and its influences on electrically induced polarisations and strains”, *J. Am. Ceram. Soc.*, 78 (1995) 2101-2112.

- [115] D. Forst, J. F. Li, Z. Xu and D. Viehland, “Incommensurately modulated polar structures in antiferroelectric tin-modified lead zirconate titanate: II, dependence of structure-property relations on tin content”, *J. Am. Ceram. Soc.*, 81 (1998) 2225-2236.
- [116] D. Viehland, D. Forst, and J. F. Li, “Compositional heterogeneity and the origins of the multicell cubic state in Sn-doped lead zirconate titanate ceramics”, *J. Appl. Phys.*, 75 (1994) 4137-4143.
- [117] Z. Xu, D. Viehland, P. Yang and D. A. Payne, “Hot-stage transmission electron microscopy studies of phase transformations in tin-modified lead zirconate titanate”, *J. Appl. Phys.*, 74 (1993) 3406-3413.
- [118] Z. Xu, D. Viehland and D. A. Payne, “An incommensurate-commensurate phase transformation in antiferroelectric tin-modified lead zirconate titanate”, *J. Mater. Res.*, 10 (1995) 453-460.
- [119] H. He and X. Tan, “Electric-field-induced transformation of incommensurate modulations in antiferroelectric $\text{Pb}_{0.99}\text{Nb}_{0.02}[(\text{Zr}_{1-x}\text{Sn}_x)_{1-y}\text{Ti}_y]_{0.98}\text{O}_3$ ”, *Phys. Rev. B*, 72 (2005) 024102-1-10.
- [120] G. H. Haertling and C. E. Land, “Hot-pressed (Pb,La)(Zr,Ti)O₃ ferroelectric ceramics for electro optic applications”, *J. Am. Ceram. Soc.*, 54 (1971) 1-11.
- [121] Z. Xu, X. Dai, J. F. Li and D. Viehland, “Coexistence of incommensurate antiferroelectric and relaxor like ferroelectric orderings in high Zr-content La-modified lead zirconate titanate ceramics”, *Appl. Phys. Lett.*, 68 (1996) 1628-1630.

- [122] D. Viehland, X. H. Dai, J. F. Li, and Z. Xu, “Effects of quenched disorder on La-modified lead zirconate titanate: Long- and short range ordered structurally incommensurate phases, and glassy polar clusters”, *J. Appl. Phys.*, 84 (1998) 458-471.
- [123] Z. Xu, X. Dai and D. Viehland, “Incommensuration in La-modified antiferroelectric lead zirconate titanate ceramics”, *Appl. Phys. Lett.*, 65 (1994) 3287-3289.

Experimental Methods and Characterization Techniques

• Contents •

- 2.1 Ceramic processing
- 2.2 Characterization techniques
- References

Experimental methods adopted for the present investigation are given in this chapter. Different characterization techniques employed are highlighted.

2.1 Ceramic processing

Conventionally, ferroelectric ceramics are prepared by solid state reaction method. Apart from solid state route, various chemical methods are also employed for the synthesis of ceramic powders includes sol-gel process¹⁻⁸, co-precipitation of metal hydroxides⁹ and oxalates¹⁰ and hydrothermal synthesis¹¹. Details of materials used and the experimental procedure followed are given in respective sections in each chapter.

2.1.1 Solid state route

The solid-state reaction route is the most widely used method for the preparation of polycrystalline solids from a mixture of solid starting materials such as oxides, carbonates etc. Since solids do not react together at room temperature over normal time scales, it is necessary to heat them to much higher temperatures for the reaction to occur at an appreciable rate. The factors on which the feasibility and rate of a solid state reaction depend include reaction conditions, structural properties of the reactants, surface area of the solids and temperature treatments. The solid state reaction method involves following steps as shown in the flow chart given in Fig. 2.1.

The raw materials are weighed according to stoichiometry and mixed mechanically. Mixing was usually done by either ball or attrition milling. In ball milling way of mixing, weighed powders were mixed with zirconia balls and water in an appropriate ratio and ball milled for long period, preferably 24 hours. Then washed with distilled water and dried. After mixing, compositions are usually calcined in powder form. During the calcination step the solid phase reaction takes place between the constituents. Calcined powder crushed and further mixed with binder for pelletizing. The shaped samples are taken to a higher temperature for sintering. The sintering temperature and time should

be optimum for proper densification. Layer of metallic silver applied in paste form and cured to form a continuous conductive layer bonded to the polished surface of sintered sample.

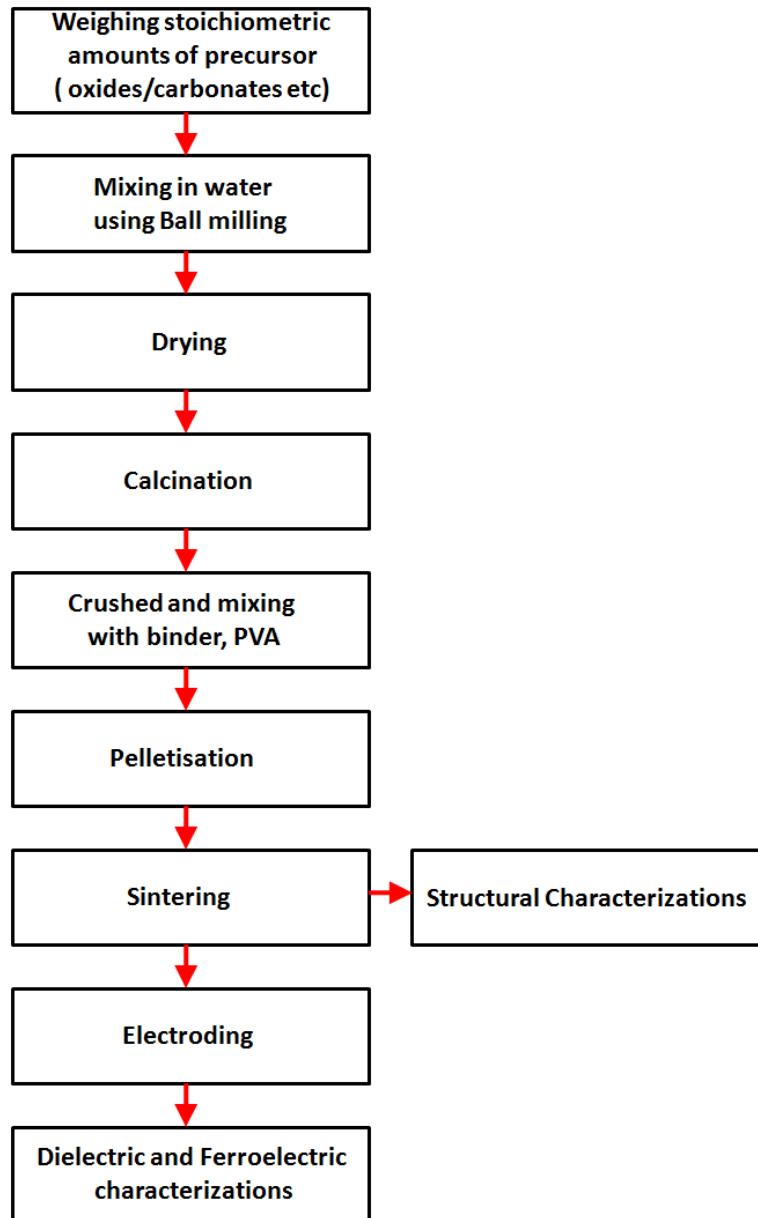


Figure 2.1 Flow chart for solid state reaction method

2.1.2 Sol-Gel method

Sol-gel process possess many advantages over conventional methods since it offers convenient fabrication procedure with high purity, molecular homogeneity, low-temperature processing.

A sol is a stable dispersion of either polymers or colloidal particles in a given solvent. A gel consists of a three dimensional continuous network within a liquid which exhibits no flow when in the steady-state. Considering a colloidal gel, the three dimensional network is constructed from agglomeration of colloidal particles. But in a polymer gel, it is the aggregates of sub-colloidal particles produce polymeric substructure. The elementary step in the sol-gel process is the formation of an oxide network through the polycondensation of the molecular precursors in a liquid phase. It is through the van der Waals forces or hydrogen bonds that the sol particles found to interact. Advantages of Sol-gel process for synthesis of materials are;

- i. Enables mixing at an atomic level
- ii. Multi component compounds may be prepared with a controlled stoichiometry
- iii. Prevents the problems with co-precipitation
- iv. Results in small particles, which are easily sinterable.

The major advantage of this system is that the entire processing can be done under ambient conditions. Precursors like acetates, metal alkoxides in suitable solvents are subjected to stirring in the presence of chelating ligands like diethanol amine and acetyl acetone. Chelating ligands impart stability to the precursor solution. Water was added to induce hydrolysis and the solution was filtered and kept for gelation at room temperature for 1 week. The gel-

derived powders, obtained after calcination was isostatically pressed into pellets and followed by sintering at higher temperature. The flow chart for the Sol-Gel method is as given in Fig. 2.2.

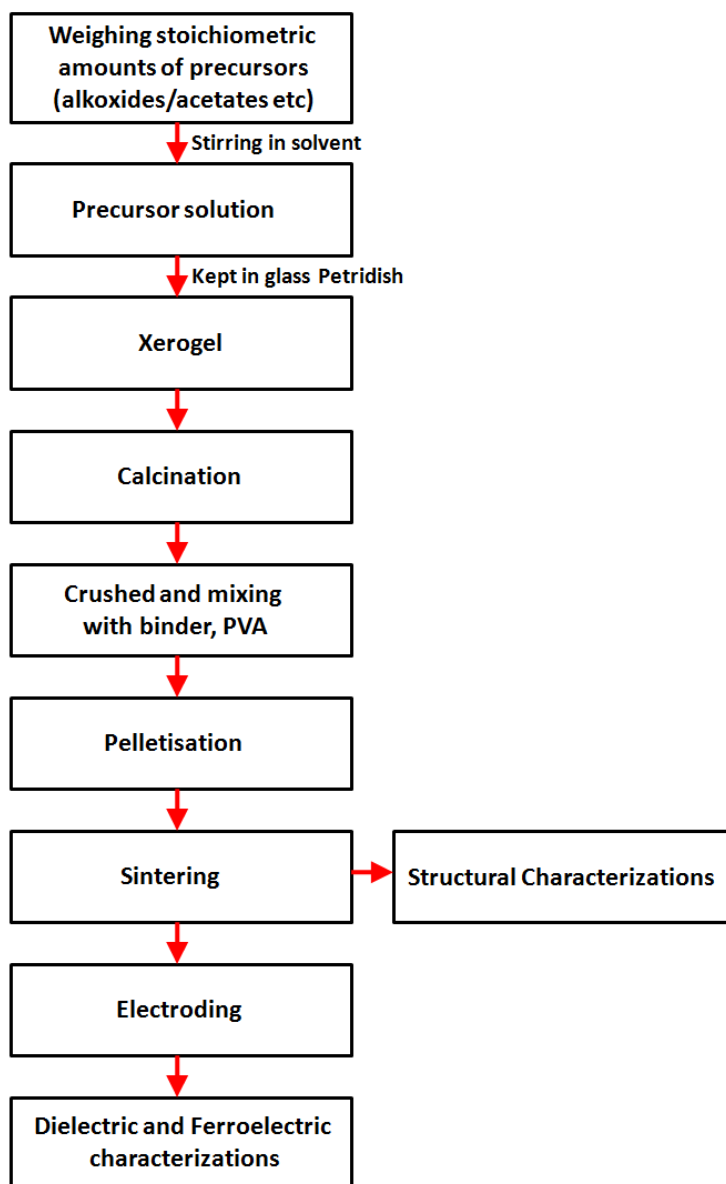


Figure 2.2 Flow chart for Sol-Gel method

2.2 Characterization techniques

2.2.1 X-ray powder diffraction¹²

X-ray powder diffraction (XRD) is an important analytical technique used for phase analysis of a crystalline material and can provide information about unit cell dimensions. X-rays are used to study the crystal structure since the wavelength of X-rays is similar to atomic spacing in a crystal. In a crystal, atoms are arranged in a periodic manner with long range order and therefore produce diffraction when X-rays incident on it. This scattering from atoms produces diffraction patterns which hold the information about atomic arrangements within the crystal. When X-ray of wavelength ' λ ' falls on the sample the interaction between the incident ray and the diffracted ray of the sample produces constructive interference only when a condition called Bragg's Law is satisfied (Fig. 2.3). Bragg's Law relates the wavelength of electromagnetic radiation ' λ ' to the diffraction angle ' θ ', and the lattice spacing, ' d ' in a crystalline sample and is given by,

$$n\lambda = 2d \sin\theta \quad (2.1)$$

where n is a positive integer.

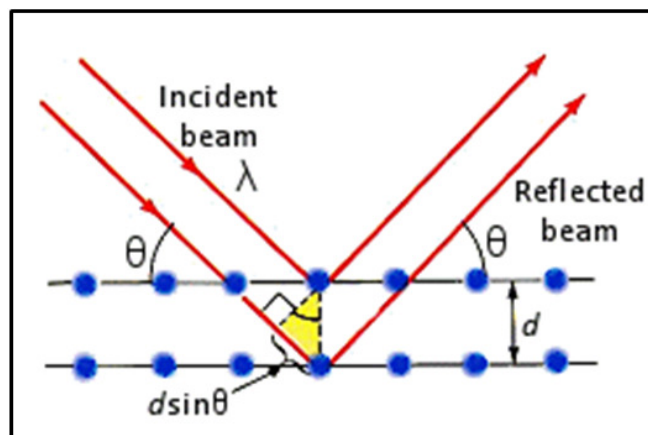


Figure 2.3 Schematic of Bragg Diffraction

In X-ray diffraction pattern, the position of the diffraction peaks is determined by the interatomic distance d_{hkl} and type of the atom determines the intensity of the peaks. Peak widths and shape of diffraction patterns mostly depend on the instrumental and microstructural parameters. The X-ray diffraction patterns of the samples in the present work, were obtained from an X-ray diffractometer (D- 5005, Bruker, Germany) using Ni filtered $\text{CuK}\alpha$ -radiation having wavelength (λ) of 1.54\AA (Fig. 2.4).

In order to precisely determine the structure, refinement of XRD data using Rietveld method was carried out by using GSAS program¹³. Pseudo-Voigt function was used for peak profile refinement.



Figure 2.4 X-ray Diffractometer

2.2.2 Raman spectroscopy^{14,15}

Raman spectroscopy is a form of vibrational spectroscopy and it arises from a change in the polarizability of the molecule due to an interaction of the

light. Thus the observed bands are due to specific molecular vibrations. When a beam of light is impinged upon a molecule, photons are absorbed by the materials and get scattered. Majority of these scattered photons are found to have the same wavelength as that of the incident photons and the corresponding scattering is called Rayleigh scattering. During the scattering process, the incident photon excites an electron into a higher virtual state following this electron decays back to a lower energy state by emitting a scattered photon. As the electron decays back to the same level as that of initial in Rayleigh scattering, it is referred as a form of elastic scattering. In Raman scattering the resulting rovibronic state of the molecule is a different rotational or vibrational state than the one in which the molecule was originally, before interacting with the incoming photon. The difference in energy between the original rovibronic state and this resulting rovibronic state leads to a shift in the emitted photon's frequency away from the excitation wavelength, the so-called Rayleigh line. As the electron excited in the scattering process decays to a different level than initial in the Raman effect and is termed inelastic scattering. It is called inelastic scattering because the energy and the momentum transfer between the photons and the molecules during the interaction results in a difference in energy between the incident and scattered photons. In particular, the difference is equal to the difference in energy between the initial and final rovibronic states. The description of scattering involving virtual state is as shown in Fig. 2.5. If the final vibrational state of the molecule is more energetic than the initial state, the inelastically scattered photon will be shifted to a lower frequency for the total energy of the system to remain balanced. This shift in frequency is designated as a Stokes shift. If the final vibrational state is less energetic than the initial state, then the inelastically scattered photon will be shifted to a higher frequency, and this is designated as an anti-Stokes shift.

The main components of a Raman spectrometer are (i) a light source, (ii) optical components, such as lenses and mirrors, to focus the light onto a sample and collect the scattered light, (iii) a spectrometer, and (iv) a detector.

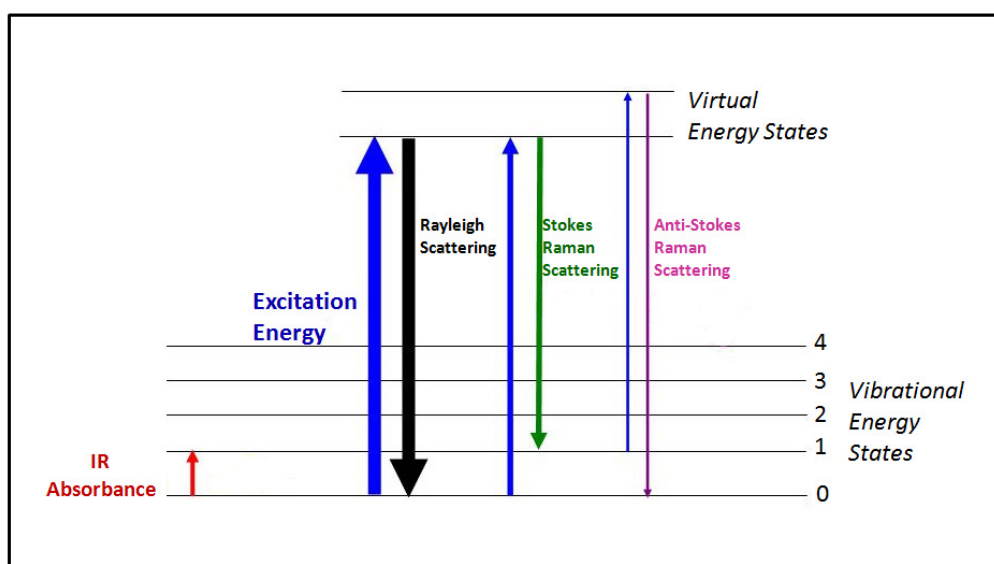


Figure 2.5 Energy level diagrams for Raman and Rayleigh scattering

A laser emitting monochromatic light is the light source found in Raman spectrometer. Elastic scattered radiation at the wavelength corresponding to the laser line (Rayleigh scattering) is filtered out by either a notch filter, edge pass filter, or a band pass filter, while the rest of the collected light is passed onto a spectrometer and the detector (CCD camera). Due to the Raman scattering of the samples, the energy of the laser photons being shifted up or down. Raman shifts are typically reported in wavenumbers, which have units of inverse length, as this value is directly related to energy. Most commonly, the unit chosen for expressing wavenumber in Raman spectra is inverse centimetres (cm^{-1}). Raman spectra of the samples were recorded using a Raman spectrometer (DXR Raman microscope, Thermo Scientific, USA) with a laser line of 532 nm and a laser power of 10 mW (Fig. 2.6).



Figure 2.6 DXR Raman microscope (Thermo Scientific USA)

2.2.3 Electron Paramagnetic Resonance spectroscopy¹⁵

Electron paramagnetic resonance (EPR) is a branch of magnetic resonance spectroscopy shown by molecules containing electrons with unpaired spins. EPR spectroscopy offers a correlation between the material properties and the defect chemistry. Also, it gives a clear idea about the local microstructure at the site of the functional center, including the valence state and site of incorporation of aliovalent dopant ions.

2.2.3.1 Origin of EPR signal

An electron is a negatively charged particle with certain mass and it mainly has two kinds of moments. The first one due to the motion around the nucleus, is orbital magnetic moment and the other due to spinning around its

own axis, is the spin magnetic moment. For an electron of spin $s = \frac{1}{2}$ the spin angular momentum quantum number can have values of $m_s = \pm \frac{1}{2}$ which in the absence of magnetic field leads to a doubly degenerate spin energy state. When an external magnetic field is applied, this degeneracy is resolved. The low energy state has the spin magnetic moment aligned with the field and corresponds to the quantum number, $m_s = -\frac{1}{2}$, while the high energy state, $m_s = +\frac{1}{2}$, has its moment opposed to the field. From quantum mechanics, the energies for an electron with $m_s = \pm \frac{1}{2}$ is,

$$E = g\beta B_0 m_s = \pm \frac{1}{2} g\beta B_0 \quad (2.2)$$

and the difference between these two states are given by:

$$\Delta E = h\nu = g\beta B_0 \quad (2.3)$$

where ' h ' is the Planck's constant, ' ν ' the frequency of radiation, ' β ' the Bohr magneton, B_0 the field strength and ' g ' the spectroscopic splitting factor. With the intensity of the applied magnetic field increasing, the energy difference between the energy levels widens until it matches with the frequency of radiation and transition between the two different electron spin energy states occurs upon absorption of a quantum of radiation in the radio frequency or microwave region and results in absorption of photons as shown in Fig. 2.7.

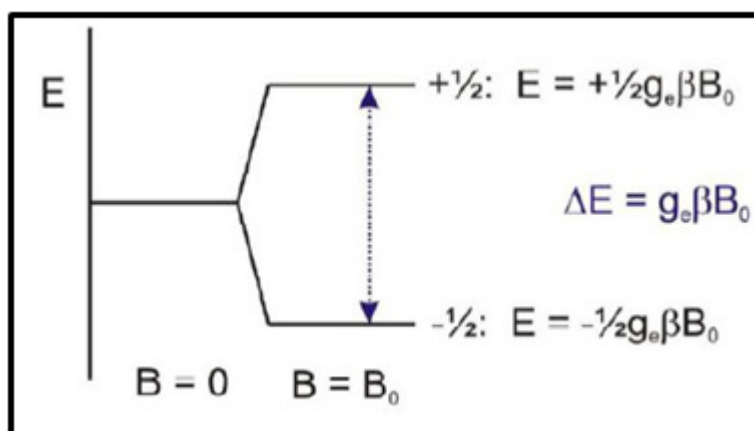


Figure 2.7 Induction of the spin state energies as a function of the magnetic field B_0

2.2.3.2 Factors affecting the magnitude of the ‘ g ’ factor

When an electron in space with no outside forces on it and places it on to a molecule, its total angular momentum changes because, in addition to the intrinsic spin angular momentum (S), it now also possesses some orbital angular momentum (L). An electron with orbital angular momentum is in effect a circulating current, and so there is also a magnetic moment arising from the orbital angular momentum. These two magnetic moments interact, and the energy of this spin-orbit interaction depends on their relative orientations. The value of ‘ g ’ for an unpaired electron in a gaseous atom or ion, for which Russell-Saunders coupling is applicable, is thus given by following equation:

$$g = 1 + \frac{J(J+1) + S(S+1) - L(L+1)}{2J(J+1)} \quad (2.4)$$

The actual value of ‘ g ’ for free electron is 2.0023 where 0.0023 is due to a relativistic correction. When there is a chemical environment about the electron, the orbital motion of the electron is strongly perturbed and the orbital degeneracy is partially removed or quenched. The properties of the transition

metals are determined by the relative magnitudes of the crystal field and spin-orbit coupling.

2. 2.3.3 Orientation dependence of ‘ g ’ factor

Magnitude of ‘ g ’ depends upon the orientation of the molecule containing the unpaired electron with respect to the magnetic field. In a solution or in the gas phase, ‘ g ’ is averaged over all orientations because of the free motion of the molecules, but in crystal, movement is restricted. If the paramagnetic radical or ion is located in a perfectly cubic crystal site, the ‘ g ’ value is independent of the orientation of the crystal and is said to be isotropic. In a crystal site of lower symmetry the ‘ g ’ value depends upon the orientation of the crystal and is said to be anisotropic. The z direction is defined coincident with the highest-fold rotation axis. The ‘ g_z ’ value is equivalent to $g_{||}$, as the ‘ g ’ value obtained when the z axis is parallel to the external magnetic field. The ‘ g ’ values along the x and y axes are ‘ g_x ’ and ‘ g_y ’, which in a tetragonal site are equal and referred to ‘ g_{\perp} ’ as the ‘ g ’ value obtained with the external magnetic field perpendicular to the z axis.

2. 2.3.4 Hyperfine Interaction

The nuclei of the atoms in a molecule or complex usually have their own fine magnetic moments. Such magnetic moments occurrence can produce a local magnetic field intense enough to affect the electron. Such interaction between the electron and the nuclei produced local magnetic field is called the hyperfine interaction and the splitting resulting from the interaction of the nuclear spin with the electron spin is called hyperfine structure. Then the energy level of the electron can be expressed as:

$$H_s = g\beta B_0 m_s + a m_s m_I \quad (2.5)$$

where 'a' is the hyperfine coupling constant and m_I is the nuclear spin quantum number. Since there are $2I + 1$ possible values of m_I ($m_I = I, I-1, I-2, \dots, -I$), the hyperfine interaction terms splits the transition into $(2I + 1)$ lines of equal intensity. For example, interaction of the electron with a nucleus with $I = \frac{1}{2}$ (for example a proton) will yield an EPR spectrum containing two lines (Figs. 2.8 and 2.9). When an unpaired electron comes in the vicinity of a nucleus with a spin, I , an interaction takes place which causes the absorption signal to be split into $(2I+1)$ components. From magnetic considerations, the interaction of a proton nuclear moment corresponding to quantum number $m_I = +\frac{1}{2}$ with electron spin moment corresponding to the quantum number $m_S = -\frac{1}{2}$ will lead to a lower energy than the interaction of moments of $m_I = -\frac{1}{2}$ and $m_S = -\frac{1}{2}$. Similarly the interaction of the moment from $m_S = +\frac{1}{2}$ and $m_I = -\frac{1}{2}$ will lead to a lower energy than interaction with $m_I = +\frac{1}{2}$. The local field of the nucleus either adds or subtracts from the applied B_0 field. As a result the ground state and excited-state energy levels are split in two (Fig. 2.8). In the EPR experiment one can detect two lines instead of one (Fig. 2.9). Not all transitions are allowed because of selection rules. The selection rules in EPR are: $\Delta m_I = 0$ and $\Delta m_S = \pm 1$. Energies for the two transitions observed are then $g\beta B_0 \pm \frac{1}{2}a$ and the separation between the two peaks is 'a', the hyperfine splitting constant.

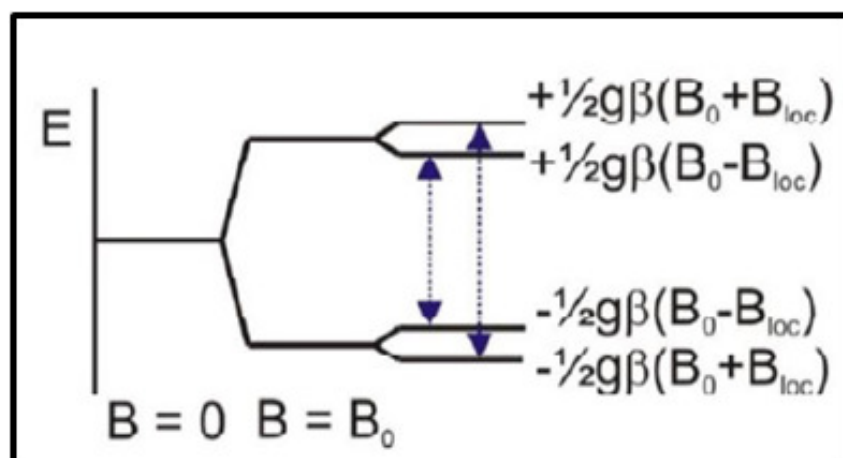


Figure 2.8 Energy states for an electron in a magnetic field effect of a nuclear spin of $\frac{1}{2}$

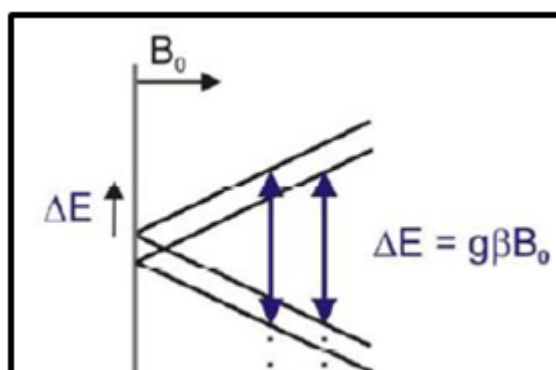


Figure 2.9 EPR spectrum of single electron interacting with a magnetic nucleus with nuclear spin, $I = \frac{1}{2}$.

2.2.3.5 Interactions affecting the energies of unpaired electrons in transition metal ion complexes

All the interactions to which unpaired electrons in a transition metal ion are subjected to can be expressed by the following equation:

$$W = W_F + V + W_{LS} + W_{SS} + \beta H(L + 2S) + W_N - \gamma \beta_N \cdot H \cdot I \quad (2.6)$$

where W is the energy of the ion in a complex, W_F is the energy of the free ion in the gaseous state, V is the electrostatic energy due to the crystal

field, W_{LS} is the energy associated with spin-orbit coupling, W_{SS} is the magnetic interaction between electron spins, $\beta H(L + 2S)$ is the effect of the external magnetic field and W_N is the interaction of the nuclear moment with the electron spin undergoing the transition.

Illustration of zero-field splitting can be done by considering a paramagnetic species with two unpaired electrons. In this case, the total spin quantum number, $S = 1$ ($m_s = -1, 0, +1$), which is the sum of the spin quantum numbers of each of the unpaired electrons. The two possible transitions for the above spin system, which obeys selection rule, $\Delta m_s = \pm 1$ are $0 \rightarrow 1$ and $-1 \rightarrow 0$ are as shown in Fig. 2.10 (a). In the absence of zero-field splitting, these transitions are degenerate and only one signal is observed in the EPR spectrum. Zero-field splitting removes the degeneracy in m_s as indicated in Fig. 2.10(b). After the application of external magnetic field, the obtained transitions are no more degenerate. As a result, two peaks are obtained in the spectrum. When Zero-field splitting, $ZFS \gg \gg$ energy of the microwave radiation, ' $h\nu$ ', the splitting will be like that shown in Fig. 2.10(c). The transitions between the doublets are forbidden because the spin has to change by more than ± 1 and thus EPR signal cannot be detected in this case.

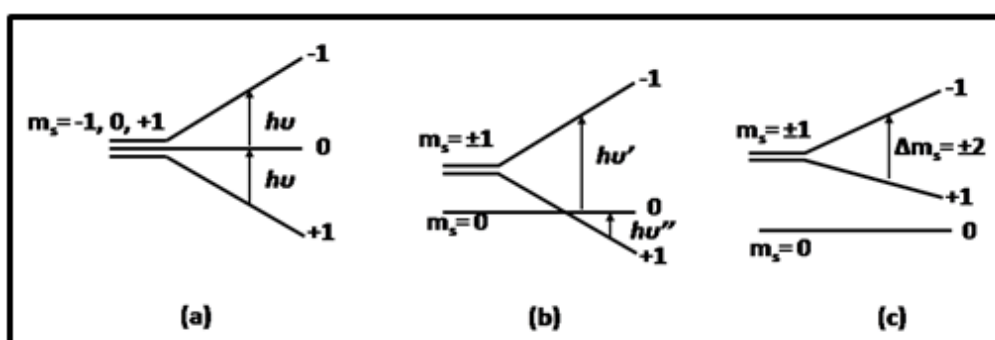


Figure 2.10 Spin levels of $S=1$ (a) without ZFS (b) with ZFS showing allowed transitions and (c) with $ZFS \gg h\nu$ showing forbidden transitions.

2.2.3.6 Theoretical description- spin-Hamiltonian concept

The spin Hamiltonian is a mathematical expression of the different interactions that exist in transition metal ions or radicals. The EPR spin Hamiltonian for an ion in an axially symmetric field, i.e., tetragonal or trigonal is:

$$H = D[S_z^2 - \frac{1}{3} S(S+1)] + g_{||} \beta H_z S_z + g_{\perp} \beta (H_x S_x + H_y S_y) + A_{||} S_z I_z + A_{\perp} (S_x I_x + S_y I_y) + Q [I_z^2 - \frac{1}{3} I(I+1)] - \gamma \beta_N H_0 I \quad (2.7)$$

In the above equation, first term describes the zero-field splitting, the next two terms describe the effect of the magnetic field on the spin multiplicity remaining after zero field splitting, the terms $A_{||}$ and A_{\perp} measure the hyperfine splitting parallel and perpendicular to the main axis, 'Q' measures the small changes in the spectrum produced by the quadrupole interaction. Quadrupole interaction is due to the fact that the nuclear magnetic moment μ_N can interact directly with the external field $\mu_N H_0 = \gamma \beta_N H_0 I$ where 'γ' is the nuclear magnetogyric ratio and β_N is the nuclear Bohr magneton. This interaction can only affect the paramagnetic resonance when the unpaired electrons are coupled to the nucleus by nuclear hyperfine or quadrupole interactions.

Owing to the different electronic configurations, and therefore different numbers of unpaired electrons, different spin-Hamiltonians have to be used in order to describe the magnetic and electric interactions of the transition-metal ions in the perovskite lattice. The information content of EPR spectra is embodied in a spin-Hamiltonian that generally is obtained after numerical spectrum simulation. To transfer the accurately determined spin-Hamiltonian parameters into structural information, the quadrupole FS interaction may be exploited that sensitively probes the electrical field gradient at the dopant-site.

Electron Paramagnetic Resonance spectroscopy of specimens were carried out using an EPR spectrometer (Model-JES FA200, JEOL, Japan) in the X band frequency of 9.17 GHz (Fig. 2.11).



Figure 2.11 EPR Spectrometer

2.2.3.7 Simulation techniques

Only the simplest of cw ESR spectra, those with few, sharp, well-resolved and sufficiently intense lines can be analyzed in a straightforward manner. Often, physical information is implicit and hidden in the details of the line shape. It is not always possible to assign lines, especially in spectra from molecules with many magnetic nuclei. When several interactions are of similar strength, line positions and intensities behave in a nontrivial manner. A straightforward analysis by read-out may also be impeded by high spectral noise levels and by very broad or strongly overlapping lines. Thus, for many cw ESR spectra, a full-scale quantum-theoretical numerical simulation, possibly combined with least-squares fitting, is necessary to reproduce the spectrum and to recover the underlying structural and dynamic parameters. Spectral simulation is therefore an important ingredient of the successful application of ESR spectroscopy.

In EPR spectroscopy (including ENDOR and pulse EPR), the extraction of information on structure and dynamics from experimental data heavily relies on computerized data processing, numerical spectral simulations and iterative parameter fittings. Numerical simulations of EPR spectra are usually performed with three intentions: (1) systematic study of the dependencies of spectral features on the magnetic parameters, (2) predictions whether a new experiment will give new information, and (3) accurate parameter extraction from experimental spectra.

EasySpin¹⁶ is software package which able to simulate cw ESR spectra of most paramagnetic systems under a wide range of dynamic conditions. EasySpin is a collection of functions and programs intended to run on Matlab, a commercial software platform for technical and scientific computation and visualization, available for several operating systems (Windows, Linux, and others). It is based on MATLAB (The MathWorks, Natick, MA, USA), a commercial programmable numerical and visualization software environment, for the following reasons: The programming language of MATLAB is based on matrices and very efficient matrix algorithms, thus relieving the spectroscopist of the implementation of these basic numerical types and procedures. Matlab has a simple syntax, and any new experimental idea can be coded and evaluated very quickly with a few additional EPR-specific functions. Visualization capabilities are extensive and very flexible.

2.2.4 Dielectric and ferroelectric characterization techniques

2.2.4.1 Dielectric characterization¹⁷

The method adopted to measure the dielectric constant of a material is to measure the capacitance of a parallel plate capacitor containing the ferroelectric substance as dielectric using Impedance/gain phase analyser

(4192A, Agilent Technologies, Palo Alto, CA). The dielectric constant can be directly calculated using the equation 2.8.

$$\epsilon_r = \frac{C t}{A \epsilon_0} \quad (2.8)$$

where ‘C’ is the capacitance in farads, ‘t’ is the distance between the electrodes in meter, ‘ ϵ_0 ’ is the permittivity of the free space (8.85×10^{-12} F/m) and ‘A’ is the area of the electrode surface of material in m^2 . The relative dielectric constant and dielectric loss ($\tan \delta$) were measured at varying frequencies ranging from 1 kHz to 100 kHz using Agilent - 4192A Impedance/Gain phase analyzer. Temperature dependent measurements are done by attaching high precision furnace to impedance analyser as shown in Fig. 2.12.



Figure 2.12 Set-up for dielectric characterisation

2.2.4.2 Piezoelectric characterisation^{17,18}

According to the procedure given by IRE standards, the piezoelectric constants such as electromechanical coupling coefficient, mechanical quality factor etc are determined simply by measuring resonance and antiresonance frequencies. The frequency of minimum impedance is called resonance frequency (f_r) and frequency of maximum impedance is called anti-resonance frequencies (f_a). The resonance and antiresonance frequencies are measured using Impedance/gain phase analyser (4192A, Agilent Technologies, CA, USA) on poled specimens.

The electromechanical coupling coefficient, k_p is the ratio of electrical energy converted to mechanical energy to that of input electrical energy and vice-versa. k_p can be calculated using the formula as given in equation 2.9.

$$k_p = \sqrt{\frac{1}{p} \left(\frac{f_a^2 - f_r^2}{f_r^2} \right)} \quad (2.9)$$

where 'p' is dimensionless shape factor and has the value 0.79 in one dimensional resonance.

The mechanical quality factor, Q_m is the ratio of strain in phase with stress to strain out of phase with stress. Q_m is calculated from the determination of minimum impedance Z_{fr} at the fundamental resonance frequency and using the equation 2.10.

$$Q_m = \frac{f_a^2}{\{2f_r Z_{fr} C(f_a^2 - f_r^2)\}} \quad (2.10)$$

The piezoelectric constants relating the mechanical strain produced by an applied electric field are termed the strain coefficients or the d coefficients. Conversely the coefficient d may be viewed as relating the charge collected on

the electrodes, to the applied mechanical stress and is known as charge output coefficients.

$$d_{ij} (C/N) = \frac{\text{Charge density}(C/m^2)}{\text{applied mechanical stress}(N/m^2)} \quad (2.11)$$

The term d_{33} applies when the force is in the 3 direction (along the polarisation axis) and is impressed on the same surface on which the charge is collected. The d_{33} constant was measured by applying a known force to the electroded surfaces of the specimen and measuring the electrical charge generated in the same direction using d_{33} meter (Piezometer System, Piezotest 300).

2.2.4.3 P-E and S-E loop measurements

All the ferroelectric material will have its own characteristic hysteresis loops and is known as the fingerprint of that material. Hysteresis loops are of two types, Polarisation- Electric field and Strain-Electric field from which spontaneous polarisation (\mathbf{P}_S), remnant polarisation (\mathbf{P}_R), and coercive field (\mathbf{E}_C) and Strain can be determined. The polarisation is a measure of degree of ferroelectricity. Polarisation \mathbf{P} , may be defined as

$$P = \frac{Q}{A} \quad (2.12)$$

where Q is the charge developed on the plates (Coulombs) and A is the area (m^2) of the plates. The most often quoted method of hysteresis loop measurement is based on a paper by Sawyer and Tower. In this experiment, the voltage is cycled by the signal generator. Its direction is reversed at high frequency, and the voltage across the reference capacitor is measured. The charge on the ferroelectric can be found by:

$$Q = CxV \quad (2.13)$$

where ‘ C ’ is the capacitance of the reference capacitor, and ‘ V ’ is the voltage measured over this capacitor. We can therefore represent the polarisation of a material in an oscillating electric field, by plotting the voltage applied to the material on the x-axis of the oscilloscope, and the surface charge on the y-axis. It is only possible to measure the polarisation through cycling the voltage across the ferroelectric ceramic. One cannot measure absolute values instantaneously, but can deduce absolute values from the changes measured when cycling the polarisation. The samples displacement is simultaneously measured with a laser interferometer system.

The ferroelectric polarisation and strain measurements are carried out using piezoelectric evaluation system (Model TF Analyser 2000, aixACCT, Germany)

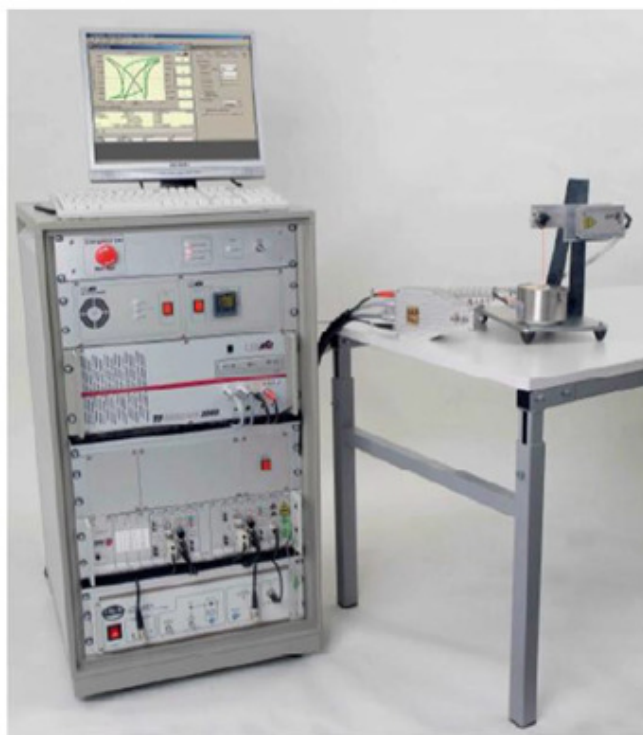


Figure 2.13 Piezo evaluation system

References

- [1] P. V. Divya and V. Kumar, "Crystallization studies and properties of $(\text{Ba}_{1-x}\text{Sr}_x)\text{TiO}_3$ in borosilicate glass", *J. Am. Ceram. Soc.*, 90 (2007) 472-476.
- [2] Y. Takahashi, Y. Matsuoka, K. Yamaguchi, M. Matsuki, and K. Kobayashi, "Dip coating of PT, PZ and PZT films using an alkoxide-diethanolamine method", *J. Mater. Sci.*, 25 (1990) 3960-3964.
- [3] D. Liu, H. Zhang, W. Cai, X. Wu, and L. Zhao, "Materials science communication synthesis of PZT nanocrystalline powder by a modified sol-gel process using zirconium oxynitrate as zirconium source", *Mater. Chem. Phys.*, 51 (1997) 186-189.
- [4] G. Yi, Z. Wu, and M. Sayer, "Preparation of $\text{Pb}(\text{Zr,Ti})\text{O}_3$ thin films by sol gel processing: electrical, optical, and electro-optic properties", *J. Appl. Phys.*, 64 (1988) 2717-2724.
- [5] H. Hirashima, E. Onishi, and M. Nakagawa, "Preparation of PZT powders from metal alkoxides", *J. Non-Cryst. Solids*, 121 (1990) 404-406.
- [6] Wu, M. Isabel, M. Salvado, P. M. Vilarinho and J. L. Baptista, "Lead zirconate titanate prepared from different zirconium and titanium precursors by sol-gel", *J. Am. Ceram. Soc.*, 81 (1998) 2640-2644.
- [7] R. Zimmermann and S. Auer, "Spray drying of sol-gel precursors for the manufacturing of PZT powders", *J. Sol-Gel Sci. Technol.*, 3 (1994) 101-107.

- [8] V. Kumar, Y. Ohya and Y. Takahashi, "Sol-gel processing of ferroelectric PbTiO_3 and $\text{Pb}(\text{Zr}_{0.5}\text{Ti}_{0.5})\text{O}_3$ thin films", *Jpn. J. Appl. Phys.*, 37 (1998) 4477-4481.
- [9] J. H. Choy, Y. S. Han and J.T. Kim, "Hydroxide co-precipitation route to the piezoelectric oxide $\text{Pb}(\text{Zr,Ti})\text{O}_3$ (PZT)", *J. Mater. Chem.*, 5 (1995) 65-69.
- [10] R. Balachandran and T. R. N. Kutty, "Formation of $\text{Pb}(\text{Ti,Zr})\text{O}_3$, from thermal decomposition of oxalate precursors", *Mater. Chem. Phys.*, 10 (1984) 287-298.
- [11] T. R. N. Kutty and R. Balachandran, "Direct precipitation of lead zirconate titanate by the hydrothermal method", *Mater. Res. Bull.*, 19 (1984) 1479-1488.
- [12] B. D. Cullity, "Elements of X-ray diffraction", Addison-Wesley Publishing Company, London (1978).
- [13] B. H. Toby "A graphical user interface for GSAS," *J. Appl. Cryst.*, 34 (2001) 210-213.
- [14] S. J. Sandoval, "Micro-Raman spectroscopy: a powerful technique for materials research", *Microelectronics* 31 (2000) 419-427.
- [15] R. S. Drago, "Physical methods in inorganic chemistry", Reinhold Publishing Corp., New York (1965).
- [16] S. Stoll and A. Schweiger, "EasySpin, a comprehensive software package for spectral simulation and analysis in EPR", *J. Magn. Reson.*, 178 (2006) 42-55.
- [17] B. Jaffe, W. R. Cook and H. Jaffe, "Piezoelectric ceramics", Academic Press (1971).

- [18] H. Jaffe, D. Berlincourt, T. Kinsley, T. M. Lambert, D. Schwarts, E. A. Gerber and I. E. Fair, "IRE standards on piezoelectric crystals: measurements of piezoelectric ceramics", Proc. IRE, 49 (1961) 1161-1169.

Ferroelectric Aging in Hybrid-Doped PZT

Contents

- 3.1 Introduction
- 3.2 Experimental Procedure
- 3.3 Results and Discussion
- References

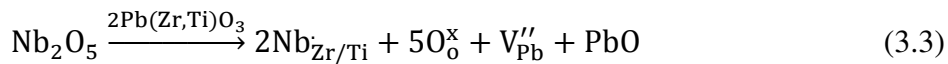
Aging effect in manganese (Mn) and niobium (Nb) hybrid-doped PZT composition has been reported. Interestingly, it is observed that the ferroelectric aging depends on the acceptor: donor ratio. In hybrid-doped PZT, at high donor dopant concentrations, aging is not observed. The underlying mechanism is correlated with the defect chemistry of the system. It is also observed that tuning the defect chemistry is an effective strategy to realize piezoceramics with enhanced dielectric and piezoelectric characteristics.

Some of the contents of this chapter have appeared in the following research publication.

A. Anil, K. Vani and V. Kumar, *Applied Physics A*, 122 (2016) 1-5.

3.1 Introduction

Lead zirconate titanate (PZT) ceramics are widely used in the field of piezoelectric sensors, actuators and transducers due to its excellent electromechanical characteristics. ‘*Hardening*’ and ‘*softening*’ of PZT by aliovalent doping is used as appropriate technique to tailor the piezoelectric properties. PZT can be ‘*softened*’ if it is doped with donor-type dopants (higher-valence) and can be ‘*hardened*’ by acceptor-type dopants (lower-valence). Modification in piezoelectric properties of Lead Zirconium Titanium oxide [PZT] by aliovalent doping is associated with the presence of point defects in the lattice. The type of point defect formed depends on the nature of the impurity and the substitution site ^{1,2}. In softening by B-site donor doping, charge compensation is achieved by formation of electrons or lead vacancies (V''_{Pb}) while in hardening by acceptor doping it is through creation of oxygen vacancies ($V_{\ddot{O}}$) as given below in equations 3.1 - 3.3¹.



where Mn'_{Ti} is a negatively charged Mn on the Ti-site, $V_{\ddot{O}}$ is doubly positively charged oxygen vacancy with respect to neutral lattice, $O^x_{\ddot{O}}$ is the neutral oxygen in the lattice, Nb_{Ti} is positively charged Nb on the Ti-site and V''_{Pb} is the doubly ionized lead vacancy. These charged point defects formed micro dipoles and interact with the spontaneous polarisation leading to stabilization of domain structure. Stabilization of domain configuration changes the ferroelectric properties and influences switching of ferroelectric domains with time. In ferroelectrics, the change of ferroelectric, dielectric and piezoelectric properties

with time is referred to as ferroelectric aging. In ferroelectrics, aging affects their stability and therefore their reliability for device applications. It usually manifests itself in large signal properties as the appearance of constricted or double polarisation-electric field (P-E) hysteresis loop in unpoled state as shown in Fig.3.1 and in small signal properties such as piezoelectric constant, dielectric constant etc. as a gradual decrease in values with time.

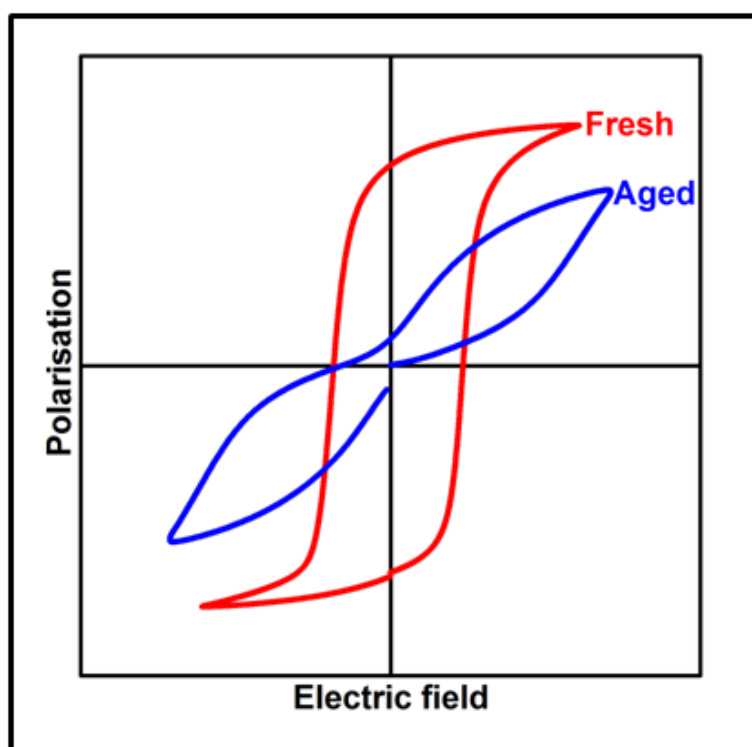


Figure 3.1 Ferroelectric hysteresis showing constriction on aging

Aging effect is vastly different between acceptor-doped ferroelectrics and donor-doped ferroelectrics. The aging effect in acceptor-doped ferroelectrics is ascribed to the migration of oxygen vacancies. Recent studies have shown that, in acceptor-doped ferroelectric oxides like BaTiO_3 , migration of point defects such as \bar{V}_O influence the switching of ferroelectric domains through a Symmetry Conforming-Short Range Ordering (SC-SRO)

mechanism^{3,4}. However in donor-doped ferroelectric oxides, such an effect does not exist since cation vacancies, generated in such cases, are immobile^{5,6}. Interestingly, in donor-acceptor co-doped BaTiO₃, the SC-SRO mechanism has been reported even when the concentration of donor dopant exceeds that of the acceptor⁷. In PZT, which is intrinsically p-type due to the presence of lead vacancies, V''_{Pb} on hybrid-doping it is still an open question whether such a mechanism operates. In order to answer this question, it is necessary to study the dielectric, ferroelectric and piezoelectric properties of hybrid (Mn, Nb) doped PZT and correlate the observed effects with its defect chemistry. This will provide clear insights for tailoring PZT-based systems for enhanced electromechanical properties and with reduced aging effects. Currently hybrid (donor+acceptor) doped PZT attract major attention in order to explore exciting possibilities in the field of actuators and transducers^{2,8,9}. However there is no systematic study on aging effect in hybrid-doped PZT. It is important to have a better understanding of the aging behaviour to improve the reliability of ferroelectric devices.

3.2 Experimental Procedure

Compositions having the general formula $(Pb_{0.94(1-x/2)}Sr_{0.06})(Zr_{0.53}Ti_{0.47})_{[(1-x)0.99625]}Mn_{0.005}Nb_xO_3$ denoted hereafter as PSZTMn_{0.005}Nb_xO₃ where $x=0, 0.002, 0.004, 0.008, 0.010, 0.015$; were prepared by conventional solid state powder method from starting materials like PbO(Qualigens, India), SrCO₃(Fisher Scientific, India), ZrO₂(Sigma Aldrich, UK), TiO₂(Merck, Germany), Nb₂O₅(Sigma Aldrich, China) and Mn₂O₃(Sigma Aldrich, USA). The metal oxides were taken in stoichiometric ratio according to the formula and mixed well by ball milling using distilled water as solvent, dried and calcined at 850⁰C for two hours. The calcined powder were made into 10 mm pellets by adding PVA as binder followed by hydrostatic pressing at a pressure

of 200MPa. The specimens were sintered at 1270⁰C for 2 hours under PbO atmosphere. Crystalline phase of sintered samples were identified with X-ray diffractometre (XRD, Model-D5005 Bruker Germany) using CuK α radiation. Sintered pellets were polished and electroded with silver paste followed by curing at 700⁰C for 15 minutes. In silicone oil bath specimens were poled by applying 3 kVmm⁻¹ at 100⁰C. Dielectric and piezoelectric properties were measured 48 h after poling. Dielectric properties of the sintered compacts were determined at 1 kHz using an impedance analyzer (Model 4192A, Agilent Technologies, Palo Alto, CA). Electro mechanical coupling factor (k_p) and mechanical quality factor (Q_m) was calculated from resonance measurements. The piezoelectric coefficient, d_{33} was measured by using d_{33} meter (Piezometer System, Piezotest 300). Ferroelectric hysteresis (P–E) of samples was measured using a Ferroelectric Tester (Precision Workstation, Radiant Technologies Inc, USA). For aging, samples were kept for 60 days at room temperature. Electron Paramagnetic Resonance spectroscopy of aged specimens were carried out using an EPR spectrometer (Model-JES FA200, JEOL, Japan) at room temperature in the X band frequency of 9.1 GHz.

3.3 Results and Discussion

XRD patterns shown in Fig. 3.2 reveal that all the compositions crystallise in the tetragonal structure as revealed by the split (002), (200) peaks at $2\theta \approx 45^0$. No secondary phase was observed in any of the compositions revealing their phase purity.

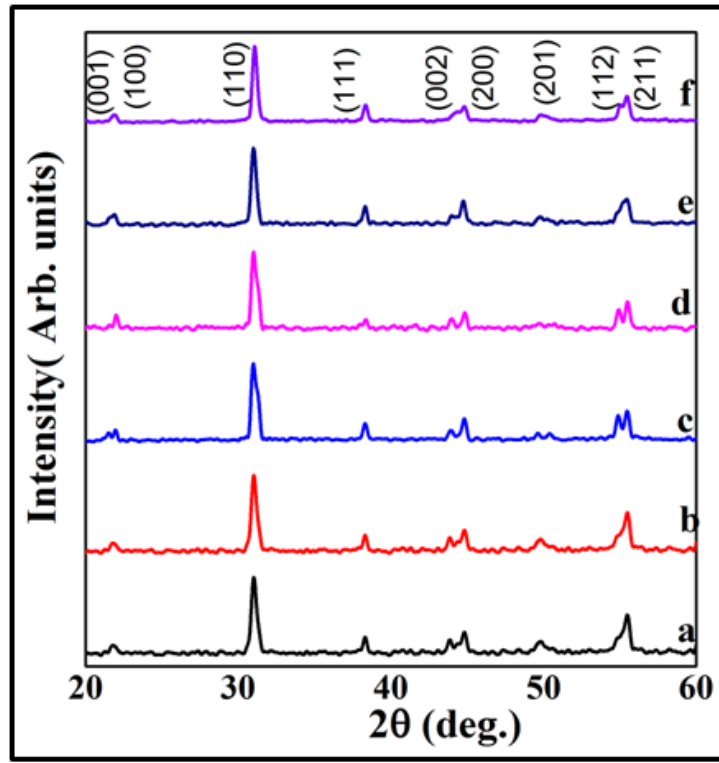


Figure 3.2 XRD patterns of $\text{PSZTMn}_{0.005}\text{Nb}_x\text{O}_3$; $x =$ (a) 0, (b) 0.002, (c) 0.004, (d) 0.008, (e) 0.010, (f) 0.015

3.3.1 Ferroelectric Aging

Ferroelectric hysteresis loops of unaged and aged samples of varying niobium concentrations are shown in Fig. 3.3. All the unaged samples show a normal hysteresis loop. But after aging, there is a remarkable difference in the nature of P-E loops with different niobium concentrations. In only acceptor-dominant samples ($x \leq 0.004$), there is a constriction in the P-E loop [Fig. 3.3(a)-(c)] after aging. For further increase in the donor concentration, ($x > 0.004$), the hysteresis loop becomes normal [Fig. 3.3(d)-(f)]. This is in sharp contrast to that observed in Mn- and Nb- hybrid-doped BaTiO_3 ⁷, where aging occurs in both acceptor-dominant and donor-dominant compositions due to the SC-SRO mechanism.

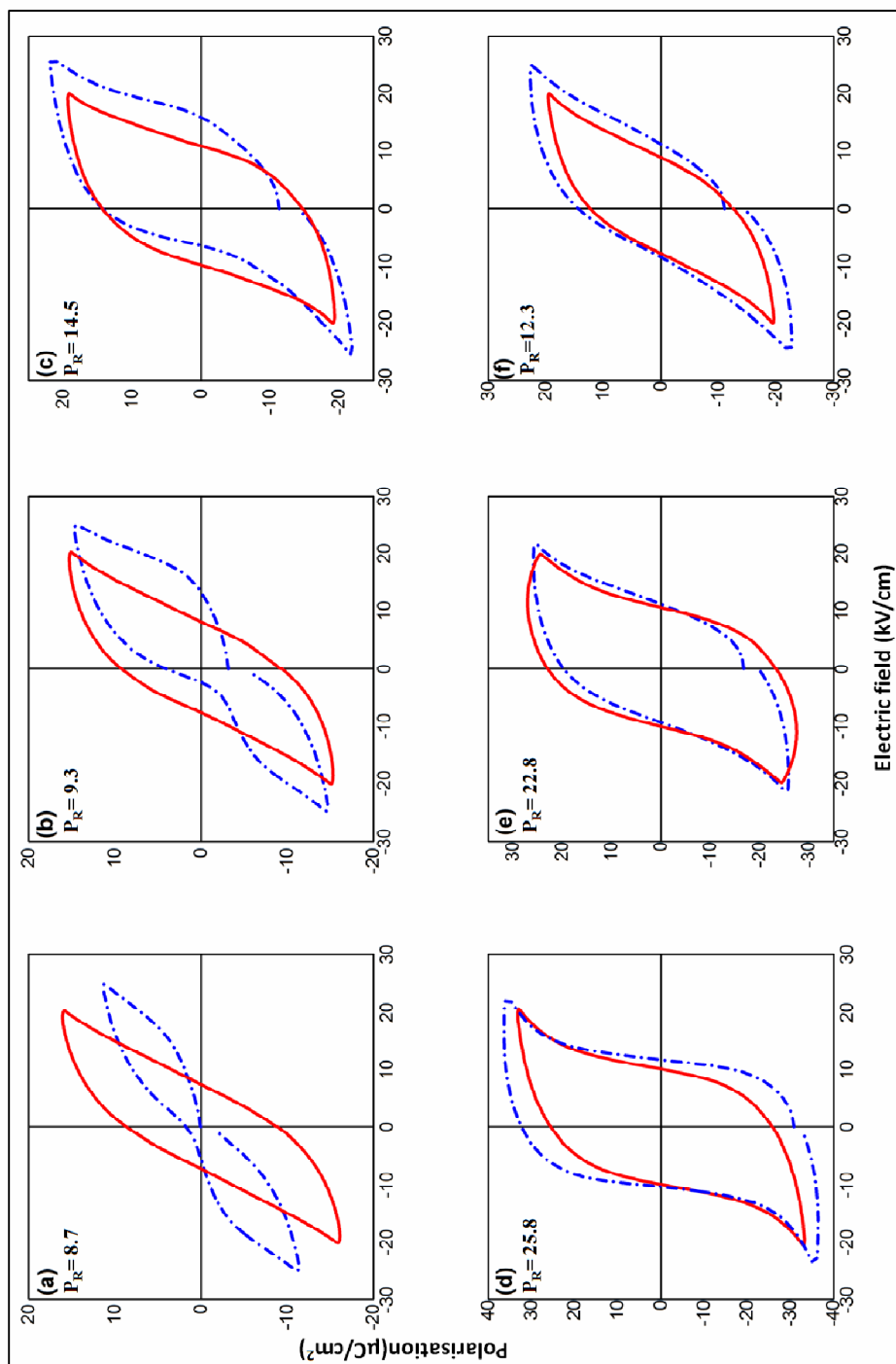


Figure 3.3 P-E loops of unaged (solid line) and aged (dotted line) samples of PSZTMn_{0.005}Nb_xO₃; x= (a)0, (b)0.002, (c)0.004, (d)0.008, (e) 0.010, (f) 0.015.

In order to better understand the defect chemistry and study the underlying aging mechanism in PZT, Electron Paramagnetic Resonance (EPR) spectroscopy was carried out since it is a sensitive spectroscopic tool to probe electronic and structural features associated with the dopants. For the theoretical confirmation of observed spectra, the EPR spectra were also simulated using the *EasySpin4.0.0*¹⁰ program using spin - Hamiltonian parameters given in Table 3.1. where g_{eff} , a_{iso} and D represent effective spectroscopic splitting factor, isotropic hyperfine coupling constant and zero field splitting parameter respectively. In the simulated spectra, hyperfine interactions with Mn-nucleus, $I = \frac{5}{2}$ is also taken into consideration.

Table 3.1 Spin-Hamiltonian parameters

Oxidation state	g_{eff}	a_{iso} [MHz]	D [cm^{-1}]
Mn ⁴⁺ (D1)	4.300	230	0.600
Mn ²⁺ (D2)	2.004	250	0.016
Mn ⁴⁺ (D3)	3.300	230	0.100

In B-site Mn³⁺ doped PZT, oxygen vacancies are created in order to maintain charge neutrality as represented in equation 3.1. The mechanism can be explained as follows.

(i) when $x=0$, the negatively charged Mn_{Ti}' forms defect dipoles of the type [Mn_{Ti}' - V_O]. Since Mn³⁺ is EPR silent at the X-band frequency (where the zero field splitting is larger than the microwave frequency, ≈ 9.2 GHz) there are no signals corresponding to it in the EPR spectra. EPR signal corresponding to a g value of 4.3 (denoted as **DI** in [Fig. 3.4(a)i]) corresponds to Mn⁴⁺ center¹¹ which is confirmed from the simulated EPR spectra [Fig. 3.4(a)ii] using spin-Hamiltonian parameters corresponding to Mn⁴⁺ ($S = \frac{3}{2}$) given in Table 3.1.

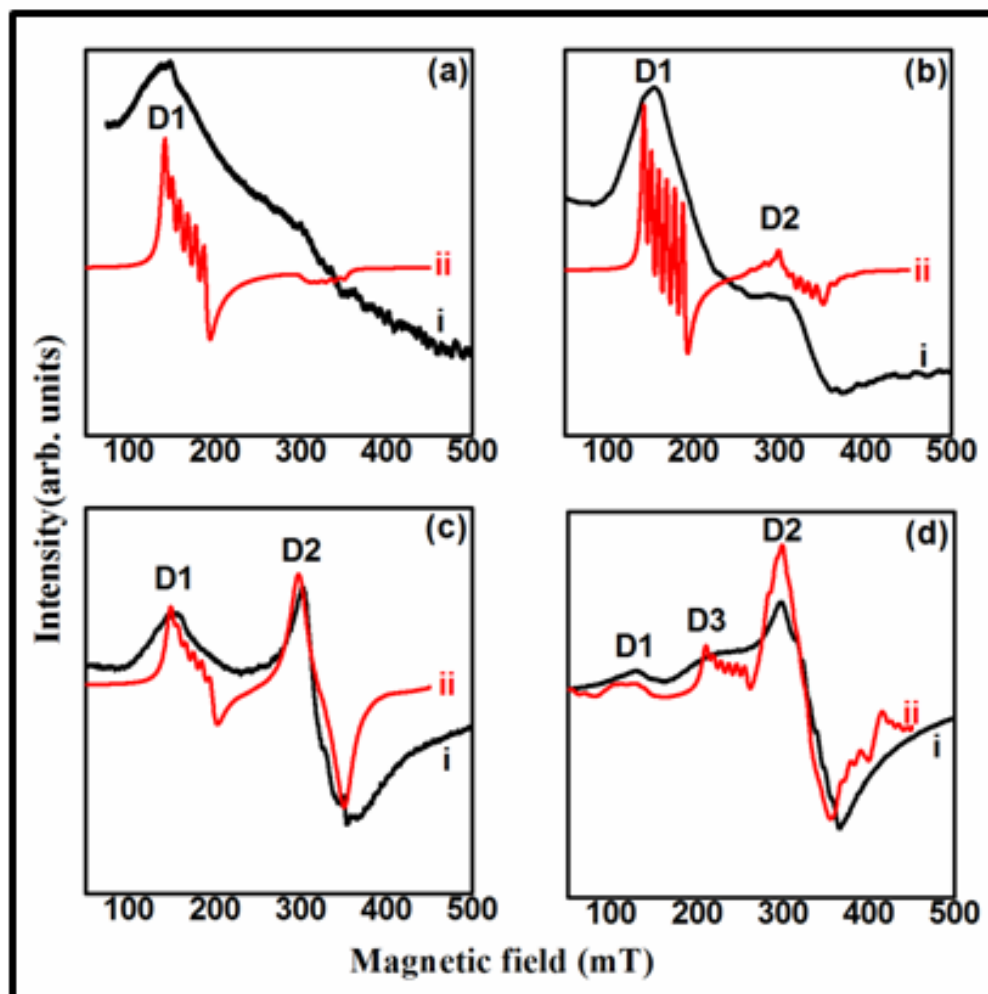


Figure 3.4 Observed (i) and Simulated (ii) EPR spectra of $\text{PSZTMn}_{0.005}\text{Nb}_x\text{O}_3$; $x =$ (a) 0, (b) 0.002, (c) 0.004, (d) 0.010

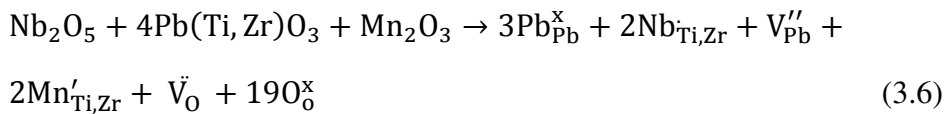
It is reasonable to assume the existence of Mn_{Ti}^x , Mn'_{Ti} and Mn''_{Ti} due to the facile disproportionation reaction of Mn^{3+} to Mn^{2+} and Mn^{4+} valence states^{12,13}. Defect dipoles such as $[Mn'_{Ti} - \ddot{V}_O]$ and $[Mn''_{Ti} - \ddot{V}_O]$ undergo Symmetry Conforming-Short Range Ordering (SC-SRO) after aging, attain the symmetry of the crystal lattice and reorient the switched ferroelectric polarisation leading to constriction in the P-E loop as shown in Fig. 3.3(a).

(ii) for lower concentrations of niobium $0 < x \leq 0.004$, free electrons are added to the system as represented in equation 3.2. These free electrons in the lattice get trapped at manganese sites¹³ reducing them as represented below



The emergence of a peak **D2** at $g = 2.1$ [Fig. 3.4(b)i] corresponds to the $[Mn''_{Ti} - \ddot{V}_O]$ defect dipole¹⁴ as confirmed from the simulated EPR spectra [Fig. 3.4(b)ii] using spin-Hamiltonian parameters corresponding to Mn^{2+} ($S = \frac{5}{2}$) given in Table 3.1. At a niobium concentration of $x = 0.004$, intensity of EPR signal **D2** is relatively larger than that of **D1** [Fig. 3.4(c)i] further confirming the generation of more Mn^{2+} ions as represented by equation 3.5. The restoring force of defect dipoles $[Mn'_{Ti} - \ddot{V}_O]$ and $[Mn''_{Ti} - \ddot{V}_O]$ on the ferroelectric polarisation lead to constriction in P-E loop [Figs. 3.3(b) & (c)].

(iii) for higher concentrations of niobium $x \geq 0.008$, the charge compensation is achieved by formation of doubly ionized lead vacancies as represented below;



There is an additional centre denoted as **D3** appearing in EPR spectra [Fig. 3.4(d) i] for $x=0.010$. We assign this additional peak to Mn^{4+} centre with a lower axial crystal field and confirmed by simulation of EPR spectra [Fig. 3.4(d) ii] using spin-Hamiltonian parameters corresponding to Mn^{4+} ($S = \frac{5}{2}$) with lower zero field splitting parameter, D (0.100cm^{-1}) as given in Table 3.1. In perovskites having tetragonal crystal structure, Mn^{4+} dopant has been reported¹¹ to occupy exactly the off-centre site occupied by Ti^{4+} . The impact of the large Zero Field Splitting (ZFS), as a result of this axial crystal field, is schematically illustrated in Fig. 3.5(a). At higher Nb^{5+} -concentrations, due to formation of lead vacancies (V_{Pb}''), strong coulombic interactions of the type $[V_{\text{Pb}}'' - \ddot{V}_{\text{O}}]^{15,16}$ resulted as shown in Fig. 3.5(c). This type of vacancy pair weakens the axial crystal field in the lattice and leads to lowering of ZFS. The resulting lower ZFS is schematically represented in Fig. 3.5(b). As a result of reduced ZFS, additional transitions with $\Delta m_s = \pm 2$ ¹⁷ which are spin forbidden is possible, as shown in Fig. 3.5(b), giving rise to the signal **D3** in the EPR spectrum. The vacancy pair $[V_{\text{Pb}}'' - \ddot{V}_{\text{O}}]$ also decreases the mobility of oxygen vacancies. Due to these factors, in donor-dominant compositions, aging is absent and hence P-E loop is normal [Figs. 3.3(d)-(f)].

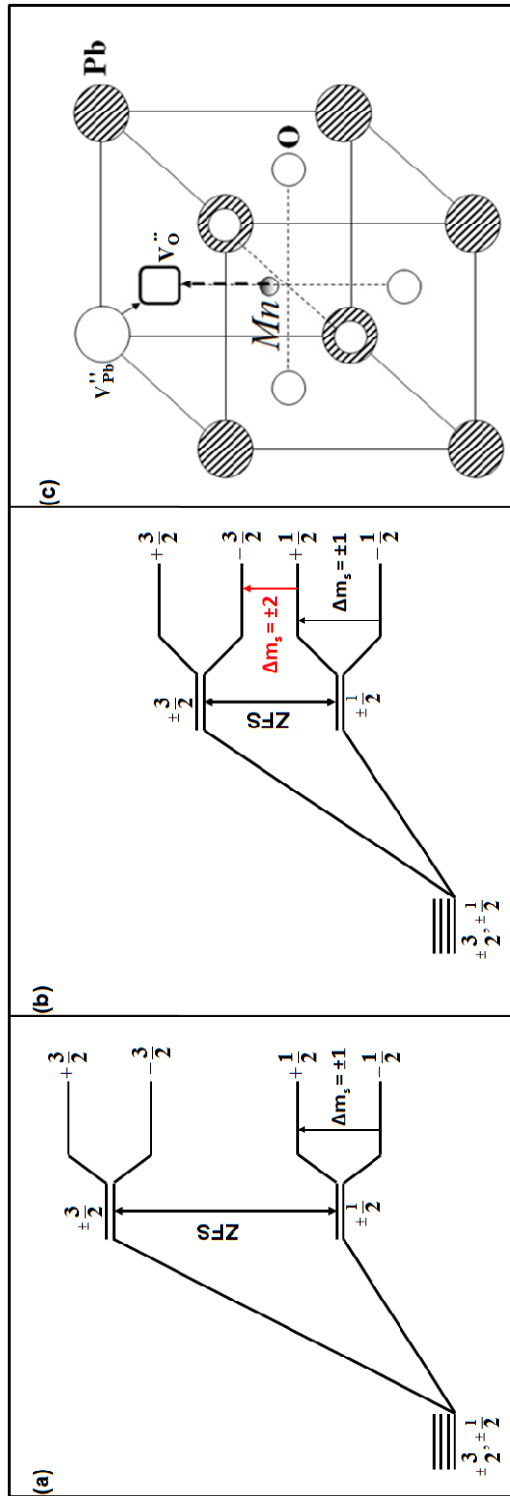


Fig. 3. 5 Splitting of energy levels in Mn^{4+} in the presence of (a) Higher Zero field splitting and (b) Lower Zero field splitting. [ZFS(a) \gg ZFS (b)] (c) Representative defect structure in B-site Mn-doped PZT

3.3.2 Ferroelectric properties

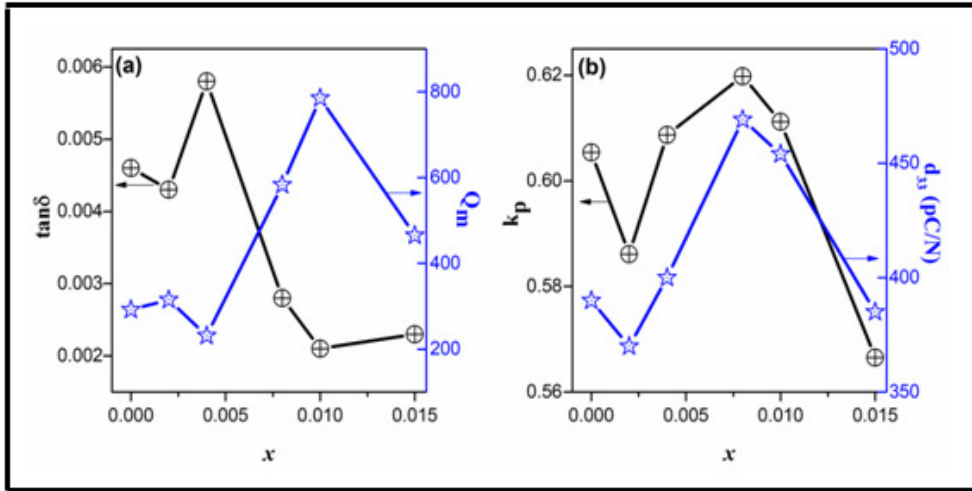


Figure 3.6 Dielectric and Piezoelectric properties of PSZTMn_{0.005}Nb _{x} O₃

Fig. 3.6 shows the changes in the dielectric and piezoelectric characteristics of the hybrid-doped systems. When $x = 0.002$, decrease in the dielectric and piezoelectric properties is attributed to increase in the tetragonality (increase in c/a ratio from 1.019 to 1.021). For the composition having $x = 0.004$, increase in $\tan\delta$ [Fig. 3.6(a)] is attributed to oxygen vacancy (\vec{V}_O) migration. Increase in d_{33} and k_p [Fig. 3.6(b)] in this case is attributed to the increased switching of ferroelectric polarisation as revealed by increase in remnant polarisation, \mathbf{P}_R as given Fig. 3.3. This is due to the decrease in the pinning of ferroelectric polarisation by $[\text{Mn}_{\text{Ti}}'' - \vec{V}_O]$ dipole when compared to that of $[\text{Mn}'_{\text{Ti}} - \vec{V}_O]$ dipole. For compositions in the range, $0.004 < x < 0.01$ enhancement in k_p and d_{33} [Fig. 3.6(b)] is attributed to the increase in domain wall mobility due to the presence of extrinsic lead vacancies (V_{Pb}'')^{8,9,18} whereas the sharp decrease in $\tan\delta$ with concomitant increase in Q_m [Fig. 3.6(a)] is due to reduction in \vec{V}_O migration. For compositions having $x \geq$

0.010 decrease in d_{33} and k_p [Fig. 3.6(b)] is attributed to decrease in A-O-B coupling as a result of more lead vacancies as represented in equation 3.6. This is also confirmed from the reduction in \mathbf{P}_R value as given Fig. 3.3. The hybrid-doped composition having 'x' = 0.008, exhibit excellent dielectric and piezoelectric characteristics with $\tan\delta = 0.003$, $Q_m = 583$, $k_p = 0.62$ and $d_{33} = 469$ pC/N suitable for actuator applications.

3.4 Conclusion

We have shown that ferroelectric aging during hybrid-doping of aliovalent dopants at B-site of PZT is related to the acceptor:donor ratio. In acceptor- dominant compositions aging is observed whereas in donor-dominant compositions significant resistance to aging is observed. This is in contrast to the 'aging' observed in non-lead containing compositions like barium titanate, irrespective of the donor:acceptor ratio. In order to understand this difference, a thorough EPR study of the defect chemistry was undertaken. By combining the results obtained from the dielectric and piezoelectric studies in these hybrid-doped compositions, the mechanism responsible for aging-resistance at high levels of donor dopant concentrations have been comprehensively established. These results also demonstrate that at appropriate donor:acceptor ratio, piezoceramics with enhanced dielectric and piezoelectric characteristics can be realised.

References

- [1] B. Jaffe, W. R. Cook and H. Jaffe, “Piezoelectric Ceramics”, Academic Press (1971).
- [2] D. Damjanovic, “Ferroelectric, dielectric and piezoelectric properties of ferroelectric thin films and ceramics”, *Rep. Prog. Phys.*, 61 (1998) 1267-1323.
- [3] X. Ren, “Large electric-field-induced strain in ferroelectric crystals by point-defect mediated reversible domain switching”, *Nat. Mater.*, 3 (2004) 91-94.
- [4] L. Zhang and X. Ren, “Aging behavior in single-domain Mn-doped BaTiO₃ crystals: implication for a unified microscopic explanation of ferroelectric aging”, *Phys. Rev. B*, 73 (2006) 094121-1-6.
- [5] H. Bao, L. Zhang, Y. Wang, W. Liu, C. Zhou and X. Ren, “Contrasting aging behavior of as-grown and annealed BaTiO₃ single crystals grown by KF-flux technique”, *Appl. Phys. Lett.*, 91 (2007) 142903-1-3.
- [6] H. Bao, J. Gao, D. Xue, C. Zhou, L. Zhang, W. Liu and X. Ren, “Control of ferroelectric aging by manipulating point defects”, *Ferroelectrics*, 401 (2010) 45-50.
- [7] W. Liu, W. Chen, L. Yang, L. Zhang, Y. Wang, C. Zhou, S. Li and X. Ren, “Ferroelectric aging effect in hybrid-doped BaTiO₃ ceramics and the associated large recoverable electrostrain”, *Appl. Phys. Lett.*, 89 (2006) 172908-1-3.

- [8] J. H. Park, B. K. Kim, K. H. Song and S. J. Park, "Piezoelectric properties of Nb₂O₅-doped and MnO₂-Nb₂O₅ co-doped Pb(Zr_{0.53}Ti_{0.47})O₃ ceramics", *J. Mater. Sci: Mater. Electron.*, 6 (1995) 97-101.
- [9] E. Boucher, B. Guiffard, L. Lebrun and P. Guyomar, "Influence of the niobium or fluorine dopant concentration on the properties of Mn-Doped lead zirconate titanate ceramics", *Jpn.J. App. Phys.*, 43 (2004) 5378-5383.
- [10] S. Stoll and A. Schweiger, "EasySpin, a comprehensive software package for spectral simulation and analysis in EPR", *J. Magn. Reson.*, 178 (2006) 42-55.
- [11] K. A. Muller, W. Berlinger, K.W. Blazey and J. Albers, "Electron paramagnetic resonance of Mn⁴⁺ in BaTiO₃", *Solid State Commun.* 61 (1987) 21-25.
- [12] K. Vani and V. Kumar, "Influence of defect mobility on electrostrain in acceptor-doped Ba_{0.80}Sr_{0.20}TiO₃", *AIP Advances*, 2 (2012) 042177-1-4.
- [13] R. A. Eichel, "Characterization of defect structure in acceptor-modified piezoelectric ceramics by multifrequency and multipulse electron paramagnetic resonance spectroscopy", *J. Am. Ceram. Soc.*, 91 (2008) 691-701.
- [14] B. Milsch, "Evaluation of lattice site and valence of manganese in polycrystalline BaTiO₃, and n- BaTiO₃, by electron paramagnetic resonance", *Phys. Stat. Sol. (a)*, 133 (1992) 455-464.

- [15] D. J. Keeble, B. Nielsen, A. Krishnan, K. G. Lynn, S. Madhukar, R. Ramesh and C.F.Young, “Vacancy defects in (Pb, La) (Zr, Ti)O₃ capacitors observed by positron annihilation”, *Appl. Phys. Lett.*, 73 (1998) 318-320.
- [16] G.H. Dai, P.W.Lu, X.Y.Huang, Q.S.Liu and W.R.Xue, “A study of Pb vacancies and Pb-O vacancy pairs in doped Pb_{0.85}Sr_{0.15} (Zr_{0.55}Ti_{0.45})O₃ ceramics by positron annihilation”, *J. Mater. Sci: Mater. Electron.*, 2 (1991) 164-170.
- [17] E. Erdem, M. Drahus, R. A. Eichel, A. Ozarowski, J. V. Tol and L. C. Brunel, “ Microstructural characterisation of the manganese functional center site in PbTiO₃ ferroelectrics-multifrequency electron paramagnetic resonance and Newman superposition model analysis”, *Ferroelectrics*, 363 (2008) 39-49.
- [18] R Gerson, “Variation in ferroelectric characteristics of lead zirconate titanate ceramics due to minor chemical modifications”, *J. Appl. Phys.*, 31 (1960) 188-194.

Local Structural Rearrangements and Evolution of Relaxor states in Complex Perovskite Systems

- Contents
- 4.1 Introduction
 - 4.2 Experimental Procedure
 - 4.3 Results and Discussion
 - 4.4 Conclusion
 - References

Local structural rearrangements in lead-based complex perovskites of the type $(\text{Ba}_{1-x}\text{Pb}_x)(\text{In}_{0.50}\text{Nb}_{0.50})\text{O}_3$ responsible for transition from ferroelectric to relaxor are examined by careful analysis of their Raman spectra. Subtle changes in the bonding brought about by the differences in the chemical nature of A- and B-site cations have been correlated with the dynamic A-O-B coupling. Deviations of the local structure as a result of such bonding preferences have been confirmed by studying the changes in the Raman spectra when Nb^{5+} is substituted by Sn^{4+} as the third B-site cation.

Some of the contents of this chapter have appeared in the following research publication.

Adukkadan Anil and Viswanathan Kumar, *Journal of the American Ceramic Society*, 99 (2016) 3980-3984.

4.1 Introduction

Relaxor (R) ferroelectrics of lead-based complex perovskites having the general formula $\text{Pb}(\text{B}'\text{B}'')\text{O}_3$ where B' and B'' are cations of unlike valence and size, have attracted interest for transducer applications in view of their excellent piezoelectric properties and lower sintering temperature enabling the use of cheaper metal electrodes for process compatibility during fabrication of multilayer actuators^{1,2}. It is established that the relaxor behavior of lead-based complex perovskites is related to its B-site ordering.

For example, in $\text{Pb}(\text{In}_{0.50}\text{Nb}_{0.50})\text{O}_3$ [PIN]³ completely disordered B-site arrangement shows relaxor behaviour while completely ordered state shows antiferroelectric character and the partially ordered PIN shows broad dielectric response without dispersion as shown in Fig.4.1(a). In $\text{Pb}(\text{Sc}_{0.50}\text{Ta}_{0.50})\text{O}_3$ [PST]⁴, completely disordered B-site arrangement shows relaxor behaviour while 1:1 ordered state shows antiferroelectric character as shown Fig. 4.1(b).

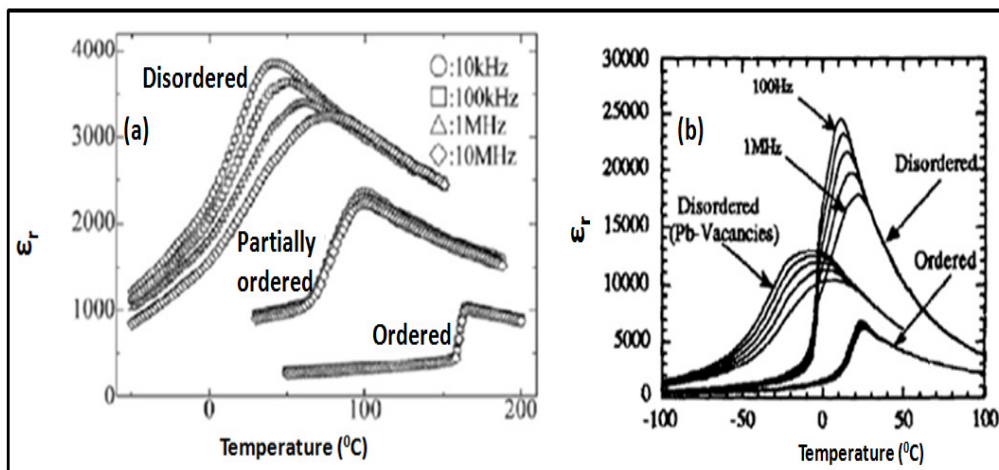


Figure 4.1 Temperature dependence of dielectric constant of (a) $\text{Pb}(\text{In}_{0.50}\text{Nb}_{0.50})\text{O}_3$

[Source: H. Ohwa et al, *J. Phys. Soc. Jpn.*, 69 (2000) 1533-1545]

(b) $\text{Pb}(\text{Sc}_{0.50}\text{Ta}_{0.50})\text{O}_3$

[Source: F. Chu et al, *J. Appl. Phys.*, 74(1993)5129-5134] at different frequencies.

But the situation is more complex in the case of complex perovskites of 1:2 stoichiometries like $\text{Pb}(\text{Mg}_{0.33}\text{Nb}_{0.66})\text{O}_3$ [PMN]. Superlattice reflections in selected area electron diffraction (SAED) patterns of PMN^{5-7} revealed the presence of 1:1 B-site ordered regions. The superlattice reflection peaks are due to the cell doubling of 1:1 ordered nanoregions with a space group $\text{Fm}\bar{3}\text{m}$. The 1:1 B-site ordering in PMN is inconsistent with its 1:2 stoichiometry. Two different models are proposed to explain the development of 1:1 ordering in PMN^5 , the space charge model and the random layer (random site) model. In the space-charge model, the B' and B'' -sub lattices are assumed to be occupied exclusively by the divalent Mg^{2+} and pentavalent Nb^{5+} cations, respectively. Accordingly, the ordered regions in PMN would have a local Mg/Nb ratio of 1:1 in contrast with the 1:2 stoichiometry at B-site. Thus, the doubled unit cell of $[\text{Pb}^{2+}(\text{Mg}_{1/2}^{2+}\text{Nb}_{1/2}^{5+})\text{O}^{2-}_3]^{-0.5}$ would carry a net negative charge. This charge imbalance leading to impede the growth of ordered domains. While in the random layer model, the 1:1 ordering can be represented by $\text{Pb}[(\text{Mg}_{2/3}\text{Nb}_{1/3})_{1/2}\text{Nb}_{1/2}]\text{O}_3$. Here B'' -sublattice is occupied exclusively by Nb^{5+} cations, whereas the B' sites are occupied by a mixture of Mg/Nb, thus the ordered regions are consistent with the 1:2 stoichiometry. In the PMN family, coarsening of ordered domain size to a micrometer scale observed for annealing at higher temperature which supports the random layer model^{8,9}. However, different models were proposed to explain the relaxor behavior in Lead-based complex perovskites¹⁰⁻¹⁵, still the origin of the relaxor behavior is under debate. It is proposed that structural origin of relaxor characteristics in lead-based complex perovskites have been related to B-site ordering as well as the rearrangements in the lattice due to the off-center displacement of lead atoms. Origin of this off-center displacement of Pb^{2+} ions is attributed to presence of its ns^2 lone pair of electrons^{16,17}.

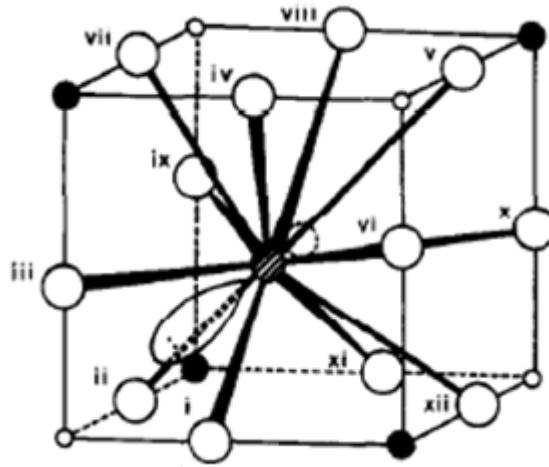


Figure 4.2 One octant of unit cell of the Perovskite

Consider one octant of the cubic unit cell as shown in Fig. 4.2. For Pb^{2+} co-ordinated to 12 oxygen atoms, there exist two crystallographic directions, [100] and [111], along which the lone-pair of electrons can be directed, being mainly repulsed by four or three Pb-O bonds, respectively. The repulsion is lower for the second direction, which is thus adopted by the lone-pair resulting in Pb^{2+} displacement along $\langle 111 \rangle$. The difference in sizes of B' and B'' -cations has intense role on Pb^{2+} displacement along $\langle 111 \rangle$. Displacement of Pb^{2+} along $\langle 111 \rangle$ is preferentially directed towards the O^{2-} ions of the BO_6 octahedra of the bigger sized B-site cation^{18,19}. EXAFS results of bond distance in several relaxor of type $\text{Pb}(\text{B}'\text{B}'')\text{O}_3$ where $r_{\text{B}'} > r_{\text{B}''}$ and $\text{B}'' = \text{Nb}$, are shown in the Table 4.1.

Table 4.1 EXAFS results of bond distance in several $\text{Pb}(\text{B}', \text{Nb})\text{O}_3$
(Z=Zn, C=Co, N=Ni, I=In; CN stands for coordination number)

Material	Pb-O		B'-O		Nb-O(B''-O)	
	R(Å)	CN	R(Å)	CN	R(Å)	CN
PZN	2.38	2.6	2.03	5.2	1.92 2.12	3 3
PCN	2.39	2.9	2.08	6.0	1.92 2.13	3 3
PNN	2.40	2.6	2.06	6.1	1.93 2.13	3 3
PIN	2.39	2.8	--	--	1.93 2.12	3 3

EXAFS data revealed that in these complex perovskites, B''-O bond distances have two set of values. When B' cations are larger than the B'' cation, six oxygen ions situated in B'O₆ are pushed outward. This in succession make Pb²⁺ to move along <111> toward larger B' cation forming three stable Pb-O bonds to incorporate the lone-pair of electrons. This leads to distortion in B''O₆ octahedra and is confirmed from the two sets of B''-O (Nb-O) bond distance in the EXAFS results.

This preferential displacement leads to decoupling of Pb-O-B'' bond along <111> as shown in Fig. 4.3(a). Alternatively if the B' cation is smaller than B'' cation, then Pb²⁺ is attracted to larger B'' so that the Pb-O-B'' coupling exists as shown in Fig. 4.3(b).

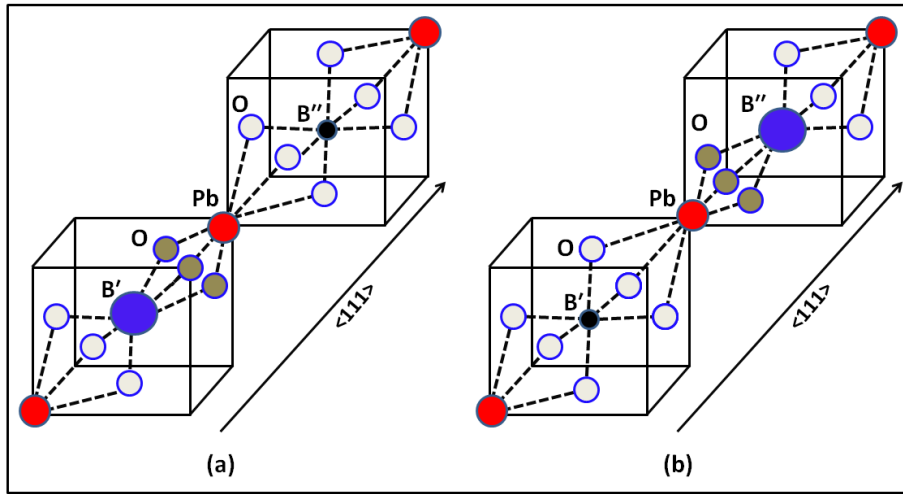


Figure 4.3 Schematic bonding in $\text{Pb}(\text{B}', \text{B}'')\text{O}_3$ (a) $r_{\text{B}'} > r_{\text{B}''}$, (b) $r_{\text{B}'} < r_{\text{B}''}$

However a completely different mechanism has been reported in $\text{Pb}(\text{Sc}_{0.50}\text{Ta}_{0.50})\text{O}_3$ [PST]. Substitution of Pb^{2+} by Ba^{2+} , which doesn't have the ns^2 lone pair, leads to suppression of long range ferroelectric ordering and enhance non-ergodic canonical relaxor states^{20,21} whereas the parent compound PST is known to undergo a transition to the ferroelectric (FE) state²². There is scatter in data in literature with regard to the origin of the relaxor state. Therefore it is interesting to study the influence of A-site isovalent substituent Pb^{2+} on the FE→R transition in the ferroelectric $\text{Ba}(\text{In}_{0.50}\text{Nb}_{0.50})\text{O}_3$. Recently our studies on $\text{Pb}(\text{In}_{0.50}\text{Nb}_{0.50})\text{O}_3$ [PIN] have shown the influence of the size difference between the B-site cations on the R→FE transition²³. Variations in the A-O and B-O bond strengths as a result of chemical substitution at A- and/or B-sites can alter the local symmetry around the B' and B'' cations and such local structural deviations significantly influence the vibrational modes^{20,21,23}. Therefore our aim is to study in detail the factors responsible for local structural rearrangements in the complex perovskite system $(\text{Ba}_{1-x}\text{Pb}_x)(\text{In}_{0.50}\text{Nb}_{0.50})\text{O}_3$ using an efficient tool like Raman spectroscopy to better understand the subtle factors responsible for FE→R transition. The influence

of bonding preferences on local structure has been further established by studying variations in the Raman spectra when a third cation (Sn^{4+}), having intermediate size and valency is introduced in B-site. We report clear insights into local structural rearrangements in relaxor complex perovskites.

4.2 Experimental Procedure

Barium acetate (99.5%, Qualigens, India), Lead acetate trihydrate (99%, Merck, India), Indium(III) acetylacetonate (99.99%, Aldrich, Germany), Tin (IV) acetate (Aldrich, Germany) and Niobium(V) ethoxide (99.95%, Aldrich, Germany) were used as starting materials for the preparation of compositions. To a solution of niobium ethoxide in isoamylalcohol, acetyl acetone was added as a complexing agent to avoid precipitation of niobium hydrous oxide. Indium acetylacetonate dissolved in acetic acid was added to this solution under continuous stirring to yield a mixed solution containing stoichiometric amounts of indium and niobium. To this clear solution, barium acetate, lead acetate trihydrate and tin acetate in acetic acid was added and stirring continued for another one hour to get a clear precursor solution. 3% excess lead was taken to compensate for lead loss during high temperature processing. The clear solution thus prepared was then transferred to a petridish and allowed to gel under ambient conditions²³. Xerogel obtained was calcined at 750 °C for 2 hours. The calcined powder was mixed with a small amount of PVA (polyvinyl alcohol) and the mixture was uniaxially pressed into pellets. The pressed pellets were sintered at 1290 °C for 3 hours. Sintered pellets were powdered and used for X-ray and Raman scattering experiments. Crystalline phase of sintered samples was identified with X-ray diffractometer (Model-D5005, Bruker, Germany) with $\text{CuK}\alpha$ radiation. We performed powder XRD measurements on our samples at room temperature. Raman scattering experiments were done by using 532 nm SSDP laser of 10 mW power on a Raman spectrometer (DXR Raman,

Thermo Scientific, USA). For dielectric measurements sintered pellets were polished and electroded with silver paste followed by curing at 700°C for 15 minutes. Dielectric properties of the sintered specimens were determined at frequencies of 10, 50 and 100 kHz using an impedance analyzer (Model-4192A, Agilent, USA) interfaced to high precision temperature bath (Model-7380, Fluke, Germany).

4.3 Results and Discussion

XRD patterns of all prepared compositions are shown in Fig.4.4. From the XRD patterns it is observed that all the compositions have high degree of crystallinity. Superlattice reflections corresponding to B-site order could not be observed and the average structure considered for the whole series in $(\text{Ba}_{1-x}\text{Pb}_x)(\text{In}_{0.50}\text{Nb}_{0.50})\text{O}_3$ is cubic.

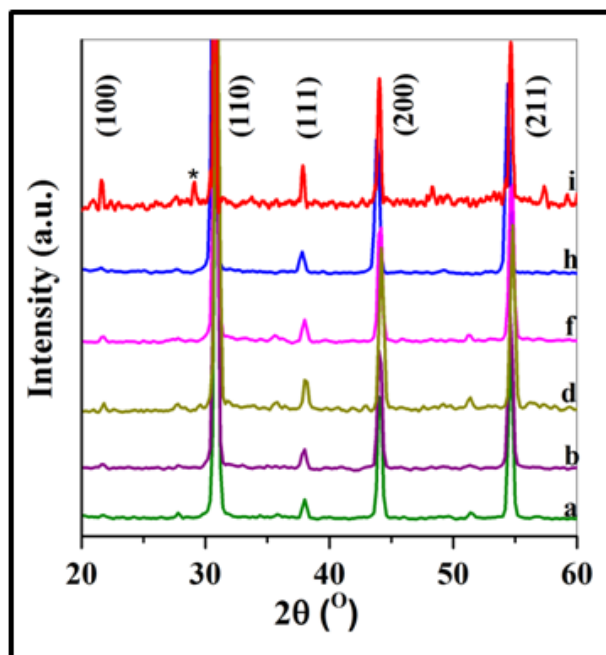


Figure 4.4 X-ray diffraction patterns of $((\text{Ba}_{1-x}\text{Pb}_x)(\text{In}_{0.50}\text{Nb}_{0.50})\text{O}_3$; x=a)0, b)0.1, d)0.3, f)0.5, h)0.8, i)1.0 (* - pyrochlore phase)

In order to precisely determine the structure, refinement of XRD data using Rietveld method was carried out for both the end members of the series i.e., for compositions having $x=0$, and $x=1$ by using GSAS program.²⁴ Pseudo-Voigt function was used for peak profile refinement. When $x=0$ (BIN), structure could be refined in $Fm\bar{3}m$ symmetry [Fig. 4.5 (A)] with $a=8.2819(0)$ Å and Ba, In/Nb, O atoms in 8c, 4a/4b, 24e Wyckoff positions respectively as reported earlier²⁵.

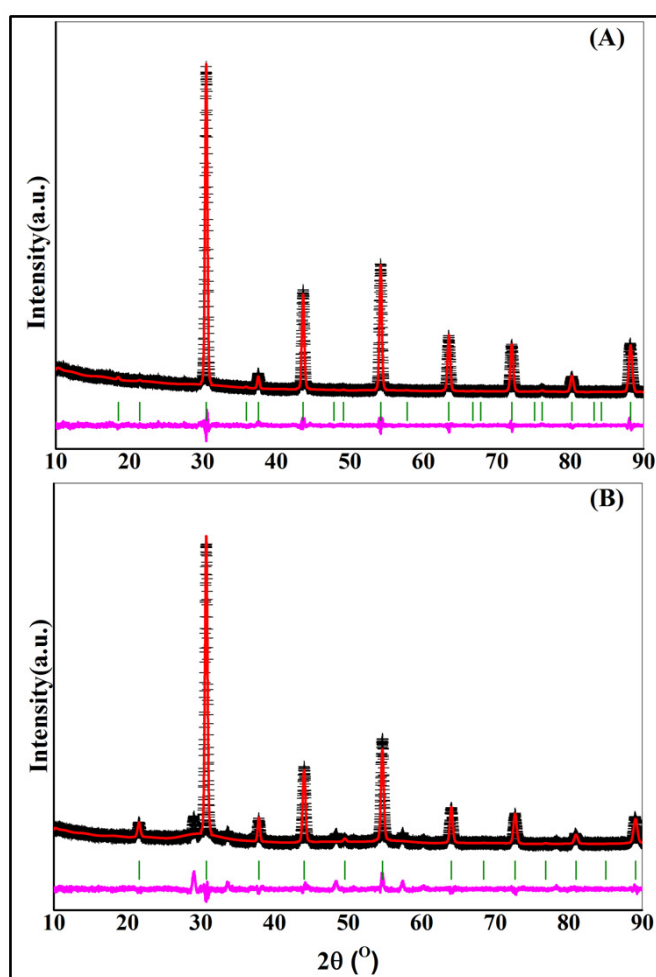


Figure 4.5 (A) The Resultant powder X-ray diffraction profile fits to Ba_2InNbO_6 . The refinement statistics at convergence were $R_{wp}=7.5$, $R_p=5.4$, $\chi^2 = 1.2$; (B) The Resultant Powder X-Ray diffraction profile fits to $Pb(In_{0.50}Nb_{0.50})O_3$. The refinement statistics at convergence were $R_{wp}=8.0$, $R_p=6.4$, $\chi^2 = 2.4$

For $Fm\bar{3}m$ symmetry, the occupied Wyckoff positions in the perovskite structure and corresponding phonon modes are given in Table 4.2. In a complex perovskite structure with $Fm\bar{3}m$ symmetry, among the normal modes $A_{1g}(R) + E_g(R) + 2F_{2g}(R) + 5F_{1u}(IR) + F_{2u}(\text{silent}) + F_{1g}(\text{silent})$, allowed Raman modes are A_{1g} , E_g and $2F_{2g}$ ²⁶.

Table 4.2 Wyckoff positions and corresponding phonon modes in $Fm\bar{3}m$

Atoms	Wyckoff position, $Fm\bar{3}m$	Phonon mode, $Fm\bar{3}m$	
		acoustic	optic
A	8c	F_{1u}	$F_{2g}(R)$
B'	4a		$F_{1u}(IR)$
B''	4b		$F_{1u}(IR)$
O	24e		$A_{1g}(R)+E_g(R)+2F_{1u}(IR)+F_{1g}(I)+F_{2g}(R)+F_{2u}(I)$

We could refine the structure when $x=1$ (PIN) in $Pm\bar{3}m$ symmetry [Fig. 4.5 (B)] with $a=4.1090(0)$ Å and Pb, In/Nb, O atoms in 1a, 1b, 3c Wyckoff positions respectively as shown in Table 4.3.

Table 4.3 Wyckoff positions and corresponding phonon modes in $Pm\bar{3}m$

Atoms	Wyckoff position, $Pm\bar{3}m$	Phonon mode, $Pm\bar{3}m$	
		acoustic	optic
A	1a	F_{1u}	
B	1b		$F_{1u}(IR)$
O	3c		$2F_{1u}(IR)+F_{2u}(I)$

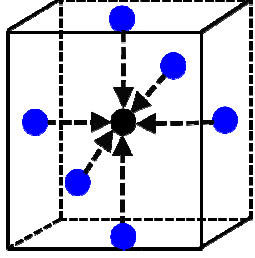
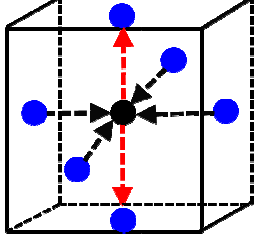
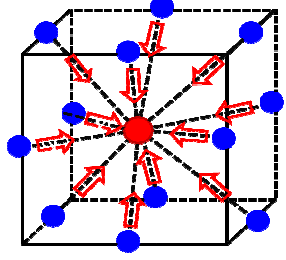
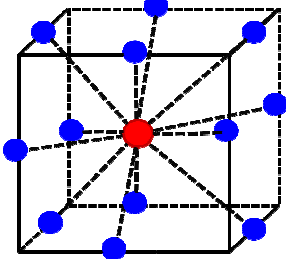
A cubic perovskite of $Pm\bar{3}m$ symmetry does not exhibit first order Raman bands (Table 4.3). In a complex perovskite of two B-site cations having 1:1 chemical ordering, doubling of the unit cell results and lead the structure to face-centered cubic symmetry $Fm\bar{3}m$. It is reported that in PIN, 1:1 B-site ordered clusters in the nanoscale having $Fm\bar{3}m$ symmetry²⁷ exist in

the disordered $Pm\bar{3}m$ matrix. Presence of mainly two bands near 800 cm^{-1} and 60 cm^{-1} in Raman spectra for PIN, are clear indications of doubling of unit cell on a local scale giving $Fm\bar{3}m$ symmetry²⁸⁻³⁰. Accordingly for the other compositions which lie within these extremes, Raman bands are assigned by considering $Fm\bar{3}m$ symmetry.

4.3.1 Origin of Raman bands

Four Raman active modes of $Fm\bar{3}m$ symmetry with corresponding phonon vibrations are shown in Table 4.4^{27,31,32}. In highest frequency, A_{1g} vibration, all the cations are at rest and only oxygen atoms are displaced as represented in Table. 4.4. This is clearly the totally symmetric stretching vibration of BO_6 octahedron. This type of vibration should give a strong Raman peak at relatively high frequency and thus assigned to the strong peak in the $850\text{-}700\text{ cm}^{-1}$. It's frequency is determined by the $B''\text{-O}$ bond strength, which depends on the chemical nature of B'' -site cation. In an E_g mode the B'' ion is not moving, while four of the oxygens approach B'' -cation and two are pushed away from the center ion. The corresponding band is assigned to weak peak around the $500\text{-}550\text{ cm}^{-1}$ region. In the two F_{2g} modes, one is characterised by the translation of the large A-cation. Such A-cation vibrations appear at lower frequency $50\text{-}150\text{ cm}^{-1}$ region. The other F_{2g} mode associated with oxygen displacement in A-O bond stretching. The two peaks that appear in the spectral range $300\text{-}400\text{ cm}^{-1}$ are assigned to this F_{2g} mode.

Table 4.4 Mode assignment for the symmetry allowed Raman active modes in $Fm\bar{3}m$

Mode	Approximate Wavenumber	Phonon vibration	
A_{1g}	850-750 cm^{-1}	Symmetric BO_6 stretching	
E_g	500-550 cm^{-1}	Symmetric B-O stretching	
F_{2g}	300-400 cm^{-1}	A-O bond stretching	
F_{2g}	50-140 cm^{-1}	A-cation vibrations	

Raman spectra of compositions of $(\text{Ba}_{1-x}\text{Pb}_x)(\text{In}_{0.50}\text{Nb}_{0.50})\text{O}_3$ is given in Fig. 4.6. For better understanding, Raman bands are displayed in three sections, (A) from 80 to 240 cm^{-1} , (B) from 250 to 500 cm^{-1} and (C) from 450 to 900 cm^{-1} . The modes near 800 cm^{-1} and 520 cm^{-1} are assigned to characteristic A_{1g} and E_g modes of $\text{Fm}\bar{3}m$ symmetry respectively. The strong mode at 390 cm^{-1} and the weak one at 300 cm^{-1} are assigned to F_{2g} symmetry. The A-cation localized mode F_{2g} (A) at 55-60 cm^{-1} and 90-110 cm^{-1} are assigned to Pb^{2+} and Ba^{2+} respectively. To analyse the influence of introduction of Pb^{2+} , having a lone pair of electrons, in $\text{Ba}(\text{In}_{0.50}\text{Nb}_{0.50})\text{O}_3$, we have studied Raman spectra of compositions of the type $(\text{Ba}_{1-x}\text{Pb}_x)(\text{In}_{0.50}\text{Nb}_{0.50})\text{O}_3$, where 'x' varies from 0 to 1. In Fig. 4.6(C), the band around 800 cm^{-1} is attributed to the symmetric stretching (A_{1g}) of the $\text{B}''\text{O}_6$ octahedra from a 1:1 chemically ordered region^{27,31}. Changes in A_{1g} mode sharpness, width and wave number reflect subtle changes in perovskite B-sublattice³². Introduction of Pb^{2+} resulted in splitting of A_{1g} mode. The antisymmetric $\text{B}''\text{O}_6$ stretching mode appears at $\approx 780 \text{ cm}^{-1}$ [Fig. 4.6(C) b-h].

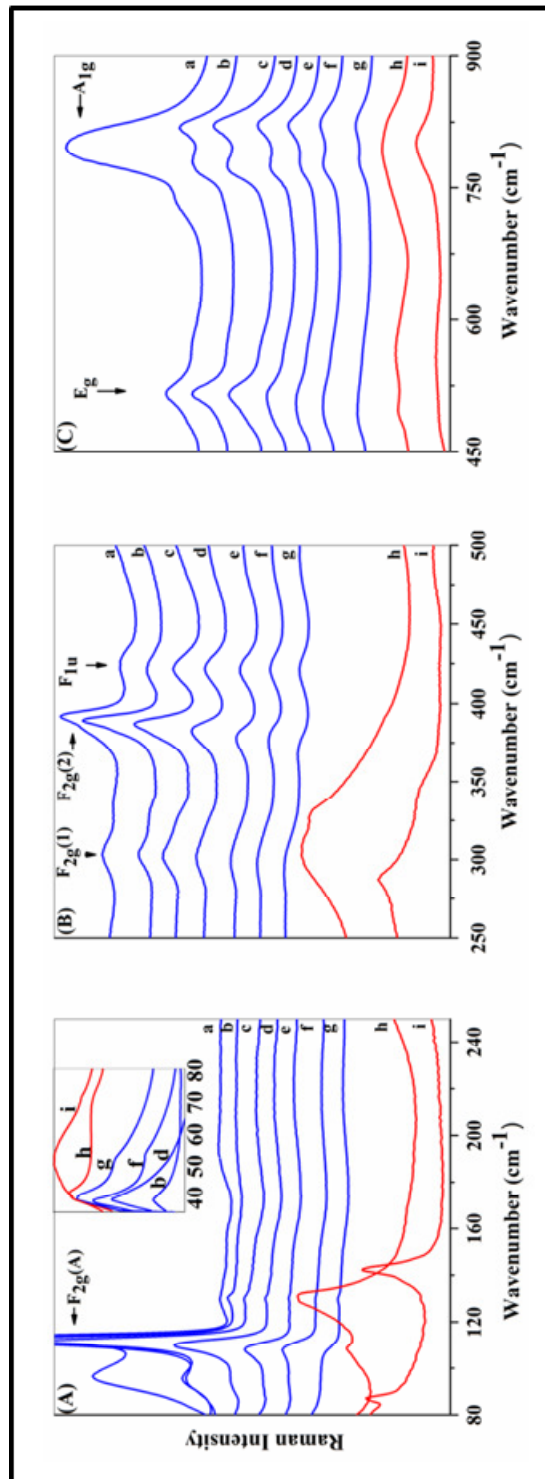


Figure 4.6 Raman spectra of $(\text{Ba}_{1-x}\text{Pb}_x)(\text{In}_{0.50}\text{Nb}_{0.50})\text{O}_3$, where $x = a)0, b)0.1, c)0.2, d)0.3, e)0.4, f)0.5, g)0.6, h)0.8, i)1.0$. Inset of Fig. 2(A) shows Raman spectra of wave number region $40 - 80\text{cm}^{-1}$.

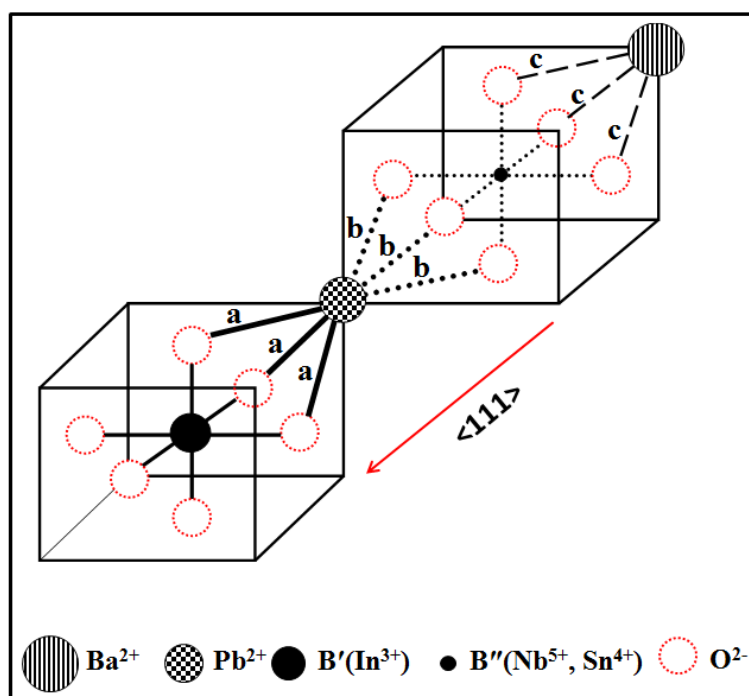


Figure 4.7 Representative structural fragment in the complex perovskite along $\langle 111 \rangle$

This is attributed to distortion in NbO_6 octahedra due to asymmetry arising in Nb-O bonds adjoining Pb^{2+} (\mathbf{b} in Fig. 4.7) and Ba^{2+} (\mathbf{c} in Fig. 4.7). When there is only one A-site cation (when $x=0$ and 1) due to lack of asymmetry in the two A-O bonds, no splitting is observed in this A_{1g} mode [Fig.4.6(C) a, i]. Full width at half maximum (FWHM), peak position and intensities were determined by using Lorentzian profile fitting. FWHM of the A_{1g} mode was determined from deconvolution of mode near 820 cm^{-1} using Lorentzian profile fitting. The perfect match of the composite peak result line with the obtained Raman peaks indicated the correctness of the peak deconvolution. FWHM of A_{1g} and E_g modes are shown in Fig. 4.8(A). It is observed that with increasing substitution of Ba^{2+} by Pb^{2+} , A_{1g} and E_g modes becomes broader, clearly indicating the increasing degree of disorder at B sublattice^{28,30}.

We also observe more interesting features in the stretching vibrations of A-O bond, F_{2g} (1) mode at 300 cm^{-1} and F_{2g} (2) at 390 cm^{-1} corresponding to bonds '**a**' and '**b**' respectively in Fig. 4.7. It is observed that with increasing Pb^{2+} content (x), F_{2g} (2) mode shifts to lower wavenumbers [Fig. 4.8(B)], becomes less intense and broadened. This is because the Pb-O bonds ('**b**' in Fig. 4.7) become weak as a result of the displacement of Pb^{2+} ions along $\langle 111 \rangle$ towards the O^{2-} ions of InO_6 octahedra¹⁸. The ratio of intensities of two F_{2g} peaks ($I_{F_{2g}(2)}/I_{F_{2g}(1)}$) is shown in Fig. 4.8(C). It is observed that the F_{2g} (2) peak intensity is greater than that of F_{2g} (1) for $0.1 \leq x \leq 0.3$. For compositions having $x > 0.3$, the F_{2g} (2) peak intensity becomes less than that of F_{2g} (1). Consistency in intensity and position of the $F_{2g}(1)$ mode is attributed to the increase in the Pb-O bond strength ('**a**' in Fig.4.7) due to Pb^{2+} translation along $\langle 111 \rangle$. Pb-O-Nb decoupling, as a consequence of this Pb^{2+} shift, also results in lesser B'- B'' interaction leading to disorder at B-site.

For higher values of ' x ' it is seen that in addition to the allowed Raman modes for the $\text{Fm}\bar{3}\text{m}$ symmetry, some forbidden modes also appear in the spectra mainly below 300 cm^{-1} . Emergence of these peaks is due to the distortion in $\text{Fm}\bar{3}\text{m}$ symmetry as a result of local structural rearrangements along $\langle 111 \rangle$ resulting in decoupling of Pb-O-Nb bond. For easy assignment of peaks in the spectra at higher values of ' x ' (when $x=0.8$) the deconvoluted spectrum is shown in Fig. 4.9. The F_{1u} mode at about 130 cm^{-1} corresponds to BO_3 -Pb translation along $\langle 111 \rangle$ ²⁸. The electrostatic repulsion between the Pb-O bonds and the ns^2 lone pair of electrons of Pb^{2+} responsible for this off-centring translation along $\langle 111 \rangle$ ^{16,17}. The soft mode at 40 cm^{-1} [inset of Fig. 4.6(A)] corresponds to this structural distortion along $\langle 111 \rangle$ ³³.

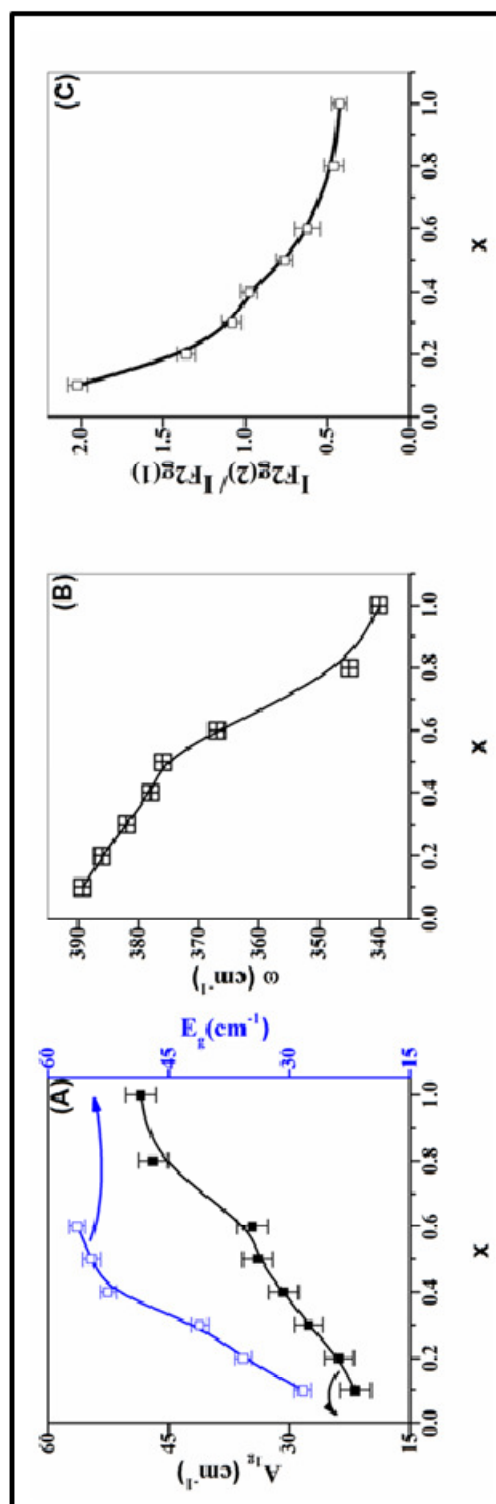


Figure 4.8 Composition dependence of (A) FWHMs of A_{1g} and E_g modes, (B) wavenumber (ω) of $F_{2g}(2)$ mode and (C) ratio of intensities $I_{F_{2g}(2)}/I_{F_{2g}(1)}$ for $(\text{Ba}_{1-x}\text{Pb}_x)(\text{In}_{0.50}\text{Nb}_{0.50})\text{O}_3$.

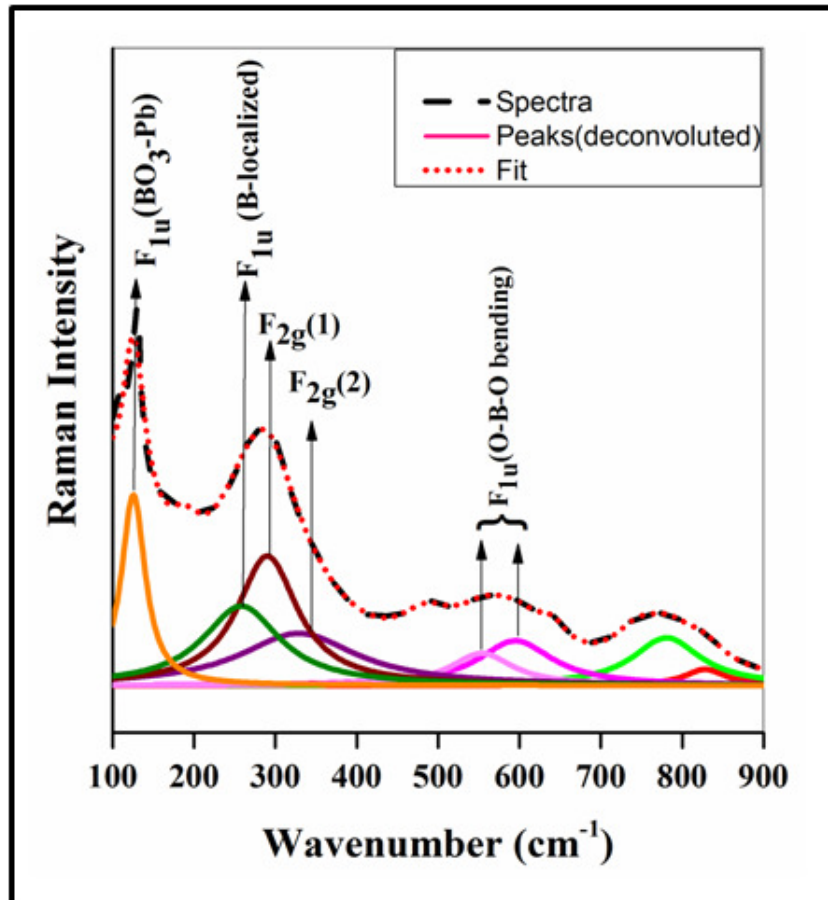


Figure 4.9 Deconvoluted Raman spectrum of $(\text{Ba}_{0.2}\text{Pb}_{0.8})(\text{In}_{0.50}\text{Nb}_{0.50})\text{O}_3$

This soft mode is merged with the Pb-cation localized $F_{2g}(A)$ mode [inset of Fig. 4.6(A)] at higher 'x' values. It is also interesting to observe a new peak near 260 cm^{-1} [Fig. 4.9] corresponding to F_{1u} mode of off-centered B'' -site cations in the polar nanoregions (PNR)^{20,28}. The mode near 420 cm^{-1} of medium intensity [Fig. 4.6(B)] is attributed to the O-B-O bending vibrations in $B''\text{O}_6$ octahedra corresponding to the infrared active F_{1u} mode in the prototype structure²⁸. It is observed that for higher values of 'x', the frequency of this mode is shifted to $500\text{--}600\text{ cm}^{-1}$ region [Fig. 4.9] confirming off-centre displacement of B'' ion in the $B''\text{O}_6$ octahedra²⁸.

Direct evidence for the local structural rearrangements were obtained by studying the changes in the Raman spectra (Fig. 4.10) when a third B-site cation, Sn^{4+} , is introduced to obtain compositions of the type $(\text{Ba}_{1-x}\text{Pb}_x)[\text{In}_{0.50}(\text{Sn}_{0.03}\text{Nb}_{0.476})]\text{O}_3$. It is interesting to observe two modes [as marked by arrows in Fig. 4.10(C) d-f] at 590 cm^{-1} and 640 cm^{-1} for compositions with $0.3 \leq x \leq 0.5$. This is attributed to the distortion of the SnO_6 octahedra resulting in variation in the Sn-O bond lengths due to asymmetric A-O bonds^{34,35}. At lower and higher values of 'x', due to more symmetrical A-O bonding, the distortion in SnO_6 octahedra is less. In Sn^{4+} -substituted compositions B-site order is retained relatively more as revealed by the FWHM values of A_{1g} and E_g modes [Fig. 4.11 (A)].

In Sn^{4+} -substituted compositions, the $\text{Sn}^{4+}\text{-O}^{2-}$ bonds are weak due to the absence of $d\pi\text{-}p\pi$ bonding since Sn^{4+} has no vacant d-orbitals³⁶. Also Sn^{4+} is bigger in size than Nb^{5+} ($r_{\text{Sn}^{4+}}=0.69\text{ \AA}$; $r_{\text{Nb}^{5+}}=0.64\text{ \AA}$). Therefore, the O^{2-} ions in the SnO_6 octahedra will be more closer to Pb^{2+} ion. Due to the above two factors, the bonds '**b**' in Fig. 4.7 will be relatively stronger. This retards the displacement of Pb^{2+} ion along $\langle 111 \rangle$ towards O^{2-} ions of the larger sized In^{3+} ion thus retaining the Pb-O-Sn coupling. For compositions in the range $0.1 \leq x \leq 0.5$, even after Pb^{2+} introduction at A-site, Pb-O-Sn coupling is retained as observed by the unchanged nature of the F_{2g} (2) mode at $\sim 390\text{ cm}^{-1}$ [Fig. 4.11(B)]. This clearly indicates a relatively stronger A-O bond ('**b**' in Fig. 4.7) due to the retarded $\langle 111 \rangle$ displacement of Pb^{2+} . This is also confirmed from the decrease in the frequency of the F_{1u} ($\text{BO}_3\text{-Pb}$ translation) mode from 140 cm^{-1} to 130 cm^{-1} [Fig. 4.10(A) i]. For higher lead-substituted compositions, $x > 0.5$, there is a significant shift in the F_{2g} (2) phonon mode. It is also interesting to note a significant change in the ratio of $I_{F_{2g}(2)}/I_{F_{2g}(1)}$ [Fig. 4.11(C)] when compared to that for compositions without Sn^{4+} -substitution [Fig. 4.8 (C)] clearly revealing the role of A-O-B decoupling on order-disorder transition.

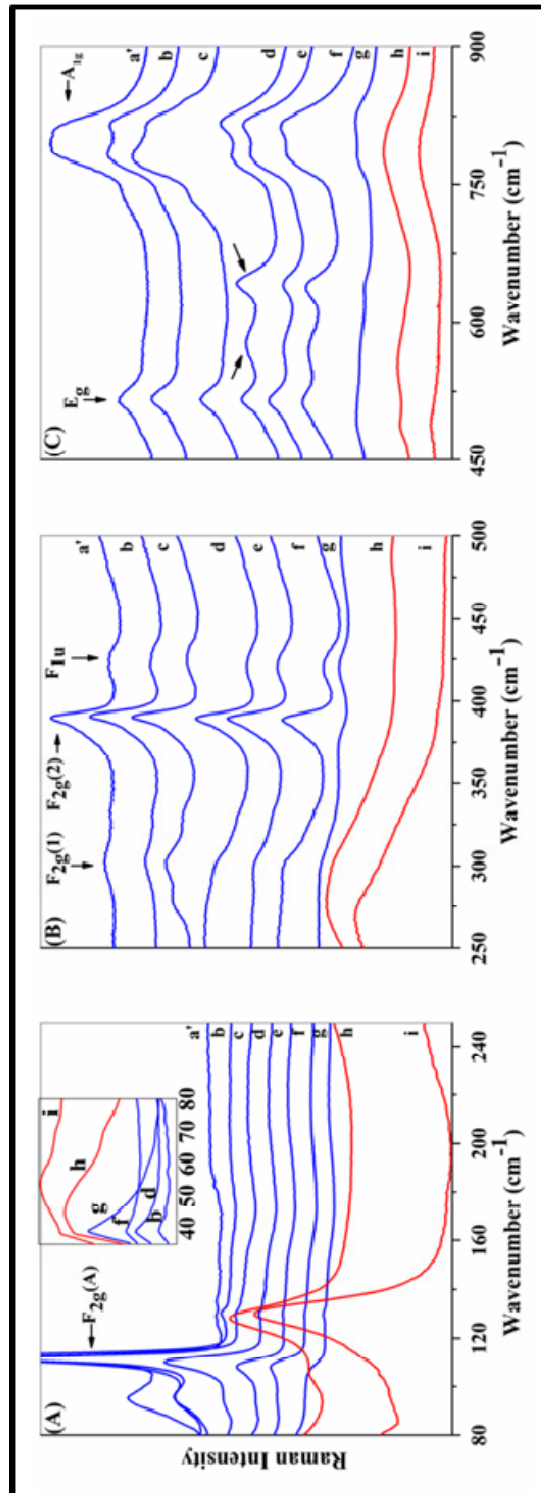


Figure 4.10 Raman spectra of $(\text{Ba}_{1-x}\text{Pb}_x) [\text{In}_{0.50}(\text{Sn}_{0.03}\text{Nb}_{0.476})\text{O}_3]$, where $x = \text{a)0, b)0.1, c)0.2, d)0.3, e)0.4, f)0.5, g)0.6, h)0.8, i)1.0}$. Inset of Fig. 6(A) shows Raman spectra of wave number region $40 - 80\text{cm}^{-1}$.

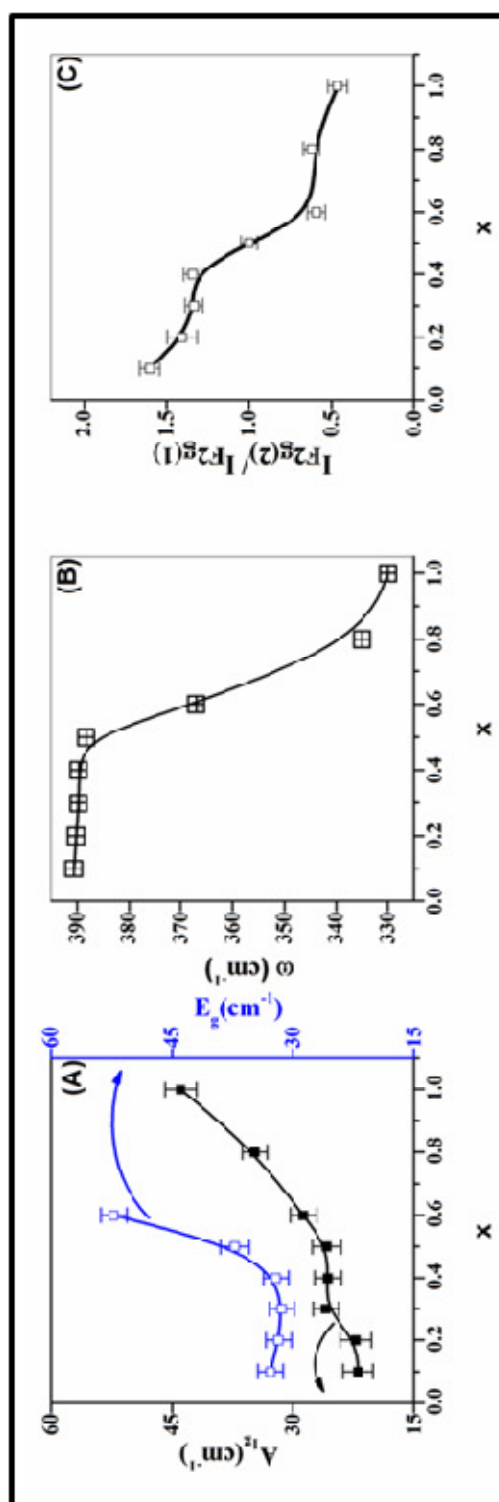


Figure 4.11 Composition dependence of (A) FWHMs of A_{1g} and E_g modes, (B) wavenumber (ω) of $F_{2g}(2)$ mode and (C) ratio of intensities $I_{F_{2g}(2)}/I_{F_{2g}(1)}$ for $(\text{Ba}_{1-x}\text{Pb}_x) [\text{In}_{0.50} (\text{Sn}_{0.03}\text{Nb}_{0.476})]\text{O}_3$.

Temperature dependent dielectric permittivities of selected compositions at different frequencies are shown in Fig. 4.12. It is seen that the temperature of maximum dielectric permittivity T_m , decreases with Sn^{4+} -substitution. This is in agreement with the weaker Sn^{4+} - O^{2-} bond strength as discussed earlier.

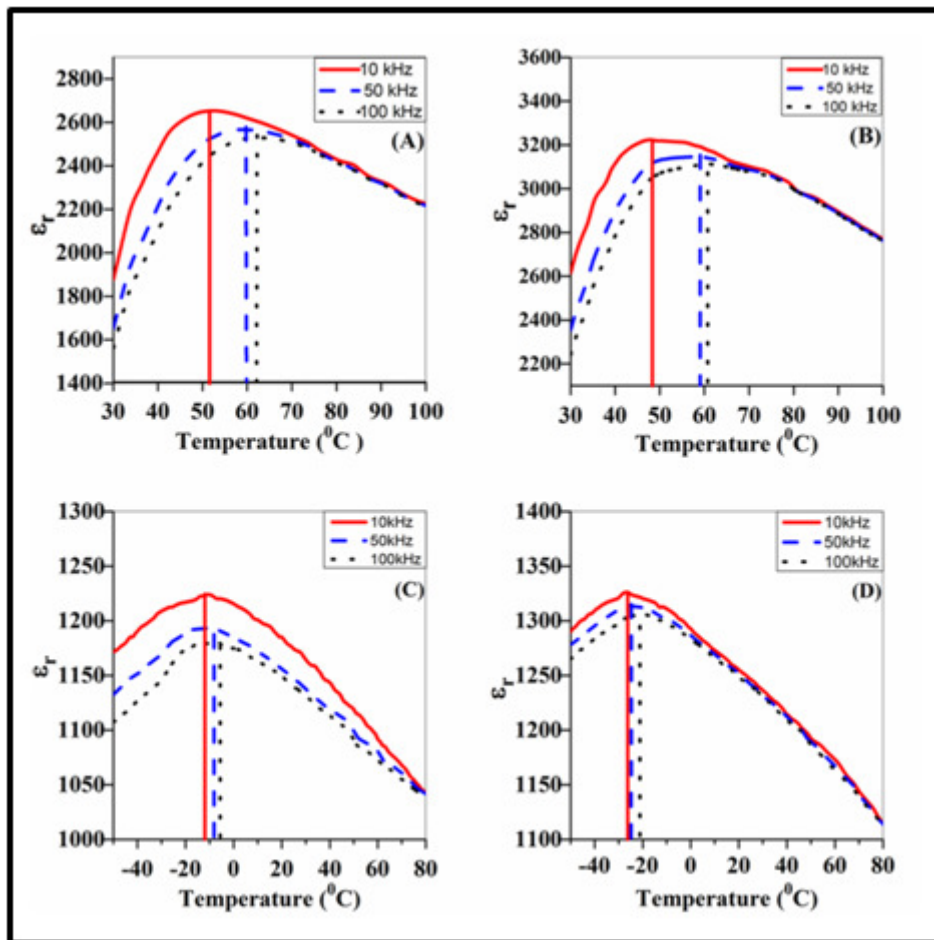


Figure 4.12 Dielectric permittivity as a function of temperature for

- (A) $\text{Pb}(\text{In}_{0.50}\text{Nb}_{0.50})\text{O}_3$;
- (B) $\text{Pb}[\text{In}_{0.50}(\text{Sn}_{0.03}\text{Nb}_{0.476})]\text{O}_3$;
- (C) $(\text{Ba}_{0.2}\text{Pb}_{0.8})(\text{In}_{0.50}\text{Nb}_{0.50})\text{O}_3$;
- (D) $(\text{Ba}_{0.2}\text{Pb}_{0.8})[\text{In}_{0.50}(\text{Sn}_{0.03}\text{Nb}_{0.476})]\text{O}_3$

It is also clearly observed that in Sn^{4+} -substituted compositions there is a decrease in the dispersion in the temperature dependence of dielectric permittivity [Figs. 4.12 (B) and (D)] when compared with those having no Sn^{4+} -substitution [Figs. 4.12 (A) and (C)]. These confirm the retention of Pb-O-Sn coupling. The above results clearly establish the crucial role of the strength of the Pb-O bonds adjacent to the ferroelectrically active $\text{B}''\text{O}_6$ octahedra in determining Pb-O-B'' coupling. While A-site Pb^{2+} substitution favors FE→R transition, B-site Sn^{4+} -substitution produces the opposite effect in $(\text{Ba}_{1-x}\text{Pb}_x)(\text{In}_{0.50}\text{Nb}_{0.50})\text{O}_3$.

4.4 Conclusion

Local structural rearrangements in lead-based complex perovskites of the type $(\text{Ba}_{1-x}\text{Pb}_x)(\text{In}_{0.50}\text{Nb}_{0.50})\text{O}_3$ responsible for transition from ferroelectric to relaxor are examined by careful analysis of their Raman spectra. Systematic Raman spectral investigation suggest that relaxor behavior in the lead based complex perovskites to be a consequence of stereo chemical influence of the ns^2 lone-pair electrons in Pb^{2+} . Due to the stereo chemical influence of this lone-pair of electrons, an off-center displacement of the lead atoms along the $\langle 111 \rangle$ is observed. The relative size of B-site cations have a prominent effect on this displacement along $\langle 111 \rangle$. Subtle changes in the bonding brought about by the differences in the chemical nature of A- and B-site cations have been correlated with the dynamic A-O-B coupling along $\langle 111 \rangle$. Through judicious substitutions at the A- and B-sites of the typical complex perovskite $(\text{Ba}_{1-x}\text{Pb}_x)(\text{In}_{0.50}\text{Nb}_{0.50})\text{O}_3$, deviations of the local structure as a result of such bonding preferences have been confirmed. Alterations in the A-O and B-O bond strengths that lead to local structural rearrangements have been comprehensively established by combining the results obtained from the dielectric data. This study provides clear insights into the mechanistic aspects of the FE→R transition in such complex perovskite systems.

References

- [1] A. A. Bokov and Z. G. Ye, “Recent progress in relaxor ferroelectrics with perovskite structure”, *J. Mater. Sci.*, 41 (2006) 31-52.
- [2] Z. G. Ye, “Relaxor ferroelectric complex perovskites: structure, properties and phase transitions”, *Key Eng. Mater.* 155–156 (1998) 81-122.
- [3] H. Ohwa, M. Iwata, H. Orihara, N. Yasuda and Y. Ishibashi, “Observation of the Distribution of the Transition Temperature in $\text{Pb}(\text{In}_{1/2}\text{Nb}_{1/2})\text{O}_3$ ”, *J. Phys. Soc. Jpn.*, 69 (2000) 1533-1545.
- [4] F. Chu, I. M. Reaney and N. Setter, “Investigation of relaxors that transform spontaneously into ferroelectrics”, *Ferroelectrics*, 151 (1994) 343-348.
- [5] J. Chen, H. M. Chan, and M. P. Harmer, “Ordering structure and dielectric properties of undoped and La/Na-doped $\text{Pb}(\text{Mg}_{1/3}\text{Nb}_{2/3})\text{O}_3$ ”, *J. Am. Ceram. Soc.*, 72 (1989) 593-598.
- [6] C. A. Randall and A. S. Bhalla, “Nanostructural-property relations in complex lead perovskites”, *Jpn. J. Appl. Phys.*, 29 (1990) 327-333.
- [7] A. D. Hilton, D. J. Barber, C. A. Randall, and T. R. Shrout, “On short range ordering in the perovskite lead magnesium niobate”, *J. Mater. Sci.*, 25 (1990) 3461-3466.
- [8] M. K. Akbas and P. K. Davies, “Domain growth in $\text{Pb}(\text{Mg}_{1/3}\text{Ta}_{2/3})\text{O}_3$ perovskite relaxor ferroelectric oxides”, *J. Am. Ceram. Soc.*, 80 (1997) 2933-2936.

- [9] P. K. Davies and M. A. Akbas, "Chemical order in PMN-related relaxors: structure, stability, modification, and impact on properties", *J. Phys. Chem. Solids*, 61 (2000) 159-166.
- [10] L. E. Cross, "Relaxor ferroelectrics", *Ferroelectrics*, 76, (1987) 241-267.
- [11] G. Smolenskii, V. A. Isupov, A. I. Agranovskaya and S.N. Popov, "Ferroelectrics with diffuse phase transitions", *Sov. Phys. Solid State*, 2 (1961) 2584-2588.
- [12] D. Viehland, S. Jang, and L. E. Cross, Freezing of the polarisation fluctuations in lead magnesium niobate relaxors", *J. Appl. Phys.*, 68 (1990) 2916-2921,
- [13] V. Westphal, W. Kleeman, and M. D. Glinchuk, "Diffuse phase transitions and random-field-induced domain states of the relaxor ferroelectric $\text{Pb}(\text{Mg}_{1/3}\text{Nb}_{2/3})\text{O}_3$ ", *Phys. Rev. Lett.*, 68 (1992) 847-850.
- [14] A. E. Glazounov and A. K. Tagantsev, "Phenomenological model of dynamic nonlinear response of relaxor ferroelectrics", *Phys. Rev. Lett.*, 85 (2000) 2192-2195.
- [15] R. Blinc, J. Dolinsek, A. Gregorovic, B. Zalar, C. Filipic, Z. Kutnjak, A. Levstik, and R. Pirc, "Local polarisation distribution and Edwards-Anderson order parameter of relaxor ferroelectrics", *Phys. Rev. Lett.*, 83 (1999) 424-427.
- [16] J. A. Alonso and I. Rasines, "On the influence of the non-bonded pair of Pb(II) in the novel ordered perovskite $\text{Pb}[\text{Sc}_{0.50}(\text{Ti}_{0.25}\text{Te}_{0.25})]\text{O}_3$ ", *J. Phys. Chem. Solids*, 49 (1988) 385-389.

- [17] S. A. Larregola, J. A. Alonso, M. Alguero, R. Jimenez, E. Suard, E. Porcher and J. C. Pedregosa, “Effect of Pb^{2+} lone pair in the structure and properties of the double perovskites $\text{Pb}_2\text{Sc}(\text{Ti}_{0.5}\text{Te}_{0.5})\text{O}_6$ and $\text{Pb}_2\text{Sc}(\text{Sc}_{0.33}\text{Te}_{0.66})\text{O}_6$: relaxor state due to intrinsic partial disorder”, *Dalton Trans.*, 39 (2010) 5159-5165.
- [18] I. W. Chen, P. Li and Y. Wang, “Structural origin of relaxor perovskites”, *J. Phys. Chem. Solids*, 57 (1996) 1525-1536.
- [19] I. W. Chen, “Structural origin of relaxor ferroelectrics-revisited”, *J. Phys. Chem. Solids*, 61 (2000) 197-208.
- [20] A-M. Welsch, B. J. Maier, J. M. Engel, B. Mihailova, R. J. Angel, C. Paulmann, M. Gospodinov, A. Friedrich, R. Stosch, B. Guttler, D. Petrova and U. Bismayer, “Effect of Ba-incorporation on pressure-induced structural changes in the relaxor ferroelectric $\text{Pb}(\text{Sc}_{0.5}\text{Ta}_{0.5})\text{O}_3$ ”, *Phys. Rev. B*, 80 (2009) 104118-1-10.
- [21] B. Maier, B. Mihailova, C. Paulmann, J. Ihringer, M. Gospodinov, R. Stosch, B. Güttler and U. Bismayer, “Effect of Local elastic strain on the structure of Pb-based relaxors: a comparative study of pure and Ba- and Bi-doped $\text{PbSc}_{0.5}\text{Nb}_{0.5}\text{O}_3$ ”, *Phys. Rev. B*, 79 (2009) 224108-1-10.
- [22] F. Chu, N. Setter and A. K. Tagantsev, “The spontaneous relaxor-ferroelectric transition of $\text{PbSc}_{0.5}\text{Ta}_{0.5}\text{O}_3$ ”, *J. Appl. Phys.*, 74 (1993) 5129-5134.
- [23] A. S. Divya and V. Kumar, “Influence of Fe^{3+} substitution on the dielectric and ferroelectric characteristics of lead indium niobate”, *J. Alloys Compd.*, 637 (2015) 426-430.

- [24] B. H. Toby “A graphical user interface for GSAS”, *J. Appl. Cryst.*, 34 (2001) 210-213.
- [25] V. Ting, Y. Liu, R.L. Withers, L. Nore´n, M. James and J.D. F. Gerald, “A structure and phase analysis investigation of the 1:1 ordered A_2InNbO_6 perovskites ($A=Ca^{2+}$, Sr^{2+} , Ba^{2+})”, *J. Solid State chem.*, 179 (2006) 551-562.
- [26] I. G. Siny, R. S. Katiyar and A. S. Bhalla, “Cation arrangement in the complex perovskites and vibrational spectra”, *J. Raman Spectrosc.*, 29 (1998) 385-390.
- [27] M. Ahart, S. Kojima, N. Yasuda and R. J. Hemley, “Successive pressure-induced structural transitions in relaxor lead indium niobate”, *Ferroelectrics*, 467 (2014) 138-145.
- [28] B. Mihailova, U. Bismayer, B. Guttler, M. Gospodinov and L. Konstantinov, “Local structure and dynamics in relaxor-ferroelectric $PbSc_{1/2}Nb_{1/2}O_3$ and $PbSc_{1/2}Ta_{1/2}O_3$ single crystals”, *J. Phys.: Condens. Matter*, 14 (2002) 1091- 1105.
- [29] I. G. Siny, R. S. Katiyar and A. S. Bhalla, “Raman scattering in ferroelectric relaxor perovskites and related thin films,” *Ferroelectrics Rev.*, 2 (2000) 51-113.
- [30] I. G. Siny, R. S. Katiyar and A. S. Bhalla, “Cation arrangement in the complex perovskites and vibrational spectra”, *J. Raman Spectrosc.*, 29 (1998) 385-390.
- [31] M. L. Duyckaerts and P. Tarte, “Vibrational studies of molybdates, tungstates and related compounds - iii ordered cubic perovskites $A_2B^{II}B^{VI}O_6$ ”, *Spectrochim. Acta*, 30A (1974) 1771-1786.

- [32] R. Ratheesh, M. Wöhlecke, B. Berge, T. Wahlbrink, H. Haeuseler, E. Rühl, R. Blachnik, P. Balan, N. Santha and M. T. Sebastian, “Raman study of the ordering in Sr (B_{0.5}Nb_{0.5}) O₃ compounds”, *J. Appl. Phys.*, 88 (2000) 2813-2818.
- [33] B. Mihailova, R. J. Angel, A- M. Welsch, J. Zhao, J. Engel, C. Paulmann, M. Gospodinov, H. Ahsbahs, R. Stosch, B. Guttler, and U. Bismayer, “Pressure-induced phase transition in PbSc_{0.5}Ta_{0.5}O₃ as a model Pb- based perovskite – type relaxor ferroelectrics”, *Phys. Rev. Lett.*, 101 (2008) 017602-1-4.
- [34] A-M. Welsch, B. J. Maier, B. Mihailova, R. J. Angel, J. Zhao, C. Paulmann, J. M. Engel, M. Gospodinov, V. Marinova and U. Bismayer, “Transformation processes in relaxor ferroelectric PbSc_{0.5}Ta_{0.5}O₃ heavily doped with Nb and Sn”, *Z. Kristallogr.*, 226 (2011) 126-137.
- [35] B. Mihailova, M. Gospodinov, B. G ü ttler, R. Stosch and U. Bismayer, “Ferroic clustering and phonon anomalies in Pb- based perovskite-type relaxors”, *J. Phys.: Condens. Matter*, 19 (2007) 275205-1-10.
- [36] V. Kumar, I. P. Selvam, K Jithesh and P. V. Divya, “Preparation and dielectric characteristics of nanocrystalline Ba(M_xTi_{1-x})O₃”, *J. Phys. D: Appl. Phys.*, 40 (2007) 2936-2940.

Defect-mediated Stabilization of Ferroelectric Phase in Antiferroelectric PZST

- 5.1 Introduction
- 5.2 Experimental Procedure
- 5.3 Results and Discussion
- 5.4 Conclusion
- References

Influence of B-site acceptor dopants, manganese and copper, on the sequence of phase transformations in antiferroelectric (AFE) $Pb(Zr_{0.60}Sn_{0.30}Ti_{0.10})O_3$ have been discussed. The sequence of phase transformations below the Curie point has been examined by dielectric, polarisation-electric field and strain-electric field studies. While the parent compound and B-site Cu^{2+} -doped composition exhibit the same sequence $FE \leftarrow AFE \leftarrow MCC$ with incommensuration in the multicell cubic (MCC) state in the case of B-site Mn^{3+} -doped system, incommensuration is found to be suppressed and only ferroelectric (FE) phase is observed below the Curie point. The underlying mechanism is related to the nature of defect complexes present in the system through detailed Electron Paramagnetic Resonance studies.

Some of the contents of this chapter have appeared in the following research publication.

Adukkadan Anil, Killimangalath Vani and Viswanathan Kumar, *Journal of the American Ceramic Society*, 101(2018) 3377-3382.

5.1 Introduction

Because of smaller free energy difference between antiferroelectric (AFE) and ferroelectric (FE) phases, when subjected to an external electric field above a critical value, the AFE phase is transformed to FE phase. This transition is accompanied by a large volume change as can be inferred from the figure given below (Fig.5.1).

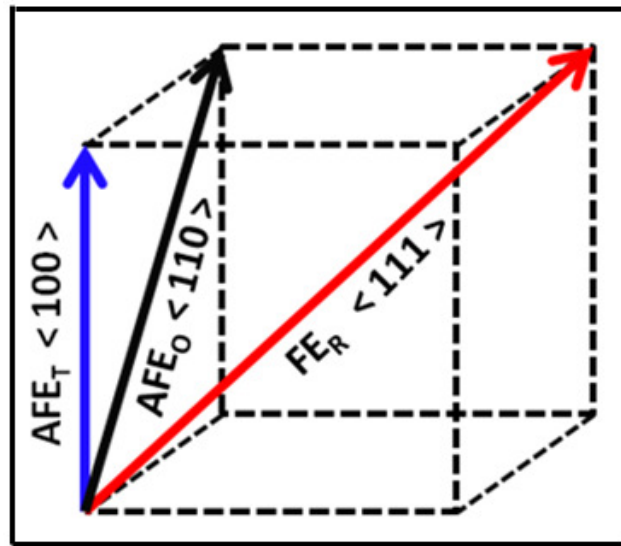


Figure 5.1 Schematic diagram of the primitive cell of AFE and FE states

This has been exploited for achieving large mechanical strains. In the typical AFE PbZrO_3 , during the transition from the paraelectric (PE) phase to orthorhombic AFE phase, existence of an intermediate rhombohedral FE phase near the Curie point have been reported^{1,2}. It has been reported that the temperature window of the stability of this FE phase has been influenced by addition of various impurities and presence of defects in the lattice. In A-site isovalent substitutions like Ba^{2+} -substituted PbZrO_3 , stability of FE phase has been enhanced whereas in the case of Sr^{2+} -substitution introduction of an intermediate AFE_T phase has been reported³. Stability of FE phase has been

reported to increase in B-site Nb^{5+} -doped PbZrO_3 containing Pb-vacancies as well as in undoped PbZrO_3 with induced oxygen vacancies^{4,5}. Also B-site isovalent substituent like Ti^{4+} stabilizes the FE phase while Sn^{4+} induces AFE phase of tetragonal symmetry⁶. Due to the presence of both ferroelectric and antiferroelectric phases, the ternary PbZrO_3 - PbTiO_3 - PbSnO_3 system holds strong scientific interest. Also Tin-modified lead zirconate titanate antiferroelectric ceramics are attractive in actuator applications as they exhibit large mechanical strains during field induced antiferroelectric (AFE) - ferroelectric (FE) transformation^{7,8}. However, many material systems in the PbZrO_3 - PbTiO_3 - PbSnO_3 ternary systems have also evinced considerable theoretical interest, especially with respect to the nature and sequence of the phase transformations below Curie point. Berlincourt et al⁹ reported complex phase transformation sequence for the compositions in this ternary system with increasing and decreasing temperatures. Aside from the different effect seen in the sequence of phase transformations, in certain Sn-modified lead zirconate titanate compositions, phase transition from paraelectric phase into AFE state is seen to proceed through an additional intermediate phase known as multi cell cubic (MCC) state. Temperature dependent electron diffraction studies reported that the single cubic (SC) paraelectric phase transformed to AFE phase through a incommensurate multicell cubic state (MCC) state¹⁰⁻¹². Such incommensurate modulations are characterized by satellite reflections in the electron diffraction patterns. In some material systems, incommensurate modulations have also been reported to be metastably locked in certain temperature region where modulation wavelength is independent of temperature¹³. Several mechanisms have been proposed for this structural modulation including octahedral tilting, Pb-cation displacement, and vacancy ordering¹⁴⁻¹⁶. Transformation of incommensurate phase to other phases can be triggered by external stimuli, such

as chemical composition, dc bias and temperature¹⁰. However, the exact cause of the incommensurate structure is still under debate. No detailed study has yet been carried out to understand the underlying mechanism responsible for the incommensurate modulations in tin modified lead zirconate titanate ceramics. Moreover, it has been reported that incommensurate modulations is strongly disturbed by small defect concentrations^{17,18}. Therefore, it is interesting to study the influence of defect structures on the FE→AFE phase transformation and existence of incommensuration in tin-modified lead zirconate titanate ceramics to derive clear insights on the structural modulations. For this study we have chosen the composition (shown in Fig. 5.2), $\text{Pb}(\text{Zr}_{0.60}\text{Sn}_{0.30}\text{Ti}_{0.10})\text{O}_3$ (PZST) close to AFE-FE phase boundary⁷ and doped with B-site aliovalent acceptors like Mn^{3+} and Cu^{2+} .

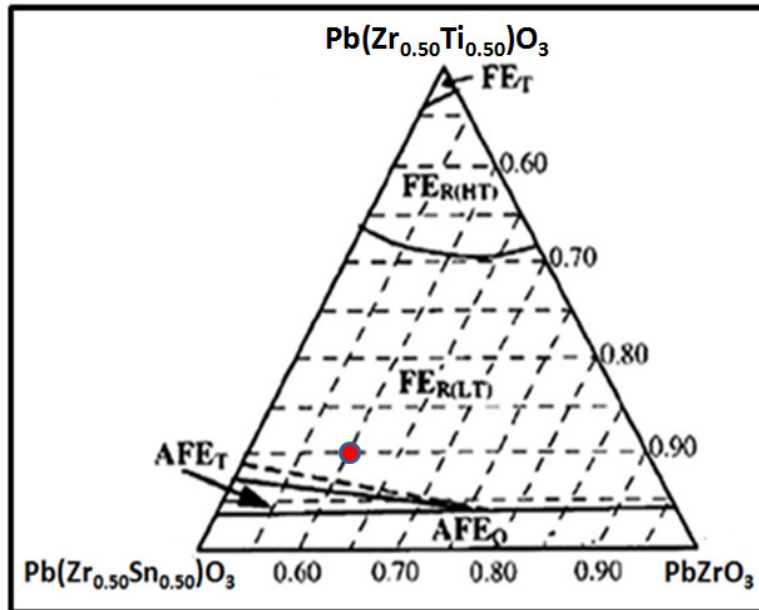


Figure 5.2 Ternary phase diagram for PbZrO_3 - PbTiO_3 - PbSnO_3 system. Red point indicated the composition chosen for this study

Motivation of this work is to establish the role of defect-structures on the phase transformation sequence in this material system. In addition, the

underlying mechanism responsible for formation of incommensurate modulations also discussed.

5.2 Experimental Procedure

Compositions having the general formula $\text{Pb}(\text{Zr}_{0.60}\text{Sn}_{0.30}\text{Ti}_{0.10})\text{O}_3$, $\text{Pb}(\text{Zr}_{0.60}\text{Sn}_{0.30}\text{Ti}_{0.10})_{0.9925}\text{Mn}_{0.01}\text{O}_3$, $\text{Pb}(\text{Zr}_{0.60}\text{Sn}_{0.30}\text{Ti}_{0.10})_{0.995}\text{Cu}_{0.01}\text{O}_3$ hereafter denoted as undoped PZST, Mn-doped PZST and Cu-doped PZST respectively were prepared by conventional solid state powder method from starting materials like PbO (98%, Qualigens, India), ZrO_2 (99%, Sigma Aldrich, UK), TiO_2 (99%, Merck, Germany), SnO_2 (99.9%, Sigma Aldrich, USA) and Mn_2O_3 (99%, Sigma Aldrich, USA), CuO (98%, Sigma Aldrich, Germany). The metal oxides were taken in a stoichiometric ratio according to the formula and mixed well by ball milling using distilled water as solvent, dried and calcined at 850°C for two hours. The calcined powder was made into 10 mm pellets by adding PVA as binder followed by hydrostatic pressing at a pressure of 200MPa. The specimens were sintered at 1250°C for 2 hours under controlled PbO atmospheres. Crystalline phase of the sintered samples were identified with X-ray diffractometer (XRD, Model-D5005 Bruker Karlsruhe, Germany) using $\text{CuK}\alpha$ radiation. Sintered pellets were polished and electroded with silver paste followed by curing at 700°C for 15 minutes. Dielectric properties of the sintered compacts were determined at 1 kHz using an Impedance-Gain phase analyzer (Model-4294 A, Agilent Technologies, USA) interfaced to a high precision furnace. Ferroelectric hysteresis (P–E and S–E) curves of samples were measured using a Piezoevaluation system (Model-FE2000, aixACCT, Germany) at 1Hz. Electron Paramagnetic Resonance spectroscopy of specimens were carried out using an EPR spectrometer (Model-JES FA200, JEOL, Japan) at liquid nitrogen temperature in the X band frequency of 9.17 GHz.

5.3 Results and Discussion

XRD patterns of the different compositions are shown in Fig. 5.3(A). It is seen that all compositions are phase-pure and have rhombohedral crystal structure. Temperature dependence of dielectric permittivity of undoped and doped PZST are given in Fig. 5.3(B). Both weak and strong anomalies are observed in dielectric permittivities. In the case of undoped PZST [Fig. 5.3(B)i], a weak dielectric anomaly is observed at temperature around 150°C and a stronger one at 190°C which is followed by a plateau in the permittivity upto a temperature of 220°C and then a sharp rise and transition to the PE state at 235°C. In the case of Cu-doped PZST [Fig. 5.3(B)ii] similar anomalies in the dielectric permittivity are observed as in the case of undoped PZST while in the case of Mn-doped PZST the plateau region in the permittivity [Fig. 5.3(B)iii] is absent. These can be explained as follows.

(i) in undoped PZST, at $T \approx 150^\circ\text{C}$ the dielectric anomaly corresponds to FE→AFE phase transition [Fig. 5.3(B)i]. This is confirmed from the P-E curves [Fig. 5.4(d)]. One distinct feature observed in the dielectric permittivity data is the presence of a plateau region between 190°C and 220°C. This plateau region observed is attributed to the broadened MCC state which is confirming the existence of metastable incommensurate phase¹⁰⁻¹⁴.

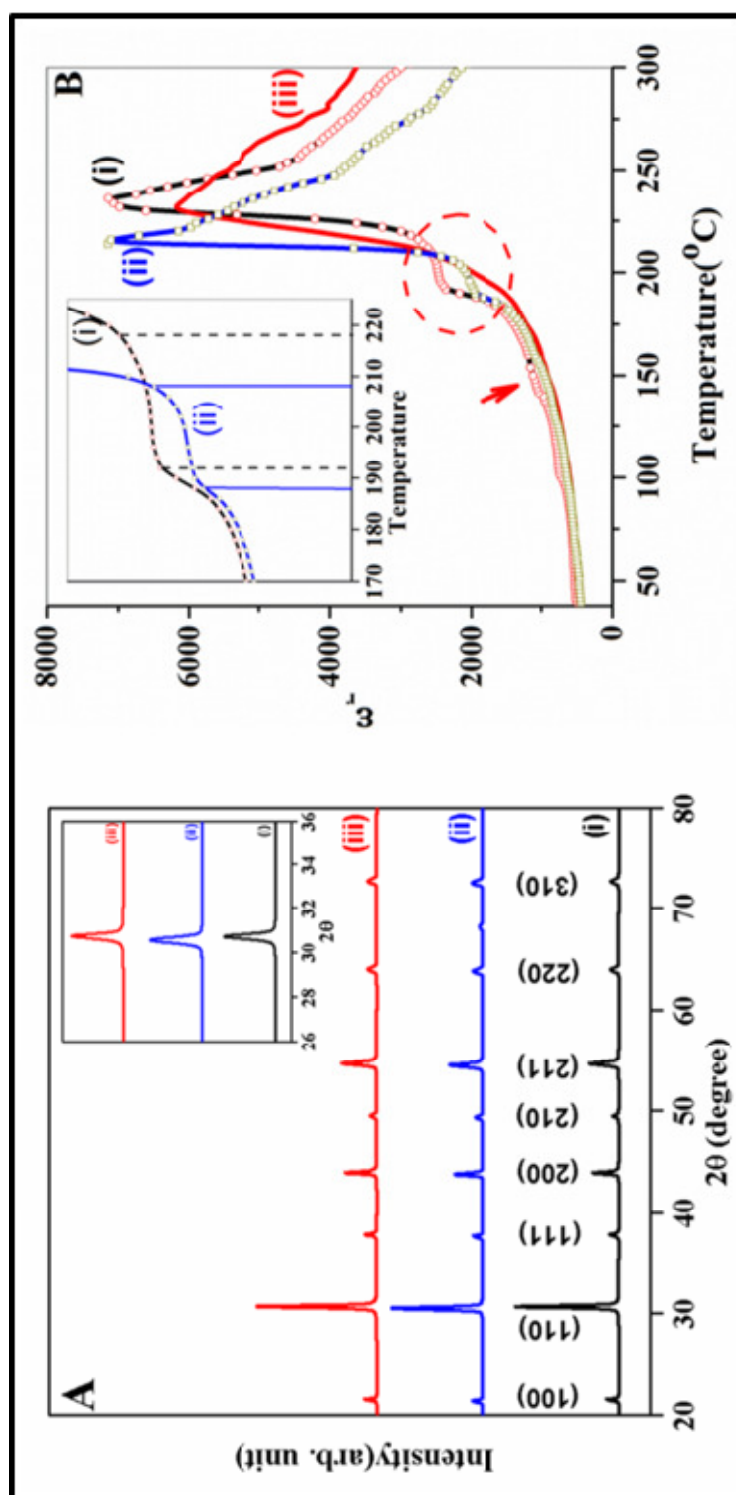


Figure 5.3 (A) XRD patterns and (B) plot of temperature dependent dielectric permittivity of (i) undoped PZST; (ii) Cu-doped PZST and (iii) Mn-doped PZST. Inset of (A) shows XRD patterns at 2θ between 26 and 36° and (B) those in the temperature region from 170°C to 225°C.

Therefore the sequence of phase transitions below Curie point, T_c , in this case is, $FE \leftarrow AFE \leftarrow MCC$.

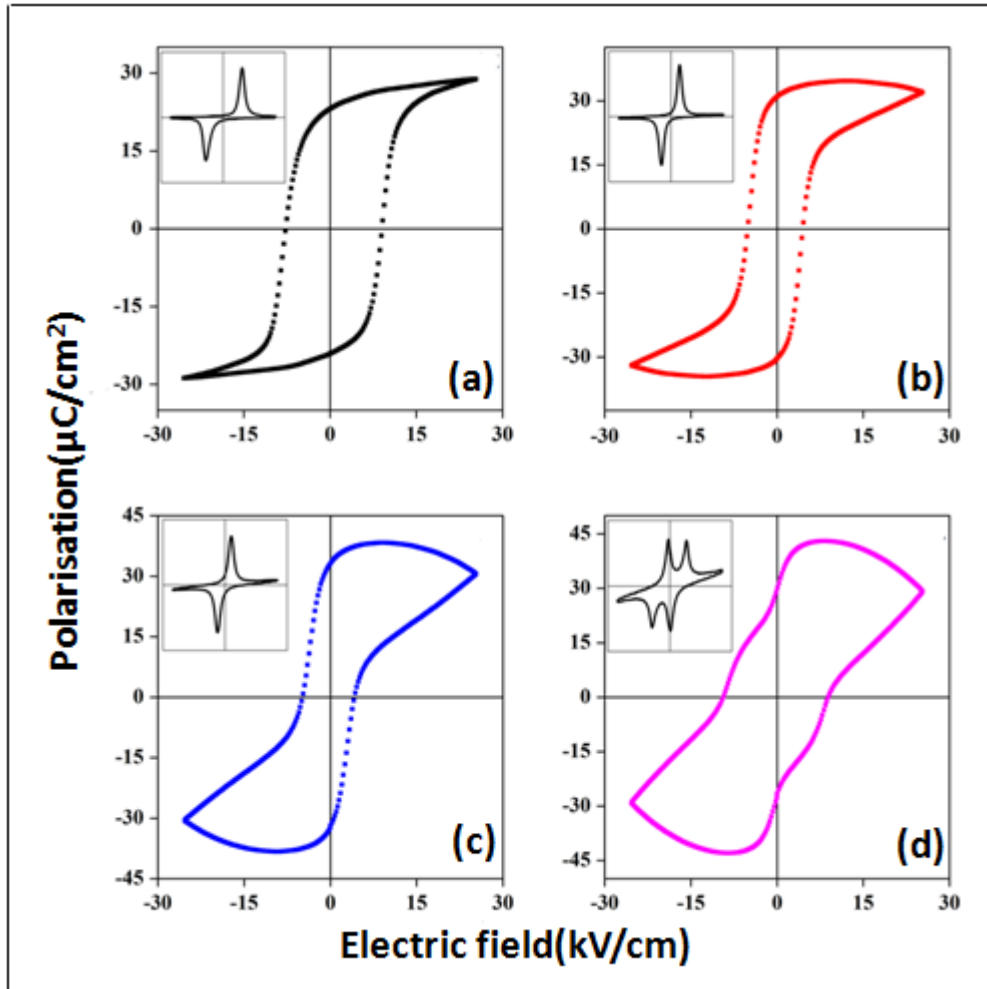


Figure 5.4 Temperature dependent P-E curves of undoped PZST; where (a) 30°C , (b) 130°C , (c) 140°C , (d) 150°C . Respective I-E curves are shown in insets.

(ii) in Cu-doped PZST similar sequence of phase transformations, as in the case of undoped PZST, are observed [Fig. 5.3(B)ii and Fig. 5.5(d)]. Therefore the sequence of phase transitions below T_c in this case is also $FE \leftarrow AFE \leftarrow MCC$.

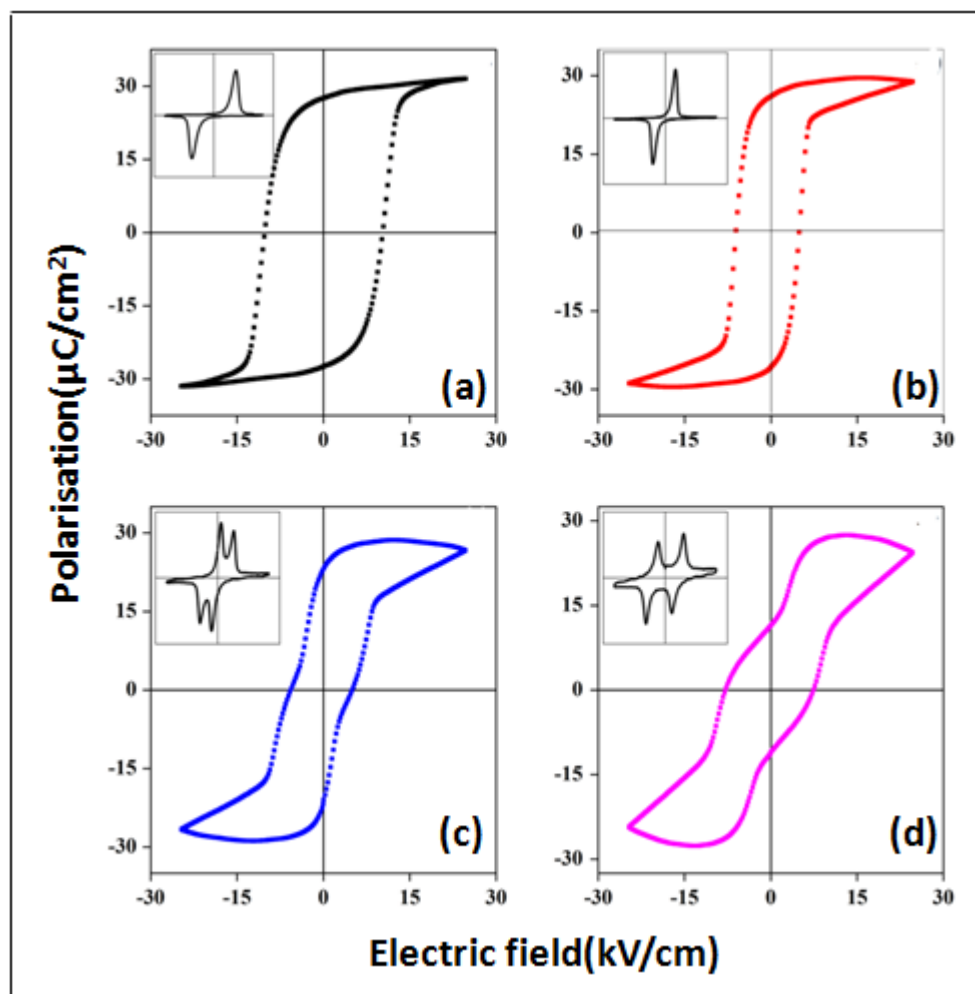


Figure 5.5 Temperature dependent P-E curves of Cu-doped PZST; where (a)30^oC, (b)130^oC, (c)140^oC, (d)150^oC. Respective I-E curves are shown in insets.

(iii) in Mn-doped PZST the FE→AFE phase transition is not clearly distinguishable from dielectric permittivity data [Fig. 5.3(B)iii] as well as from P-E curves [Fig. 5.6(d)]. It is therefore inferred that the transition to the AFE phase is significantly suppressed in this case. It is also observed that the plateau region, attributed to incommensuration in MCC state is absent. Therefore below T_c in this case only FE phase is observed.

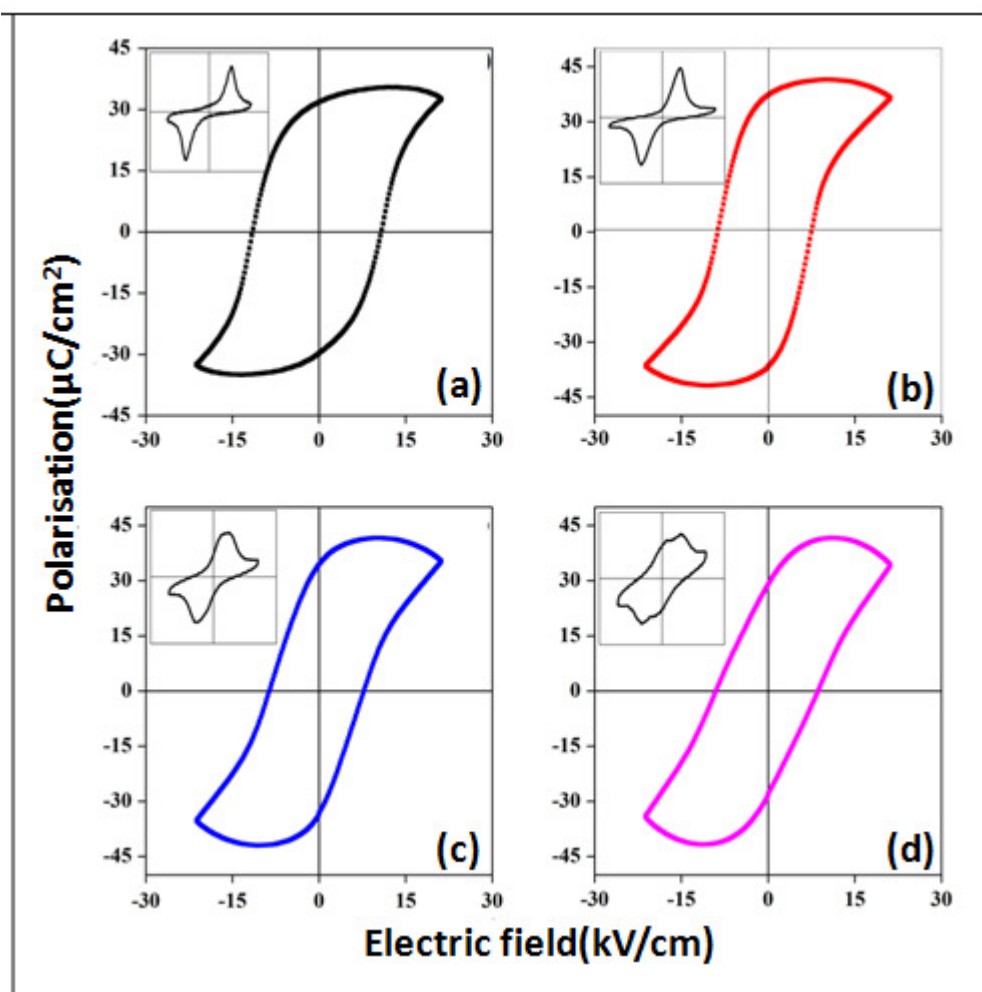


Figure 5.6 Temperature dependent P-E curves of Mn-doped PZST; where (a) 30^oC, (b)130^oC, (c)140^oC, (d) 150^oC. Respective I-E curves are shown in insets.

The FE-AFE phase transition is confirmed from the Strain-Electric field (S-E) loops recorded as a function of temperature as shown in Fig. 5.7. At the AFE→FE phase transition ($T \approx 150^{\circ}\text{C}$), maximum strain value is expected⁷. Maximum strain of 0.17% is observed in the case of undoped PZST. In the case of Mn-doped PZST, the butterfly shape of the curves clearly reveals the FE nature.

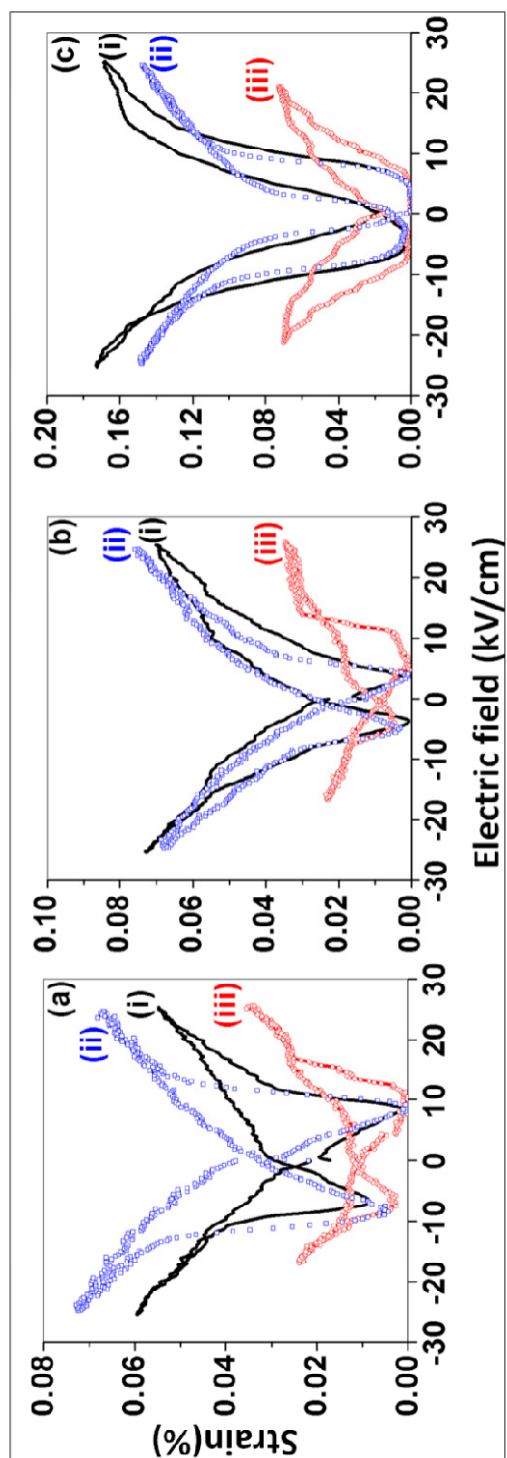
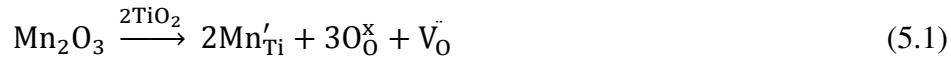


Figure 5.7 Temperature dependent S-E curves at (a) 30°C, (b) 130°C and (c) 150°C, where (i) undoped PZST; (ii) Cu-doped PZST and (iii) Mn-doped PZST

From the temperature dependent dielectric, P-E, I-E and S-E data, significant differences are observed on the influence of different acceptor dopants on the FE-AFE phase transformation and incommensuration in the MCC state. In undoped PZST, the difference in the free energies of formation of AFE and FE phases is very small. This intrinsic competition between the ferroelectric and antiferroelectric coupling leads to incommensuration with MCC state stable over a broad temperature window¹⁰⁻¹⁴. The distinct behaviour observed in the different acceptor-doped systems can be explained on the basis of the defect dipoles formed in the lattice since addition of aliovalent dopants in lead zirconate titanate result in formation of point defects¹⁹. For B-site acceptor doping, charge compensation is achieved through creation of oxygen vacancies¹⁹ as given in equations 5.1 and 5.2 for the B-sublattice.



Negatively charged acceptor dopant ions, Mn'_{Ti} and Cu''_{Ti} forms defect dipoles with the positively charged oxygen vacancy, $\text{V}^{\cdot\cdot}_{\text{O}}$ in the lattice²⁰⁻²². Evidence for such defect dipoles is obtained from EPR spectroscopy results. The EPR spectra were also simulated using *Easy Spin 4.0.0* program²³ using spin-Hamiltonian parameters given in Table 5.1. In the simulated spectra, hyperfine interactions with Mn-nucleus, $I = \frac{5}{2}$ is and Cu-nucleus, $I = \frac{3}{2}$ is also taken into consideration.

EPR spectrum of Mn-doped PZST is given in Fig. 5.8(A). Since Mn^{3+} is EPR silent, there are no signals corresponding to it in the EPR spectra. EPR signals shown in Fig. 5.8(A)i correspond to Mn^{4+} and Mn^{2+} centers²⁴ respectively which are confirmed from the simulated EPR spectra [Fig. 5.8(A)ii].

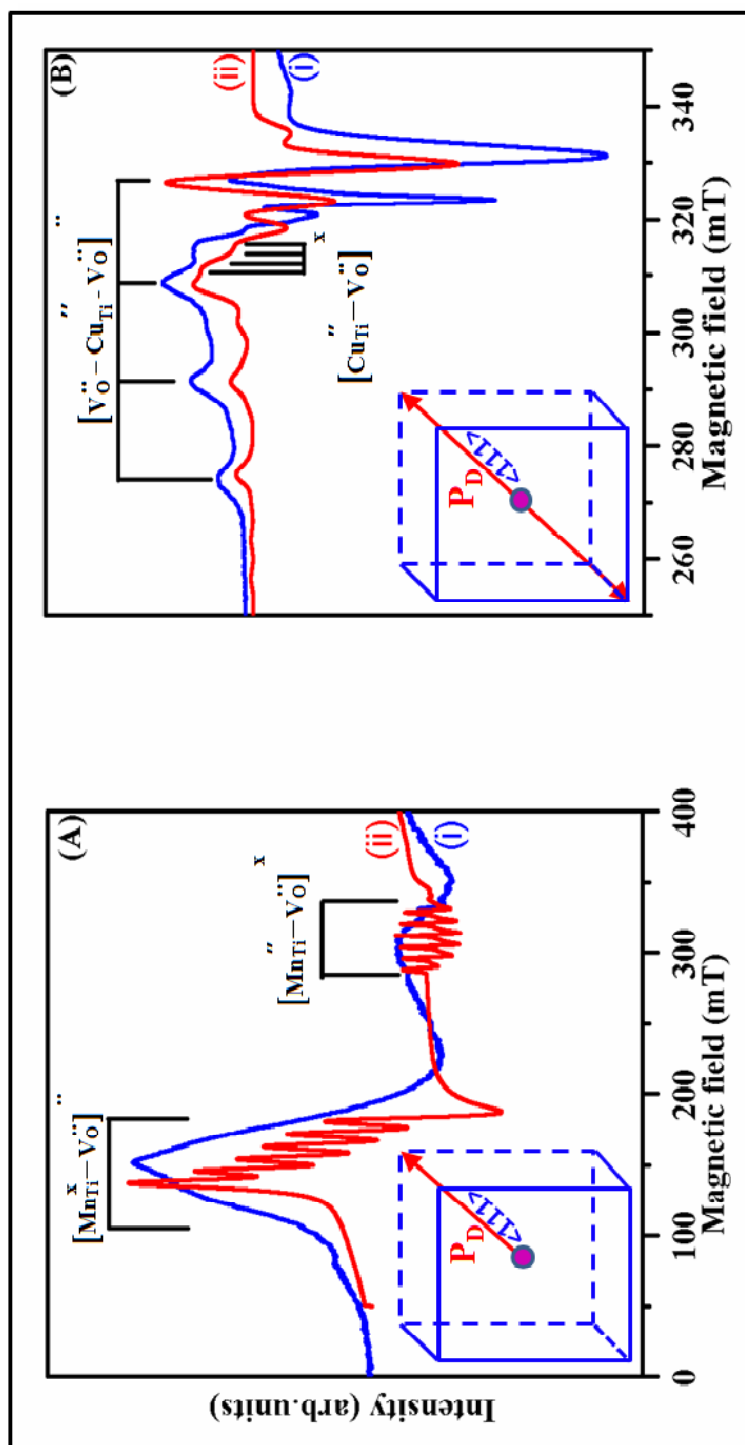


Figure 5.8 Observed (i) and simulated (ii) EPR spectra of (A) Mn-doped PZST, (B) Cu-doped PZST; where \mathbf{P}_D represents the lattice symmetry-attained defect dipole.

Table 5.1 Spin-Hamiltonian parameters

Center	g_{zz}	g_{xy}	A_{zz}	A_{xy}
$\text{Mn}_{\text{Ti}}^{\text{x}} - \ddot{\text{V}}_{\text{O}}$	2.0025	5.2	--	250
$\text{Mn}_{\text{Ti}}^{\text{''}} - \ddot{\text{V}}_{\text{O}}$	2.021	2.1	--	240
$\text{Cu}_{\text{Ti}}^{\text{''}} - \ddot{\text{V}}_{\text{O}}$	2.09	2.45	40	205
$\ddot{\text{V}}_{\text{O}} - \text{Cu}_{\text{Ti}}^{\text{''}} - \ddot{\text{V}}_{\text{O}}$	2.02	2.17	40	500

The existence of $\text{Mn}_{\text{Ti}}^{\text{x}}$ and $\text{Mn}_{\text{Ti}}^{\text{''}}$ is attributed to the facile disproportionation of Mn^{3+} to Mn^{2+} and Mn^{4+} valence states²⁵ which form defect dipoles of the type $[\text{Mn}_{\text{Ti}}^{\text{x}} - \ddot{\text{V}}_{\text{O}}]^{\cdot}$ and $[\text{Mn}_{\text{Ti}}^{\text{''}} - \ddot{\text{V}}_{\text{O}}]^{\text{x}}$. EPR spectrum of Cu-doped PZST is given in Fig. 5.8(B). EPR signals are shown in Fig. 5.8(B)i reveals the presence of two Cu-centres corresponding to a dimeric centre $[\text{Cu}_{\text{Ti}}^{\text{''}} - \ddot{\text{V}}_{\text{O}}]^{\text{x}}$ and a trimeric centre $[\ddot{\text{V}}_{\text{O}} - \text{Cu}_{\text{Ti}}^{\text{''}} - \ddot{\text{V}}_{\text{O}}]^{\cdot}$ ²⁶⁻²⁸ which are confirmed from the simulated EPR spectrum [Fig. 5.8(B) ii]. By analyzing the spectrum it is observed that the trimeric defect structure is prominent in Cu-doped PZST.

As dictated by the symmetry conforming property of the defect dipoles²⁹, these defect dipoles attain the lattice symmetry through short range migration of oxygen vacancies. In both Mn- and Cu-doped PZST, oxygen vacancy migration is facilitated by lattice expansion³⁰ since ionic radii of both Cu^{2+} (0.73Å) and Mn^{3+} (0.65Å) are larger than that of Ti^{4+} (0.61Å). EPR spectrum of Mn-doped PZST reveals the formation of dimeric defect dipoles of type as shown in inset of Fig 5.8(A). As a result, these defect dipoles will be oriented along the direction in which spontaneous polarisation exists. This triggers the alignment of the FE dipoles in the neighboring unit cells along same direction leading to long range FE order. Thus the formation of the incommensurate MCC state is suppressed in Mn-doped PZST. In Cu-doped PZST, such an interaction with the ferroelectric polarisation is not possible

because the trimeric defect centre has a non-polar character [inset of Fig. 5.8(B)] due to its symmetric configuration and results in formation of incommensurate MCC state.

5.4 Conclusion

This study has established the influence of defect structures on the formation of incommensurate structures in a typical incommensurately modulated Sn-modified Lead Zirconate Titanate. Results obtained from temperature dependent dielectric, polarisation-electric field, strain-electric field and EPR spectral investigations have revealed that in tin-modified lead zirconate titanate $\text{Pb}(\text{Zr}_{0.60}\text{Sn}_{0.30}\text{Ti}_{0.10})\text{O}_3$, B-site acceptor dopant, Mn^{3+} suppress the formation of incommensuration whereas in the case of Cu^{2+} -substitution incommensuration is observed as in the case of the parent system. The results suggest that frustration from the competing ferroelectric ordering and antiferroelectric ordering is responsible for the presence of incommensurate structure. By judicious doping and careful examination of defect chemistry, mechanistic aspects of incommensurate structures have been comprehensively established.

References

- [1] V. J. Tennery, "A study of the phase transitions in PbZrO_3 ", *J. Electrochem. Soc.*, 112 (1965) 1117-1120.
- [2] V. J. Tennery, "High-temperature phase transitions in PbZrO_3 ", *J. Am. Ceram. Soc.*, 49 (1966) 483-486.
- [3] G. Shirane and S. Hoshino, "X-ray study of phase transitions in PbZrO_3 containing Ba or Sr", *Acta Cryst.*, 7 (1954) 203-210.
- [4] L. Benguigui, "Ferroelectricity and antiferroelectricity in pure and Nb_2O_5 doped lead zirconate", *J. Solid State chem.*, 3 (1971) 381-386.
- [5] Z. Ujma, "Dielectric properties and phase transitions in PbZrO_3 with oxygen vacancies", *Phase Transitions*, 4 (1984) 169-181.
- [6] B. Jaffe, W. R. Cook and H. Jaffe, "Piezoelectric Ceramics", Academic Press (1971) 129-131.
- [7] W. Pan, Q. Zhang, A. Bhalla and L. E. Cross, "Field-forced antiferroelectric-to-ferroelectric switching in modified lead zirconate titanate stannate ceramics", *J Am. Ceram. Soc.*, 72 (1989) 571-578.
- [8] K. Uchino and S. Nomura, "Electrostriction in PZT-family antiferroelectrics", *Ferroelectrics*, 50 (1983) 191-196.
- [9] D. Berlincourt, H. H. A. Krueger and B. Jaffe, "Stability of phases in modified lead zirconate with variation in pressure, electric field, temperature and composition", *J. Phys. Chem. Solids*, 25 (1964) 659-674.

- [10] D. Viehland, D. Forst and J. F. Li, “Compositional heterogeneity and the origins of the multicell cubic state in Sn-doped lead zirconate titanate ceramics”, *J. Appl. Phys.*, 75 (1994) 4137-4143.
- [11] D. Viehland, D. Forst, Z. Xu and J. F. Li, “Incommensurately modulated polar structures in antiferroelectric Sn-modified lead zirconate titanate: the modulated structure and its influences on electrically induced polarisations and strains”, *J. Am. Ceram. Soc.*, 78 (1995) 2101-2112.
- [12] D. Forst, J. F. Li, Z. Xu and D. Viehland, “Incommensurately modulated polar structures in antiferroelectric tin-modified lead zirconate titanate: ii, dependence of structure-property relations on tin content”, *J. Am. Ceram. Soc.*, 81 (1998) 2225-2236.
- [13] Z. Xu, D. Viehland and D. A. Payne, “An incommensurate-commensurate phase transformation in antiferroelectric tin-modified lead zirconate titanate”, *J. Mater. Res.*, 10 (1995) 453-460.
- [14] Z. Xu, D. Viehland, P. Yang and D. A. Payne, “Hot-stage transmission electron microscopy studies of phase transformations in tin-modified lead zirconate titanate”, *J. Appl. Phys.*, 74 (1993) 3406-3413.
- [15] Y. J. Chang, J. Y. Lian and Y. Wang, “One-dimensional regular arrays of antiphase domain boundaries in anti-ferroelectric tin-substituted lead zirconate titanate (PZT) ceramics”, *Appl. Phys. A: Solids Surf.* 36 (1985) 221-227

- [16] J. S. Speck, M. D. Graef, A. P. Wilkinson, A. K. Cheetham and D. R. Clarke, “Hierarchical domain structures and in situ domain migration in the antiferroelectric ceramic PLSnZT”, *J. Appl. Phys.*, 73 (1993) 7261-7266.
- [17] Y. Imry and S. Ma, “Random-Field instability of the ordered state of continuous symmetry”, *Phys. Rev. Lett.*, 35 (1975) 1399-1401.
- [18] P. Prelovsek and R. Blinc, “Defect and fluctuation effects at the incommensurate commensurate phase transition in Rb_2ZnCl_4 ”, *J. Phys. C*, 17 (1984) 577-588.
- [19] B. Jaffe, W. R. Cook and H. Jaffe, “Piezoelectric Ceramics”, New York, Academic Press (1971).
- [20] E. S. Kirkpatrick, K. A. Muller and R. S. Rubins, “Strong axial electron paramagnetic resonance spectrum of Fe^{3+} in SrTiO_3 due to nearest-neighbour charge compensation”, *Phys. Rev.*, 135 (1964) A86-A90.
- [21] K. A. Muller, W. Berlinger and K. W. Blazey, “Electron paramagnetic resonance of Mn^{4+} in BaTiO_3 ”, *Solid State Commun.*, 61 (1987) 21-25.
- [22] E. Siegel and K. A. Muller, “Structure of transition metal-oxygen vacancy pair centers”, *Phys. Rev. B*, 19 (1979) 109-120.
- [23] S. Stoll and A. Schweiger, “EasySpin, a comprehensive software package for spectral simulation and analysis in EPR”, *J Magn Reson.*, 178 (2006) 42-55.

- [24] K. A. Muller, W. Berlinger, K. W. Blazey and J. Albers, “Electron paramagnetic resonance of Mn^{4+} in $BaTiO_3$ ”, *Solid State Commun.*, 61 (1987) 21-25.
- [25] K. Vani K and V. Kumar, “Influence of defect mobility on electrostrain in acceptor-doped $Ba_{0.80}Sr_{0.20}TiO_3$ ”, *AIP Advances*, 2 (2012) 042177-1-4.
- [26] E. Erunal, P. Jakes, S. Korbelt, J. Acker, H. Kungl, C. Elsasser, M. J. Hoffmann and R. A. Eichel, “CuO-doped $NaNbO_3$ antiferroelectrics: impact of aliovalent doping and nonstoichiometry on the defect structure and formation of secondary phases”, *Phys Rev B*, 84 (2011) 184113-1-11.
- [27] R. A. Eichel, E. Erunal, P. Jakes, S. Korbelt, C. Elsasser, H. Kungl, J. Acker and M. J. Hoffmann, “Interactions of defect complexes and domain walls in CuO-doped ferroelectric $(K,Na)NbO_3$ ”, *Appl. Phys. Lett.*, 102 (2013) 242908-1-5.
- [28] S. M. Ke, H. T. Huang, H. Q. Fan, H. K. Lee, L. M. Zhou and Y. W. Mai “Antiferroelectric-like properties and enhanced polarisation of Cu-doped $K_{0.5}Na_{0.5}NbO_3$ piezoelectric ceramics”, *Appl. Phys. Lett.*, 101 (2012) 082901-1-4.
- [29] X. Ren, “Large electric field-induced strain in ferroelectric crystals by point-defect-mediated reversible domain switching”, *Nat. Mater.*, 3 (2004) 91-94.
- [30] Y. Y. Guo, M. H. Qin, T. Wei and K. F. Wang, “Kinetics controlled aging effect of ferroelectricity in Al-doped and Ga-doped $BaTiO_3$ ”, *Appl. Phys. Lett.*, 97 (2010) 112906-1-3.

Highlights of the Present work

- [1] Ferroelectric aging in hybrid-doped PZT has been studied and shown to be related to the ratio of acceptor: donor dopants.
- [2] Defect chemistry has been correlated with aging-resistance at high levels of donor dopant concentrations in hybrid-doped PZT.
- [3] Local structural rearrangements responsible for FE→R in Lead-based complex perovskites have been established.
- [4] Differences in the sequence of phase transitions on cooling from high temperature paraelectric phase in AFE system have been correlated to the defect chemistry.
- [5] Mechanistic aspects of incommensuration in antiferroelectric PbZrO₃-based compositions have been established.

List of Publications

Journals

- [1] **A. Anil**, K. Vani, V. Kumar, 'Influence of Defect Structure on Ferroelectric Aging in Donor-Acceptor Hybrid doped PZT', *Applied Physics A*, 122:581(2016) 1-5.
- [2] **Adukkadan Anil** and Viswanathan Kumar, 'Local Structural Rearrangements and Evolution of Relaxor State in the Complex Perovskite $(\text{Ba}_{1-x}\text{Pb}_x)(\text{In}_{0.50}\text{Nb}_{0.50})\text{O}_3$ ', *Journal of the American Ceramic Society*, 99(2016) 3980-3984.
- [3] A. S. Divya, P. Juairiya, **A. Anil**, K. Vani, V. Kumar, 'Influence of A-site Sr^{2+} Substitution on Structure, Dielectric and Ferroelectric Characteristics of $0.66[\text{Pb}(\text{In}_{0.50}\text{Nb}_{0.50})\text{O}_3]-0.34[\text{PbTiO}_3]$ ', *Ceramics International*, 43(2017) 825-829.
- [4] **Adukkadan Anil**, Killimangalath Vani, Viswanathan Kumar, 'Role of Defect Structures in Stabilization of Ferroelectric Phase in Tin-Substituted Lead Zirconate Titanate', *Journal of the American Ceramic Society*, 101(2018) 3377-3382.
- [5] Killimangalath Vani, **Adukkadan Anil**, Viswanathan Kumar, 'Enhanced Electrostrain in Cu^{2+} -doped $\text{Ba}_{0.80}\text{Sr}_{0.20}\text{TiO}_3$ ' (Communicated to *Ferroelectrics*)

Paper Presented in Conference/Seminar

A. Anil and Viswanathan Kumar, ‘Mechanistic Aspects of Stabilization of Ferroelectric Phase in Antiferroelectric Tin-modified Lead Zirconate Titanate’, *National Seminar on Frontiers in Chemical Sciences, FCS-2018*, Calicut University, Kerala, February 2018.

Patents

- [1] **Adukkadan Anil**, Vattappilly Priyadarsini, Mani Iyer Sathyanarayanan, Viswanathan Kumar, ‘Piezoelectric compositions, methods and applications thereof’, Indian Patent Application No.1372/DEL/2015, Publication No. 1372/DEL/2015A.
- [2] **Adukkadan Anil**, Vattappilly Priyadarsini, Mani Iyer Sathyanarayanan, Viswanathan Kumar, ‘Piezoelectric compositions, methods and applications thereof’, US Patent Application No.15/152674, Publication No. US2016/0380179 A1.
